UNIVERSITY OF CALIFORNIA

Santa Barbara

The Role of Large-scale Circulation in Recent Arctic Climate Change and Variability: Impacts on Sea Ice, Water Vapor and Aerosols

A Dissertation submitted in partial satisfaction of the

requirements for the degree Doctor of Philosophy

in Geography

by

Ian Takeo Baxter

Committee in charge:

Professor Qinghua Ding, Chair

Professor Leila Carvalho

Professor Charles Jones

June 2024

The dissertation of Ian Takeo Baxter is approved.

_____

Dr. Leila Carvalho

_____

Dr. Charles Jones

_____

Dr. Qinghua Ding, Committee Chair

June 2024

The Role of Large-scale Circulation in Recent Arctic Climate Change and Variability

ACKNOWLEDGEMENTS

I would like to express my deepest gratitude to my mentor, advisor and committee chair, Professor Qinghua Ding, without whom this work would not be possible. I was incredibly fortunate that you advertised the open position in your group in the undergraduate climate modeling class. Your mentorship and guidance have helped me to persevere throughout this journey. I am most grateful to you for providing me this opportunity and preparing me for future endeavors.

I would like to thank my committee members, Professor Leila Carvalho and Professor Charles Jones, for their time and comments to improve this research. Your guidance and kindness have always been very much appreciated.

I would like to express my appreciation to UCSB Department of Geography, the Earth Research Institute, and Department of Earth Science for their support throughout the years. A special thank you to my good friend and officemate Zhe Li for many discussions and meals. Thank you also to the incredible visiting scholars to our group and the collaborators on these studies that have helped me so much with this research and for so many really great discussions.

I would like to thank the Department of Energy's Office of Science Graduate Student Research (SCGSR) Program and High Latitude and Regional Arctic System Modeling (HiLat-RASM) team for allowing me to spend a year at the Pacific Northwest National Laboratory as well as for their support and guidance from which I learned so much and enabled me to conduct much of the work presented here. Lastly, thank you so much to all my family and friends for your unwavering love and support all these years.

VITA OF IAN TAKEO BAXTER

June 2024

Department of Geography/ Earth Research Institute

University of California Santa Barbara, Santa Barbara, CA 93106.

Email: itbaxter@ucsb.edu

Education

PhD, Geography: University of California Santa Barbara (UCSB, Winter 2020- *Spring 2024*)

- Dissertation: Quantifying the role of large-scale circulation in recent extreme changes in Arctic climate and its representation in earth system models
- Committee: Dr. Qinghua Ding (chair), Dr. Charles Jones, Dr. Leila Carvalho

M.A., Geography: University of California Santa Barbara (UCSB, Fall 2017-Fall 2019)

- Thesis: Tropical Pacific sea surface cooling contribution to accelerated Arctic sea ice melt from 2007 to 2012 as ice is thinned by anthropogenic forcing
- Committee: Dr. Qinghua Ding (chair), Dr. Charles Jones, Dr. Leila Carvalho

B.S., Earth Science: University of California Santa Barbara (UCSB, September 2013-June 2017)

- Thesis: Quantifying rates of regional subsidence along eastern Gulf of Mexico since last interglacial
- Adviser: Dr. Alex Simms

Publications

Baxter, I., Wang, H., Ding, Q., Brown, H., Huo, Y., & Yang, Y. (2024). High latitude extreme aerosol transport events (Aerosol Atmospheric Rivers, AARs) during the MOSAiC field expedition captured in the standard resolution and Arctic regionally-refined E3SM. (*in prep*)

Baxter, I., Ding, Q., Wang, H., Ballinger, T., et al. (2024). Sources and land capacitor effects mediating observed summer Arctic moistening and water vapor feedback (*in prep*)

Ballinger, T.J., Moore, G.WK., Ding, Q., … **Baxter, I.**, et al. (2024). Simultaneous Bering Sea and Labrador Sea ice melt extremes in March 2023: A confluence of meteorological events aligned with stratosphere-troposphere interactions. *Weather and Climate Dynamics*. (*submitted*)

Li, Z., Ding, Q., … **Baxter, I.**, (2024) Atmosphere-driven processes in shaping long-term climate variability in Greenland and the broader subpolar North Atlantic. *Journal of Climate*. (*in revision)*

Ma, W., Wang, H., Chen, G., Qian, Y., **Baxter, I**., Huo, Y., & Seefeldt, M. W. (2024). Wintertime Extreme Warming Events in the High Arctic: Characteristics, Drivers, Trends, and the Role of Atmospheric Rivers. *Atmospheric Chemistry and Physics*, 2024, 1-30, https://doi.org/10.5194/egusphere-2023-2018 (*in press*)

Luo, R., Ding, Q., **Baxter, I.**, Chen, X., Wu, Z., Bushuk, M., & Wang, H. (2023). Uncertain role of clouds in shaping summertime atmosphere-sea ice connections in reanalyses and CMIP6 models. *Climate Dynamics*, 1-22, https://doi.org/10.1007/s00382-023-06785-9

Ding, Q., Schweiger, A., & **Baxter, I.** (2022). Nudging observed winds in the Arctic to quantify associated sea ice loss from 1979 to 2020. *Journal of Climate*, 35(20), 3197–3213, https://doi.org/10.1175/JCLI-D- 21-0893.1

Baxter, I., & Ding, Q. (2022). An Optimal Atmospheric Circulation Mode in the Arctic Favoring Strong Summertime Sea Ice Melting and Ice–Albedo Feedback. *Journal of Climate*, 35(20), 3027-3045, https://doi.org/10.1175/JCLI-D-21-0679.1

Huang, Y., Ding, Q., Dong, X., Baike, X., **Baxter, I.** (2021). Summertime low clouds mediate the impact of the large-scale circulation on Arctic sea ice. *Communications Earth and Environment*, https://doi.org/10.1038/s43247-021-00114-w

Luo, R., Ding, Q., Wu, Z., **Baxter, I.**, et al. (2021). Summertime atmosphere–sea ice coupling in the Arctic simulated by CMIP5/6 models: Importance of large-scale circulation. *Climate Dynamics*, 1-19, https://doi.org/10.1175/JCLI-D-20-0216.1

Feng, X., Ding, Q., Wu, L., Jones, C., **Baxter, I.**, et al. (2020). A multidecadal-scale tropically-driven global teleconnection over the past millennium and its recent strengthening. *Journal of Climate*, 1-51, https://doi.org/10.1175/JCLI-D-20-0216.1

Topál, D., Ding, Q., Mitchell, J., **Baxter, I.**, et al. (2020). An internal atmospheric process determining summertime Arctic sea ice melting in the next three decades: lessons learned from five large ensembles and multiple CMIP5 climate simulations. *Journal of Climate*, 33(17), 7431-7454, https://doi.org/10.1175/JCLI-D-19-0803.1

Baxter, I., Ding, Q., Schweiger, A., et al. (2019) How tropical Pacific surface cooling contributed to accelerated sea ice melt from 2007 to 2012 as ice is thinned by anthropogenic forcing, *Journal of Climate*, *32*(24), 8583-8602, https://doi.org/10.1175/JCLI-D-18-0783.1

Ding, Q., ..., **Baxter, I.** (2018) Fingerprints of internal drivers of Arctic sea ice loss in observations and model simulations, *Nature Geoscience*, *12*(1), 28, https://doi.org/10.1038/s41561-018-0256-8.

Presentations

Baxter, I., et al. (2024) Water sources and land capacitor effects facilitating summer Arctic moistening and warming, 2024 UCLA Department of Atmospheric and Oceanic Sciences Informal Seminar (Invited)

Baxter, I., et al. (2024) Increasing importance of North American pathway for Arctic moisture transport and water vapor feedback, 2024 AMS Annual Meeting Polar Symposium

Baxter, I., et al. (2024) Increasing importance of North American pathway for Arctic moisture transport and water vapor feedback, Arctic Modeling and the Early Career Communities: Student Presentations --- Modelers and Early Career Community of Practice Jan 2024 Meeting

Baxter, I., et al. (2024) Increasing importance of North American pathway for Arctic moisture transport and water vapor feedback, US CLIVAR Polar Amplification Meeting (Poster)

Baxter, I., et al. (2023) High latitude extreme aerosol transport events (Aerosol Atmospheric Rivers, AARs) during the MOSAiC field expedition captured in the E3SM, 2023 AGU Fall Meeting

Baxter, I., et al. (2023) Preconditioning of Arctic summer sea ice via increasing poleward moisture transport and rainfall sourced from North America, 2023 AGU Fall Meeting

Baxter, I., et al. (2023) High latitude extreme aerosol transport events (Aerosol Atmospheric Rivers, AARs) during the MOSAiC field expedition captured in the E3SM, DOE Career Conversations

Baxter, I., et al. (2023) High latitude extreme aerosol transport events (Aerosol Atmospheric Rivers, AARs) during the MOSAiC field expedition captured in the E3SM, AeroCom/AeroSAT Conference

Baxter, I., et al. (2023) Arctic precipitation in circulation-constrained CESM1/2 simulations and the role of meridional moisture transport, 2023 CESM Workshop

Baxter, I., et al. (2023) High latitude extreme aerosol transport events (Aerosol Atmospheric Rivers, AARs) during the MOSAiC field expedition captured in the E3SM, 2023 UCSB Climate Meeting Seminar Series

Baxter, I., Ding, Q. (2022) An Optimal Large-Scale Wind Pattern Favoring Summertime Arctic Sea Ice Loss in Wind Nudging Simulations, Polar AMS/Collective Madison Meeting (Invited)

Baxter, I. (2021) Optimal large-scale wind patterns favoring strong sea ice melting and ice-albedo feedback in the absence of anthropogenic forcing, AGU Annual Meeting 2021 (Poster)

Baxter, I., Ding, Q. (2021) Optimal large-scale wind patterns favoring strong sea ice melting and ice-albedo feedback in the absence of anthropogenic forcing, Polar Climate Modeling Working Group Meeting

Baxter, I., Ding, Q. (2021) Optimal large-scale wind patterns favoring strong sea ice melting and ice-albedo feedback in the absence of anthropogenic forcing, 16th Conference on Polar Meteorology and Oceanography Virtual Meeting

Baxter, I., Ding, Q. (2021) Optimal large-scale wind patterns favoring strong sea ice melting and ice-albedo feedback in the absence of anthropogenic forcing, AMS Annual Meeting 2021

Baxter, I., Ding, Q. (2020) Optimal large-scale wind patterns favoring strong sea ice melting and ice-albedo feedback in the absence of anthropogenic forcing, AGU Annual Meeting 2020 (Poster)

Baxter, I., et al. (2020) How tropical Pacific sea surface cooling enhanced Arctic sea ice melt from 2007 to 2012, Polar Climate Modeling Working Group Meeting

Baxter, I., et al. (2020) How tropical Pacific sea surface cooling enhanced Arctic sea ice melt from 2007 to 2012, NCAR Informal Seminar (Invited)

Baxter, I. (2019) Interdecadal variability of summer Arctic sea ice associated with tropical SST changes, 15th Conference on Polar Meteorology and Oceanography Meeting

Baxter, I. (2018) Recent slow melt of summer Arctic sea ice caused by tropical Pacific SST changes, NOAA 43rd Climate Diagnostics and Prediction Workshop, University of California Santa Barbara

Baxter, I. (2018) Recent slow melt of summer Arctic sea ice caused by tropical Pacific SST changes, NOAA 43rd Climate Diagnostics and Prediction Workshop, University of California Santa Barbara (Poster)

Awards

UCSB Geography Regents Fellowship, Santa Barbara, CA (2017-2018)

Co-Outstanding Student Oral Presentation, AMS Collective Meeting, Madison, WI (2022)

DOE Science Graduate Student Research Award (SCGSR): BER Atmospheric System Research (2023)

- Project: Role of large-scale circulation in shaping Arctic cloud-aerosol interactions in E3SM
- Host Scientist: Dr. Hailong Wang, Pacific Northwest National Laboratory (PNNL), Richland, WA

ABSTRACT

The Role of Large-scale Circulation in Recent Arctic Climate Change and Variability: Impacts on Sea Ice, Water Vapor and Aerosols

by

Ian Takeo Baxter

Over the last few decades, the Arctic has warmed at a rate 3-4 times the global average, referred to as Arctic Amplification. The rate of amplified warming has been attributed to complex interactions amongst feedback processes, making it difficult to understand and isolate the leading causes. Due to this uncertainty, there is a large divide between model simulated changes in the Arctic and those in observations, undermining confidence in our ability to project future polar warming and its impacts. Thus, this research seeks to bridge the gap between climate models and observations by imposing essential observed conditions (e.g., circulation changes, aerosol emissions, etc.) in climate models to understand and quantify their roles in shaping various aspects of climate variability in the Arctic, including the warming rates of some key fields determining cryosphere conditions, extreme weather, energy budget, and climate states. Multiple versions of two climate models (CESM and E3SM) are used in my research, enabling me to investigate these topics with less impacts due to the sensitivity of a specific model to imposed forcing. According to this overarching goal, my overall effort is equally allocated to address the following issues, which are detailed in the subsequent chapters: Chapter 1 details the key motivations driving the research questions explored in the following

chapters. The representation of internal variability in climate models, manifested as large-scale circulation, is a leading factor causing biases relative to observations. Chapter 2 addresses this effect of circulation on summer sea ice, employing an atmospheric wind nudging approach. This chapter characterizes the optimal large-scale wind pattern contributing to enhanced sea ice decline: a quasi-barotropic anticyclonic pattern with high pressure over the Arctic and Greenland that adiabatically warms the lower troposphere and increases downwelling longwave radiation. This pattern is found to coincide with periods of enhanced sea ice decline in preindustrial simulations and paleoclimate products, suggesting it is likely of internal origin. In Chapter 3, I examine the role of large-scale circulation in driving moisture transport into the Arctic and their radiative impacts during Northern Hemisphere summer. Using a combined nudging and moisture tagging approach in the iCESM1, it is found that the large-scale circulation drives an increase in atmospheric rivers which dominate high latitude moistening and the water vapor feedback. Two thirds of the of poleward transport passes through the high latitude land masses via a land capacitor effect, first originating from the tropical Atlantic and Mediterranean Sea. Chapter 4 investigates the response of extreme black carbon transport to large-scale circulation during the MOSAiC field campaign. Using statistical techniques and wind nudging in the E3SMv2 it is found that an Arctic Oscillation pattern is the leading determinant of poleward black carbon transport. Simulations with constrained circulation show improvements in mean poleward black carbon transport and occurrence of extreme events, but still underestimate the magnitude of transport. Altogether, this research addresses knowledge gaps pertaining to the uncertainties in the leading drivers of warming and sea ice loss between models and observations, identifying that many of the discrepancies are likely associated with the representation of large-scale circulation changes.

TABLE OF CONTENTS

Chapter 1

Introduction

I.T. Baxter

1.1 Overview

1.1.1 Amplified Arctic Warming

The Arctic has warmed at 4 times the rate of global mean surface temperature – commonly referred to as Polar or Arctic Amplification – coinciding with a rapid retreat of sea and land ice (Manabe and Wetherald 1975; Serreze and Francis 2006; Comiso et al. 2008; Mouginot et al. 2019). Arctic Amplification was first demonstrated in 1970s in a series of studies using the first global climate models (Manabe and Wetherald 1975; Manabe and Stouffer 1979). In the four and a half decades since, the pattern of Arctic Amplification, with enhanced warming in the winter and muted warming in the summer, has come to fruition (Fig. 1.1). From the beginning, it was understood that this amplified warming can primarily been attributed to a decrease of sea ice volume resulting from the radiative effects of increasing atmospheric greenhouse gas concentrations (Manabe and Stouffer 1979; Holland and Bitz 2003; Taylor et al. 2013; Notz and Stroeve 2016). However, the Coupled Model Intercomparison Project Phase 5 and 6 (Taylor et al. 2012; Eyring et al. 2016) models generally underestimate the rate of Arctic Amplification (Previdi et al. 2021; Hahn et al. 2021). This suggests that there are likely other processes contributing to warming that are not well understood, including poleward heat, moisture and aerosol transport (Pithan and Mauritsen 2014; Goose et al. 2018).

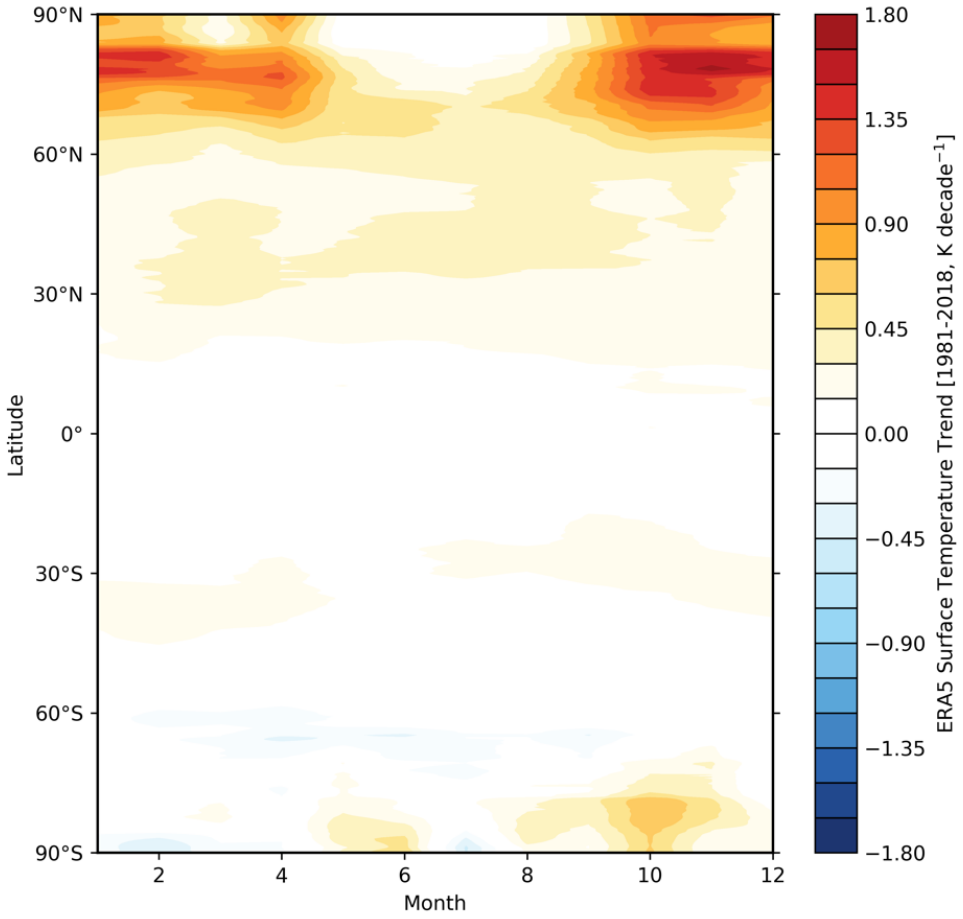

Figure 1.1 Arctic Amplification Zonal mean monthly ERA5 surface temperature trends (1981-2018, K decade-1). This figure is inspired by the first published evidence of Arctic Amplification in model simulations conducted by Manabe & Stouffer (1980).

While Arctic Amplification is most prominently known by its peak warming during boreal winter, this rate of warming is foremost determined by processes contributing to heat uptake by the ocean in summer (Pithan and Mauritsen 2014; Hahn et al. 2021; Chung and Feldl 2023). This can occur through a multitude of pathways, including downwelling long- and shortwave radiation (Ding et al. 2017), warmer atmospheric temperatures (Olonscheck et al. 2019; Bonan et al. 2021), mechanical breakup of ice (Marko 2003; Asplin et al. 2012; Kohout et al. 2014), export through the Fram Strait (Smedsrud et al. 2017; Spreen et al. 2020) and ocean heat transport and mixing (Polyakov et al. 2020). Therefore, greater understanding of the

mechanisms determining the retreat of sea ice cover, decrease in snow insulating the sea ice, and radiative processes that further warm the upper Arctic Ocean are key to projecting future climate change in the region across seasons.

Within the Arctic, this warming is expected to lead to large changes in other aspects beyond just declining sea ice, as the Arctic potentially enters a new climate regime (Landrum and Holland 2020). One of the primary targets for defining this "New Arctic", is the first occurrence of an ice-free summer (Wang and Overland 2009; Screen and Williamson 2017; Notz and Stroeve 2018; Sigmond et al. 2018; Jahn et al. 2024). Projections from climate models place this first occurrence somewhere between 2030 and 2050 (Topál and Ding 2023; Kim et al. 2023; Jahn et al. 2024). However, the free-running large ensemble simulations suggest that the first occurrence of ice-free conditions should have already taken place (Fig. 1.2). If we compare September sea ice area from observations with that from these large ensembles, we find that they underestimate sea ice cover (Fig. 1.2a). Some of these biases in the amount of sea ice seen in large ensembles have been linked to clouds physics and aerosol forcing (DuVivier et al. 2020; DeRepentigny et al. 2022).

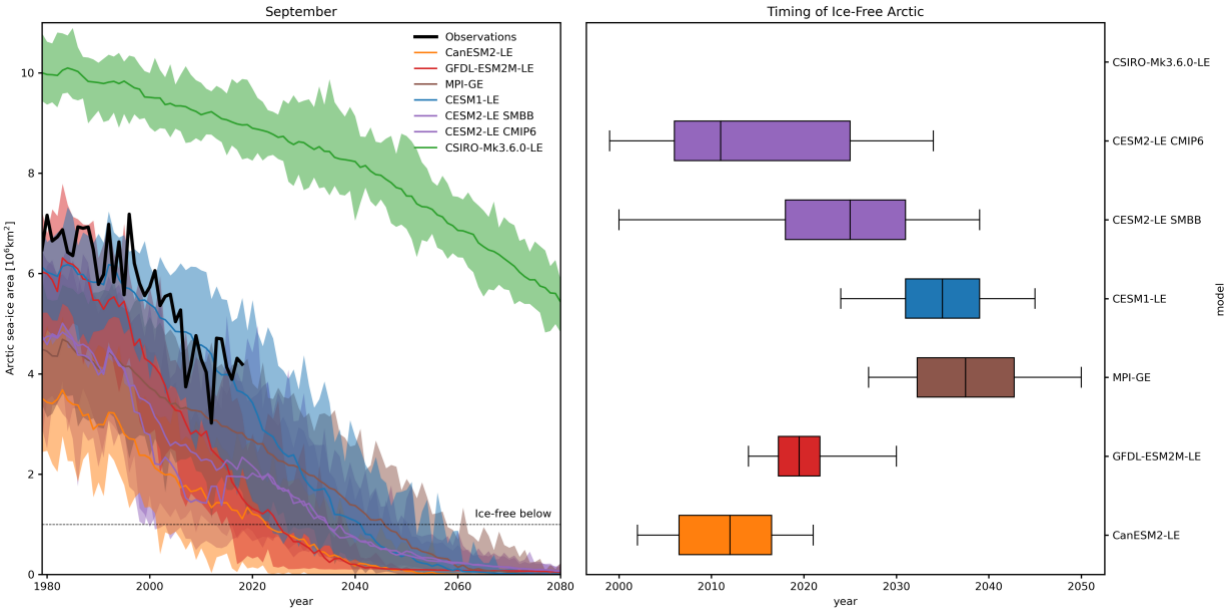

Figure 1.2 Ice-free conditions (a) Total Arctic September sea ice area from 5 SMILEs. The solid lines show the ensemble means of each SMILE and the shading shows the total spread amongst the members of each SMILE. (b) The first occurrence of ice-free (SIA < 1 million km^{-2}) from each SMILE.

A shift to ice-free conditions has complex implications for the ecosystems, as many of these communities rely on the ice yet flourish under thin, first year ice when they can receive sunlight (Clement Kinney et al. 2023). Biological processes associated with these ecosystems can also further contribute to warming and sea ice loss in the Arctic through release of biogenic aerosols (Kramshøj et al. 2016; Nielsen et al. 2019). The loss of sea ice could also alter the stability of the lower troposphere which can then modulate the release of heat and moisture out of the surface through processes such as the lapse rate feedback (Morrison et al. 2019; Boeke et al. 2021; Feldl et al. 2020). However, during summertime it should be noted that much of the heat is directed towards melting of sea ice and ocean mixed layer uptake, leading to relatively small gradients between the ocean and atmosphere (Kay et al. 2016; Morrison et al. 2019; Hahn et al. 2022). This leaves the Arctic particularly susceptible to changes in the overlying atmosphere and poleward transport, which we will explore in this dissertation (Feldl et al. 2020).

The implications of preferential warming in the Arctic are not limited to the region but may alter meridional temperature and energy gradients that can lead to changes in midlatitude storm tracks and the jet stream (Francis and Vavrus 2012; Cohen et al. 2014). The most prominent example of this connection is often associated with the winter phenomenon referred to as the Warm Arctic Cold Eurasia (Mori et al. 2014) pattern. An example of a summertime connection is that Arctic sea ice loss has been suggested to weaken the summertime storm tracks (Coumou et al. 2015; Gertler and O'Gorman 2019; Kang et al. 2023). Many studies in recent years and

several coordinated efforts have strived to characterize the potential influence that Arctic Amplification can have on midlatitude weather and potentially the tropics (Smith et al. 2019). However, many of these teleconnections between the Arctic and midlatitudes own weak signals relative to the climate noise, requiring either long integrations or a large number of ensemble members (Blackport et al. 2019; Cohen et al. 2020).

1.1.2 Uncertainty in Arctic Climate Change from Observations vs. Models

In addition to Arctic Amplification, another common metric of polar climate change that focuses on sea ice is referred to as sea ice sensitivity. This is defined as the change in total sea ice extent divided by change in global mean surface temperature (Rosenblum and Eisenman 2017; DeRepetigney et al. 2022). Models across the board show much weaker sea ice sensitivity relative to observations, with observed sensitivity far outside the spread of Coupled Model Intercomparison Project Phase 5 and 6 (CMIP5/6) models. Many studies have since implicated weak sea ice sensitivity as a key motivation for focusing more on improving the representation of local processes, but this definition overlooks spatial variations in surface temperature warming.

Over the recent decade more studies have noted the potentially important role of internal climate variability in determining the rate of amplified warming and difference between observed and simulated sea ice sensitivity (Winton 2011; Swart et al. 2015; Rosenblum and Eisenman 2017; Wu et al. 2021). Subsequent research has estimated this contribution from internal variability at around 30-50% (Ding et al. 2017; England et al. 2019). Trends in 200 hPa geopotential height over the historical period highlight this discrepancy (Fig. 1.3). Reanalysis show strong increasing geopotential height and warming over the Arctic during

summertime, with weak warming in the tropics and subtropics (Fig. 1.3a). However, in the multi-model and ensemble means from CMIP6, the Community Earth System Model Large Ensemble version 2 (Danabasoglu et al. 2020), and CESM1-LE (Kay et al. 2015), we see a relatively uniform warming signature globally (Fig. 1.3b-d). If we consider the differences between model and observed sea ice sensitivity, again defined as the trend in total sea ice area per degree global warming, we must consider the warming due to the pattern of large scale circulation and its interactions with sea surface temperatures (Dong et al. 2019, 2020; Andrews et al. 2022; Wills et al. 2022).

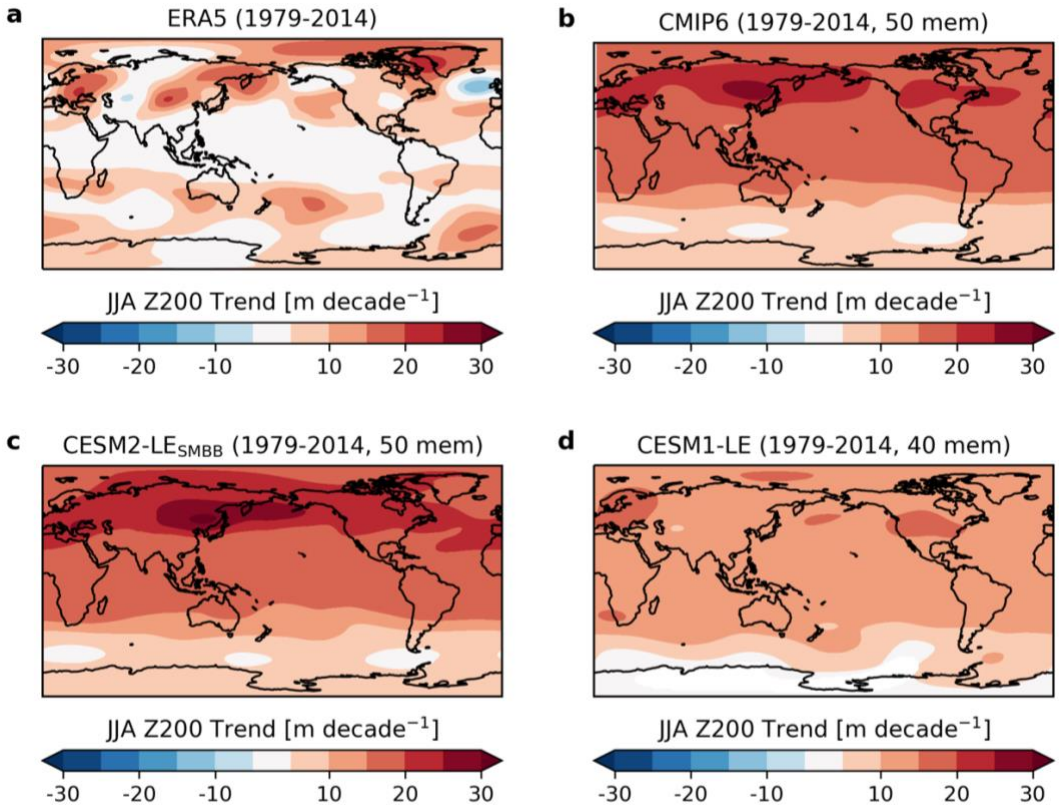

Figure 1.3. Drivers of historical warming: Linear trends (1979-2014) in 200 hPa geopotential heights from (a) ERA5, and the ensemble means from (b) CMIP6, (c) the CESM2-LE, and (d) the CESM1-LE.

Previously for my Master's Thesis, I examined a teleconnection between summertime tropical Pacific sea surface temperatures and Arctic sea ice, which we named the Pacific-Arctic teleconnection (PARC, Baxter et al. 2019). A sea surface temperature cooling in the central and eastern Pacific reminiscent of La Nina, negative Pacific Meridional Mode (PMM; , negative Interdecadal Pacific Oscillation (IPO) or negative Pacific Decadal Oscillation (Mantua et al. 1997; Newman et al. 2016) generated an anomalous Rossby wave train from the tropics to high latitudes. In this study, we were unable to definitively link the teleconnection to sea ice loss due to a lack of a dynamical sea ice and ocean model, in addition to potential model limitations in capturing the propagation of this wave train (Bonan and Blanchard-Wrigglesworth 2020; Topál et al. 2020; Feng et al. 2021; Sweeney et al. 2023; Wyburn-Powell and Jahn 2023). Therefore, the following chapters in this dissertation are motivated by a nudging approach developed to more realistically quantify the role of large-scale circulation, considering both the direct impacts of circulation on temperature as well as indirect effects through transport of water vapor and aerosols.

1.2 Dissertation Objectives

The rate of Arctic Amplification has broad consequences for ecosystems, resources, and societies both locally within the region but also in lower latitudes. Linking together the polar regions with the rest of the world, through its connections with large-scale circulation and the hydrological and carbon cycles, is of the utmost importance for creating a sustainable future. However, before we can make reliable projections of future responses to Arctic Amplification, we must first understand the key processes that cause it. We have known for decades that a decline in sea ice and snow cover leads to an enhancement of high latitude warming, yet it is

still uncertain what drives that sea ice decline, how it interacts with other feedback processes, and how that rate of warming will evolve in the future. Previous work by myself and others has shown that large-scale circulation, especially in boreal summer, serves as a bridge, linking many of the processes that contribute to Arctic Amplification together. **Thus, the overarching goal of this research is to determine the impact of observed large-scale circulation in recent Arctic climate change by examining its direct influence on temperature and radiation as well as its indirect control through modulating sea ice, moisture, and aerosols.** In this dissertation, we reconcile observations and models by employing a data assimilation technique, referred to as nudging, in a series of Earth System Models. This approach enables the examination of the impacts of large-scale circulation as a leading control determining the rate of change taking place in the Arctic. This dissertation is divided into three main chapters, with each chapter investigating the interactions of large-scale circulation with local radiative processes, remote transport and external forcing.

In Chapter 2, I examine the impacts of boreal summer large-scale circulation on September sea ice loss. Using a set of perpetual (same year repeated for 10+ model years) nudging simulations in the CESM1, I quantify the contribution from individual atmospheric circulation patterns that favor strong sea ice decline. This approach identifies a "Figure-8" quasi-barotropic anticyclonic pattern with a lobe centered over the sea ice and another over Greenland. The model simulations suggest that this optimal circulation pattern that can enhance sea ice by adiabatically warming the lower troposphere, that then generates moistening and low cloud increases near the surface, leading to the enhanced emission of downwelling longwave radiation that melts the top of the sea ice and snow in early summer, then the upper ocean in late summer. To reconcile with free running model simulations and

other observation-based datasets, I seek the optimal wind pattern leading to strong sea ice loss in the CESM1 piControl simulation and several paleoreanalysis products. In all datasets, high pressure over the Arctic coincides with periods of the strongest warming and melting. The free-running model, however, struggles to capture the second lobe of the "Figure-8" over Greenland.

Chapter 3 quantifies the contribution of moisture transport to summertime water vapor radiative effects within the Arctic. The goal of this chapter was to identify the major source regions that feed moisture into the Arctic, then quantify their impact on the Arctic energy budget using a radiative feedback analysis. To do this, water vapor is tracked from evapotranspiration at the surface until it is precipitated out back again at the surface. This approach reveals the importance of the high latitude land surface as an intermediary leaking moisture transport from the tropics into the Arctic, which we refer to as the land capacitor effect. The land capacitor effect describes deposition of moisture originating from the tropics in late winter and spring over northeastern North America and western/central Eurasia that is then evaporated in summer and transported in atmospheric rivers into the Arctic. We calculate that this transport mechanism accounts for 2/3 of the moistening trends seen over the historical period. Using two radiative feedback kernel frameworks, it also found that this moistening has had a dominant influence on the water vapor feedback, accounting for 83% of the positive warming feedback at the surface over the last four decades. This chapter highlights the importance of large-scale circulation in determining the pathway and magnitude of poleward transport and its influence on amplified polar warming.

Lastly, I investigate the role of large-scale circulation is contributing to the underestimation of aerosols in the Arctic simulated by global climate models in Chapter 4. Using Maximum

Covariance Analysis, I identify the dominant circulation pattern contributing to changes in high latitude black carbon to be an Arctic Oscillation-like configuration with high pressure over the central Arctic and low pressure over Europe and Siberia controlling poleward aerosol fluxes. This configuration was very strongly in its positive phase (low pressure over Arctic, high pressure in midlatitudes) during the 2019-2020 MOSAiC field expedition, suggesting that our best in situ measurements in the deep Arctic likely sampled a weak transport year. Despite this, extremely large black carbon events were measured, and it is shown that MERRA-2 is able to capture these rapid increases and their associated transport during the colder months, but not as well in summer. Constraining atmospheric circulation through wind nudging in E3SMv2 results in an improvement in the annual mean poleward transport. However, higher resolution, achieved through regional refinement over high latitudes, produces much improved aerosol atmospheric river occurrence as detected by a modified moisture atmospheric river detection and tracking algorithm, though both E3SMv2 simulations still underestimate the amount transport in extreme events. These results highlight the importance of large-scale circulation in capturing the redistribution of aerosols to remote regions, which can huge impacts in our quantification of radiative feedbacks and climate sensitivity.

This dissertation characterizes direct and indirect mechanisms by which large-scale circulation, which can be representative of internal climate variability, contributes to Arctic climate change seen over recent decades. This work also serves to bridge the gaps between global climate model simulations and observations, by leveraging an online data assimilation technique, referred to as nudging, to ground our understanding in the historical record. We show that large-scale circulation changes, largely driven by changes in tropical sea surface temperatures, are responsible for much of the change we see in the Arctic (Baxter et al. 2019;

Baxter and Ding 2022). Specifically, these changes have generated anticyclonic circulation over the boreal summer Arctic, leading to warming through subsidence, as well as import of moisture and aerosols. The understanding gained through this dissertation has important implications that can be used to constrain future Arctic warming and sea ice loss.

1.3 Permissions and Attributions

1. The content of chapter 2 and appendix A is the result of a collaboration with Dr. Qinghua Ding and has previously appeared in Journal of Climate (Baxter & Ding, 2022). It is reproduced here with the permission of the © **American Meteorological Society. Used with permission:** https://journals.ametsoc.org/view/journals/clim/35/20/JCLI-D-21-0679.1.xml

References

Andrews, T., and Coauthors, 2022: On the Effect of Historical SST Patterns on Radiative Feedback. *Journal of Geophysical Research: Atmospheres*, **127**, e2022JD036675, https://doi.org/10.1029/2022JD036675.

Asplin, M. G., R. Galley, D. G. Barber, and S. Prinsenberg, 2012: Fracture of summer perennial sea ice by ocean swell as a result of Arctic storms. *Journal of Geophysical Research: Oceans*, **117**, https://doi.org/10.1029/2011JC007221.

Baxter, I., and Q. Ding, 2022: An Optimal Atmospheric Circulation Mode in the Arctic Favoring Strong Summertime Sea Ice Melting and Ice–Albedo Feedback. *Journal of Climate*, **35**, 6627–6645, https://doi.org/10.1175/JCLI-D-21-0679.1.

——, and Coauthors, 2019: How Tropical Pacific Surface Cooling Contributed to Accelerated Sea Ice Melt from 2007 to 2012 as Ice Is Thinned by Anthropogenic Forcing. *Journal of Climate*, **32**, 8583–8602, https://doi.org/10.1175/JCLI-D-18-0783.1.

Blackport, R., J. A. Screen, K. van der Wiel, and R. Bintanja, 2019: Minimal influence of reduced Arctic sea ice on coincident cold winters in mid-latitudes. *Nat. Clim. Chang.*, **9**, 697–704, https://doi.org/10.1038/s41558-019-0551-4.

Boeke, R. C., P. C. Taylor, and S. A. Sejas, 2021: On the Nature of the Arctic's Positive Lapse-Rate Feedback. *Geophysical Research Letters*, **48**, e2020GL091109, https://doi.org/10.1029/2020GL091109.

Bonan, D. B., and E. Blanchard-Wrigglesworth, 2020: Nonstationary Teleconnection Between the Pacific Ocean and Arctic Sea Ice. *Geophysical Research Letters*, **47**, e2019GL085666, https://doi.org/10.1029/2019GL085666.

Bonan, D. B., T. Schneider, I. Eisenman, and R. C. J. Wills, 2021: Constraining the Date of a Seasonally Ice-Free Arctic Using a Simple Model. *Geophysical Research Letters*, **48**, e2021GL094309, https://doi.org/10.1029/2021GL094309.

Chung, P.-C., and N. Feldl, 2023: Sea Ice Loss, Water Vapor Increases, and Their Interactions with Atmospheric Energy Transport in Driving Seasonal Polar Amplification. *Journal of Climate*, **1**, 1–28, https://doi.org/10.1175/JCLI-D-23-0219.1.

Clement Kinney, J., M. Frants, W. Maslowski, R. Osinski, N. Jeffery, M. Jin, and Y. J. Lee, 2023: Investigation of Under-Ice Phytoplankton Growth in the Fully-Coupled, High-Resolution Regional Arctic System Model. *Journal of Geophysical Research: Oceans*, **128**, e2022JC019000, https://doi.org/10.1029/2022JC019000.

Cohen, J., and Coauthors, 2014: Recent Arctic amplification and extreme mid-latitude weather. *Nature Geosci*, **7**, 627–637, https://doi.org/10.1038/ngeo2234.

Cohen, J., and Coauthors, 2020: Divergent consensuses on Arctic amplification influence on midlatitude severe winter weather. *Nat. Clim. Chang.*, **10**, 20–29, https://doi.org/10.1038/s41558-019-0662-y.

Comiso, J. C., C. L. Parkinson, R. Gersten, and L. Stock, 2008: Accelerated decline in the Arctic sea ice cover. *Geophysical Research Letters*, **35**, https://doi.org/10.1029/2007GL031972.

Coumou, D., J. Lehmann, and J. Beckmann, 2015: The weakening summer circulation in the Northern Hemisphere mid-latitudes. *Science*, **348**, 324–327, https://doi.org/10.1126/science.1261768.

Danabasoglu, G., and Coauthors, 2020: The Community Earth System Model Version 2 (CESM2). *Journal of Advances in Modeling Earth Systems*, **12**, e2019MS001916, https://doi.org/10.1029/2019MS001916.

DeRepentigny, P., and Coauthors, 2022: Enhanced simulated early 21st century Arctic sea ice loss due to CMIP6 biomass burning emissions. *Science Advances*, **8**, eabo2405, https://doi.org/10.1126/sciadv.abo2405.

Ding, Q., and Coauthors, 2017: Influence of high-latitude atmospheric circulation changes on summertime Arctic sea ice. *Nature Clim Change*, **7**, 289–295, https://doi.org/10.1038/nclimate3241.

Dong, Y., C. Proistosescu, K. C. Armour, and D. S. Battisti, 2019: Attributing Historical and Future Evolution of Radiative Feedbacks to Regional Warming Patterns using a Green's Function Approach: The Preeminence of the Western Pacific. *Journal of Climate*, **32**, 5471–5491, https://doi.org/10.1175/JCLI-D-18-0843.1.

——, K. C. Armour, M. D. Zelinka, C. Proistosescu, D. S. Battisti, C. Zhou, and T. Andrews, 2020: Intermodel Spread in the Pattern Effect and Its Contribution to Climate Sensitivity in CMIP5 and CMIP6 Models. *Journal of Climate*, **33**, 7755–7775, https://doi.org/10.1175/JCLI-D-19-1011.1.

DuVivier, A. K., M. M. Holland, J. E. Kay, S. Tilmes, A. Gettelman, and D. A. Bailey, 2020: Arctic and Antarctic Sea Ice Mean State in the Community Earth System Model Version 2 and the Influence of Atmospheric Chemistry. *Journal of Geophysical Research: Oceans*, **125**, e2019JC015934, https://doi.org/10.1029/2019JC015934.

England, M., A. Jahn, and L. Polvani, 2019: Nonuniform Contribution of Internal Variability to Recent Arctic Sea Ice Loss. *Journal of Climate*, **32**, 4039–4053, https://doi.org/10.1175/JCLI-D-18-0864.1.

Eyring, V., S. Bony, G. A. Meehl, C. A. Senior, B. Stevens, R. J. Stouffer, and K. E. Taylor, 2016: Overview of the Coupled Model Intercomparison Project Phase 6 (CMIP6) experimental design and organization. *Geoscientific Model Development*, **9**, 1937–1958, https://doi.org/10.5194/gmd-9-1937-2016.

Feldl, N., S. Po-Chedley, H. K. A. Singh, S. Hay, and P. J. Kushner, 2020: Sea ice and atmospheric circulation shape the high-latitude lapse rate feedback. *npj Clim Atmos Sci*, **3**, 1–9, https://doi.org/10.1038/s41612-020-00146-7.

Feng, X., and Coauthors, 2021: A Multidecadal-Scale Tropically Driven Global Teleconnection over the Past Millennium and Its Recent Strengthening. *Journal of Climate*, **34**, 2549–2565, https://doi.org/10.1175/JCLI-D-20-0216.1.

Francis, J. A., and S. J. Vavrus, 2012: Evidence linking Arctic amplification to extreme weather in mid-latitudes. *Geophysical Research Letters*, **39**, https://doi.org/10.1029/2012GL051000.

Gertler, C. G., and P. A. O'Gorman, 2019: Changing available energy for extratropical cyclones and associated convection in Northern Hemisphere summer. *Proceedings of the National Academy of Sciences*, **116**, 4105–4110, https://doi.org/10.1073/pnas.1812312116.

Hahn, L. C., K. C. Armour, M. D. Zelinka, C. M. Bitz, and A. Donohoe, 2021: Contributions to Polar Amplification in CMIP5 and CMIP6 Models. *Frontiers in Earth Science*, **9**.

Hahn, L. C., K. C. Armour, D. S. Battisti, I. Eisenman, and C. M. Bitz, 2022: Seasonality in Arctic Warming Driven by Sea Ice Effective Heat Capacity. *Journal of Climate*, **35**, 1629–1642, https://doi.org/10.1175/JCLI-D-21-0626.1.

Holland, M. M., and C. M. Bitz, 2003: Polar amplification of climate change in coupled models. *Climate Dynamics*, **21**, 221–232, https://doi.org/10.1007/s00382-003-0332-6.

Jahn, A., M. M. Holland, and J. E. Kay, 2024: Projections of an ice-free Arctic Ocean. *Nat Rev Earth Environ*, **5**, 164–176, https://doi.org/10.1038/s43017-023-00515-9.

Kang, J. M., T. A. Shaw, and L. Sun, 2023: Arctic Sea Ice Loss Weakens Northern Hemisphere Summertime Storminess but Not Until the Late 21st Century. *Geophysical Research Letters*, **50**, e2022GL102301, https://doi.org/10.1029/2022GL102301.

Kay, J. E., and Coauthors, 2015: The Community Earth System Model (CESM) Large Ensemble Project: A Community Resource for Studying Climate Change in the Presence of Internal Climate Variability. *Bulletin of the American Meteorological Society*, **96**, 1333–1349, https://doi.org/10.1175/BAMS-D-13-00255.1.

Kay, J. E., T. L'Ecuyer, H. Chepfer, N. Loeb, A. Morrison, and G. Cesana, 2016: Recent Advances in Arctic Cloud and Climate Research. *Curr Clim Change Rep*, **2**, 159–169, https://doi.org/10.1007/s40641-016-0051-9.

Kim, Y.-H., S.-K. Min, N. P. Gillett, D. Notz, and E. Malinina, 2023: Observationally-constrained projections of an ice-free Arctic even under a low emission scenario. *Nat Commun*, **14**, 3139, https://doi.org/10.1038/s41467-023-38511-8.

Kramshøj, M., I. Vedel-Petersen, M. Schollert, Å. Rinnan, J. Nymand, H. Ro-Poulsen, and R. Rinnan, 2016: Large increases in Arctic biogenic volatile emissions are a direct effect of warming. *Nature Geosci*, **9**, 349–352, https://doi.org/10.1038/ngeo2692.

Landrum, L., and M. M. Holland, 2020: Extremes become routine in an emerging new Arctic. *Nat. Clim. Chang.*, **10**, 1108–1115, https://doi.org/10.1038/s41558-020-0892-z.

Manabe, S., and R. T. Wetherald, 1975: The Effects of Doubling the CO2 Concentration on the climate of a General Circulation Model. *Journal of the Atmospheric Sciences*, **32**, 3–15, https://doi.org/10.1175/1520-0469(1975)032<0003:TEODTC>2.0.CO;2.

——, and R. J. Stouffer, 1979: A CO2-climate sensitivity study with a mathematical model of the global climate. *Nature*, **282**, 491–493, https://doi.org/10.1038/282491a0.

Mantua, N. J., S. R. Hare, Y. Zhang, J. M. Wallace, and R. C. Francis, 1997: A Pacific Interdecadal Climate Oscillation with Impacts on Salmon Production*. *Bulletin of the American Meteorological Society*, **78**, 1069–1080, https://doi.org/10.1175/1520-0477(1997)078<1069:APICOW>2.0.CO;2.

Marko, J. R., 2003: Observations and analyses of an intense waves-in-ice event in the Sea of Okhotsk. *Journal of Geophysical Research: Oceans*, **108**, https://doi.org/10.1029/2001JC001214.

Mori, M., M. Watanabe, H. Shiogama, J. Inoue, and M. Kimoto, 2014: Robust Arctic sea-ice influence on the frequent Eurasian cold winters in past decades. *Nature Geosci*, **7**, 869–873, https://doi.org/10.1038/ngeo2277.

Morrison, A. L., J. E. Kay, W. R. Frey, H. Chepfer, and R. Guzman, 2019: Cloud Response to Arctic Sea Ice Loss and Implications for Future Feedback in the CESM1 Climate Model. *Journal of Geophysical Research: Atmospheres*, **124**, 1003–1020, https://doi.org/10.1029/2018JD029142.

Mouginot, J., and Coauthors, 2019: Forty-six years of Greenland Ice Sheet mass balance from 1972 to 2018. *Proceedings of the National Academy of Sciences*, **116**, 9239–9244, https://doi.org/10.1073/pnas.1904242116.

Newman, M., and Coauthors, 2016: The Pacific Decadal Oscillation, Revisited. *Journal of Climate*, **29**, 4399–4427, https://doi.org/10.1175/JCLI-D-15-0508.1.

Nielsen, I. E., and Coauthors, 2019: Biogenic and anthropogenic sources of aerosols at the High Arctic site Villum Research Station. *Atmospheric Chemistry and Physics*, **19**, 10239–10256, https://doi.org/10.5194/acp-19-10239-2019.

Notz, D., and J. Stroeve, 2016: Observed Arctic sea-ice loss directly follows anthropogenic CO2 emission. *Science*, **354**, 747–750, https://doi.org/10.1126/science.aag2345.

——, and ——, 2018: The Trajectory Towards a Seasonally Ice-Free Arctic Ocean. *Curr Clim Change Rep*, **4**, 407–416, https://doi.org/10.1007/s40641-018-0113-2.

Olonscheck, D., T. Mauritsen, and D. Notz, 2019: Arctic sea-ice variability is primarily driven by atmospheric temperature fluctuations. *Nat. Geosci.*, **12**, 430–434, https://doi.org/10.1038/s41561-019-0363-1.

Pithan, F., and T. Mauritsen, 2014: Arctic amplification dominated by temperature feedbacks in contemporary climate models. *Nature Geosci*, **7**, 181–184, https://doi.org/10.1038/ngeo2071.

Polyakov, I. V., and Coauthors, 2020: Weakening of Cold Halocline Layer Exposes Sea Ice to Oceanic Heat in the Eastern Arctic Ocean. *Journal of Climate*, **33**, 8107–8123, https://doi.org/10.1175/JCLI-D-19-0976.1.

Previdi, M., K. L. Smith, and L. M. Polvani, 2021: Arctic amplification of climate change: a review of underlying mechanisms. *Environ. Res. Lett.*, **16**, 093003, https://doi.org/10.1088/1748-9326/ac1c29.

Rosenblum, E., and I. Eisenman, 2017: Sea Ice Trends in Climate Models Only Accurate in Runs with Biased Global Warming. *Journal of Climate*, **30**, 6265–6278, https://doi.org/10.1175/JCLI-D-16-0455.1.

Screen, J. A., and D. Williamson, 2017: Ice-free Arctic at 1.5 °C? *Nature Clim Change*, **7**, 230–231, https://doi.org/10.1038/nclimate3248.

Serreze, M. C., and J. A. Francis, 2006: The Arctic Amplification Debate. *Climatic Change*, **76**, 241–264, https://doi.org/10.1007/s10584-005-9017-y.

Sigmond, M., J. C. Fyfe, and N. C. Swart, 2018: Ice-free Arctic projections under the Paris Agreement. *Nature Clim Change*, **8**, 404–408, https://doi.org/10.1038/s41558-018-0124-y.

Smedsrud, L. H., M. H. Halvorsen, J. C. Stroeve, R. Zhang, and K. Kloster, 2017: Fram Strait sea ice export variability and September Arctic sea ice extent over the last 80 years. *The Cryosphere*, **11**, 65–79, https://doi.org/10.5194/tc-11-65-2017.

Smith, D. M., and Coauthors, 2019: The Polar Amplification Model Intercomparison Project (PAMIP) contribution to CMIP6: investigating the causes and consequences of polar amplification. *Geoscientific Model Development*, **12**, 1139–1164, https://doi.org/10.5194/gmd-12-1139-2019.

Spreen, G., L. de Steur, D. Divine, S. Gerland, E. Hansen, and R. Kwok, 2020: Arctic Sea Ice Volume Export Through Fram Strait From 1992 to 2014. *Journal of Geophysical Research: Oceans*, **125**, e2019JC016039, https://doi.org/10.1029/2019JC016039.

Swart, N. C., J. C. Fyfe, E. Hawkins, J. E. Kay, and A. Jahn, 2015: Influence of internal variability on Arctic sea-ice trends. *Nature Clim Change*, **5**, 86–89, https://doi.org/10.1038/nclimate2483.

Sweeney, A. J., Q. Fu, S. Po-Chedley, H. Wang, and M. Wang, 2023: Internal Variability Increased Arctic Amplification During 1980–2022. *Geophysical Research Letters*, **50**, e2023GL106060, https://doi.org/10.1029/2023GL106060.

Taylor, K. E., R. J. Stouffer, and G. A. Meehl, 2012: An Overview of CMIP5 and the Experiment Design. *Bulletin of the American Meteorological Society*, **93**, 485–498, https://doi.org/10.1175/BAMS-D-11-00094.1.

Taylor, P. C., M. Cai, A. Hu, J. Meehl, W. Washington, and G. J. Zhang, 2013: A Decomposition of Feedback Contributions to Polar Warming Amplification. *Journal of Climate*, **26**, 7023–7043, https://doi.org/10.1175/JCLI-D-12-00696.1.

Topál, D., and Q. Ding, 2023: Atmospheric circulation-constrained model sensitivity recalibrates Arctic climate projections. *Nat. Clim. Chang.*, **13**, 710–718, https://doi.org/10.1038/s41558-023-01698-1.

——, ——, J. Mitchell, I. Baxter, M. Herein, T. Haszpra, R. Luo, and Q. Li, 2020: An Internal Atmospheric Process Determining Summertime Arctic Sea Ice Melting in the Next Three Decades: Lessons Learned from Five Large Ensembles and Multiple CMIP5 Climate Simulations. *Journal of Climate*, **33**, 7431–7454, https://doi.org/10.1175/JCLI-D-19-0803.1.

Wang, M., and J. E. Overland, 2009: A sea ice free summer Arctic within 30 years? *Geophysical Research Letters*, **36**, https://doi.org/10.1029/2009GL037820.

Wills, R. C. J., Y. Dong, C. Proistosecu, K. C. Armour, and D. S. Battisti, 2022: Systematic Climate Model Biases in the Large-Scale Patterns of Recent Sea-Surface Temperature and Sea-Level Pressure Change. *Geophysical Research Letters*, **49**, e2022GL100011, https://doi.org/10.1029/2022GL100011.

Winton, M., 2011: Do Climate Models Underestimate the Sensitivity of Northern Hemisphere Sea Ice Cover? *Journal of Climate*, **24**, 3924–3934, https://doi.org/10.1175/2011JCLI4146.1.

Wu, F., W. Li, P. Zhang, and W. Li, 2021: Relative Contributions of Internal Atmospheric Variability and Surface Processes to the Interannual Variations in Wintertime Arctic Surface Air Temperatures. *Journal of Climate*, **34**, 7131–7148, https://doi.org/10.1175/JCLI-D-20-0779.1.

Wyburn-Powell, C., and A. Jahn, 2023: Large-scale Climate Modes Drive Low-frequency Regional Arctic Sea Ice Variability.

Chapter 2

An Optimal Atmospheric Circulation Mode in the Arctic Favoring Strong Summertime Sea Ice Melting and Ice–Albedo Feedback

I.T. Baxter, Q. Ding

Abstract

The rapid decline of summer Arctic sea ice over the past few decades has been driven by a combination of increasing greenhouse gases and internal variability of the climate system. However, uncertainties remain regarding spatial and temporal characteristics of the optimal internal atmospheric mode that most favors summer sea ice melting on low-frequency time scales. To pinpoint this mode, we conduct a suite of simulations in which atmospheric circulation is constrained by nudging tropospheric Arctic (60°–90°N) winds within the

Community Earth System Model, version 1 (CESM1), to those from reanalysis. Each reanalysis year is repeated for over 10 model years using fixed greenhouse gas concentrations and the same initial conditions. Composites show the strongest September sea ice losses are closely preceded by a common June–August (JJA) barotropic anticyclonic circulation in the Arctic favoring shortwave absorption at the surface. Successive years of strong wind-driven melting also enhance declines in Arctic sea ice through enhancement of the ice–albedo feedback, reaching a quasi-equilibrium response after repeated wind forcing for over 5–6 years, as the effectiveness of the wind-driven ice–albedo feedback becomes saturated. Strong melting favored by a similar wind pattern as observations is detected in a long preindustrial simulation and 400-yr paleoclimate reanalysis, suggesting that a summer barotropic anticyclonic wind pattern represents the optimal internal atmospheric mode maximizing sea ice melting in both the model and natural world over a range of time scales. Considering strong contributions of this mode to changes in Arctic climate, a better understanding of its origin and maintenance is vital to improving future projections of Arctic sea ice.

2.1 Introduction

The rapid decline of Arctic sea ice, seen in all months over the last four decades, has become one of the most prominent symbols of a warming world. Most climate models predict this warming will lead to the first occurrence of ice-free summers in the Arctic sometime in the 2030s–2040s in response to the rise of anthropogenic greenhouse gases in the atmosphere (Overland and Wang 2013; Liu et al. 2013; Jahn et al. 2016; Jahn 2018; Screen and Deser 2019; Sigmond et al. 2018; Notz and SIMIP Community 2020; Bonan et al. 2021a; Diebold and Rudebusch 2021; Wang et al. 2021). However, the range of when an ice-free Arctic Ocean

will likely occur and the rate of decline in sea ice cover is heavily influenced by low-frequency variability of the climate system (Kay et al. 2011; Winton 2011; Notz and Marotzke 2012; Wettstein and Deser 2014; Zhang 2015; Swart et al. 2015; England et al. 2019; Bonan et al. 2021b) that is believed to be partially driven by natural SST variability in the tropics and extratropics (Screen and Deser 2019; Baxter et al. 2019; Bonan and Blanchard-Wrigglesworth 2020). Studies attempting to understand the extent of this contribution have suggested that internal variability may have accounted for 30%–50% of Arctic sea ice decline over the past 40 years (Stroeve et al. 2007; Kay et al. 2011; Stroeve et al. 2012; Zhang 2015; Ding et al. 2019; England et al. 2019) through impacts on large-scale atmospheric and oceanic processes in and around the Arctic. Oceanic processes associated with wind-driven gyre circulations and import of warm, salty water from lower latitudes has been linked to Arctic sea ice changes on decadal time scales (Lindsay and Zhang 2005; Polyakov et al. 2020). However, internally driven wind changes may only require several years to exert a melting impact on sea ice through atmospheric processes. Atmospheric circulation may be able to melt a substantial amount of Arctic sea ice within only a few years, such as the 6-yr period from 2007 to 2012 and strongly modulate anthropogenic impacts over the same time periods (Baxter et al. 2019). However, it remains quantitatively unclear how much sea ice loss during 2007–12 is due to wind forcing.

During the melt season, sea ice loss is determined by changes in surface radiative fluxes and temperature over the sea ice in addition to mechanical breakup and export of ice out of the Arctic (Ding et al. 2019; Olonscheck et al. 2019; Papritz 2020). Statistical analysis of reanalysis products has shown persistent anticyclonic circulation over the Arctic during summer can induce adiabatic descent of air from the middle to upper troposphere that can

warm the near-surface atmosphere, enhancing downward longwave radiative fluxes and melting sea ice (Baxter et al. 2019; Papritz 2020). This summertime anticyclonic circulation can also strongly influence cloud cover, altering downwelling radiation at the surface (Huang et al. 2021), as well as enhance export of ice through the Fram Strait (Smedsrud et al. 2017; Spreen et al. 2020). It was found that air masses with anticyclonic circulation produced clear-sky conditions in their center and cloudy conditions at their edges, leading to a complex combination of downwelling radiative fluxes dispersed around the anticyclone on a broad range of time scales (Wernli and Papritz 2018; Huang et al. 2021).

Although progress has been made to improve our physical understanding of the processes by which atmospheric circulation influences sea ice, the limited predictability of these processes in climate models constrains robust forecasts of end of summer sea ice to around June at best (Bushuk et al. 2020). Though recent Arctic sea ice change is dominated by a long-term decreasing trend, strong interannual variability is seen in the sea ice record, especially in the past decade, illustrated by the dispersion of extreme events such as the low sea ice cover events in 2007, 2012, 2016, 2019, and 2020 and the sea ice maximum event in 1996. Most current models have limited skill in predicting these interannual changes beyond a few months lead time and may struggle more in the future if thinner ice becomes more sensitive to atmospheric chaotic variability (Holland and Stroeve 2011; Wang et al. 2013; Msadek et al. 2014). We do not know to what degree these limitations are a result of current models' inability to capture important internal atmospheric processes in the polar regions and whether these internal processes possess some large-scale features that we can focus on to overcome the limited predictability of sea ice forecasts.

Many well-known modes of climate variability have been linked to Arctic sea ice loss, including the Pacific decadal variability (PDV), interdecadal Pacific oscillation (IPO), Atlantic multidecadal variability (AMV), and North Atlantic Oscillation (NAO) (Ogi et al. 2003; Meehl et al. 2018; Baxter et al. 2019; Screen and Deser 2019). Although internal atmospheric variability has been long known to have impacts on sea ice in observations, it is still unclear whether there exists an optimal internal mode that favors the strongest sea ice decline in the Arctic and the key mechanism through which this mode regulates sea ice variability. This question cannot be fully answered by diagnostic studies of observed records since so many driving forces of sea ice are mixed and the observed sea ice changes thus represent a combination of responses to forcing originating from different sources. To address these questions, we conduct a set of nudging simulations by specifying observed winds into a fully coupled model to assess the sensitivity of the sea ice response to different wind patterns. We believe this strategy is unique in that it may pave new ground and develop a new perspective for studying the Arctic sea ice response to internal climate variability in climate models.

2.2 Strategy, Data and Methods

Because large-scale circulation variability is believed to be most representative of internal viability in the high latitudes (Deser et al. 2012; Shepherd 2014; Ding et al. 2017), a model's response to these observed winds may help us detect the optimal circulation mode that can excite the most significant sea ice change in the model. Once these modes can be identified in our nudging runs, we will then conduct an examination of the radiative fluxes and contributions to thermodynamic and dynamic ice loss associated with this mode and a comparison with observations that may shed more light on the fundamental mechanism contributing to sea ice

variability in reality and climate models. The simulated sea ice response to this optimal mode in the nudging runs may also aid us to better estimate the largest magnitude of sea ice melting that could be attributed to internal atmospheric variability and thus constrain the uncertainty in projecting the occurrence of the first ice-free summer in the Arctic under different future warming scenarios. One limitation of our nudging simulations is that reliable reanalysis winds with 6-h temporal resolution in the Arctic only covers the recent 40 years, which is likely too short to reflect a full spectrum of all possible internal variability due to winds and may also contain imprints of anthropogenic forcing. Therefore, diagnostic analysis is also performed on a long (1800-yr) preindustrial simulation and 400-yr paleoclimate proxy data assimilated reconstructions reaching back to the seventeenth century to search for a circulation pattern that is closely associated with the strongest sea ice melting and warming epochs in the Arctic prior to the influence of anthropogenic emissions. These approaches using three independent data sources may improve our understanding of the common features of the optimal mode across different products and the sensitivity of this type of mode to anthropogenic forcing.

2.2.1 NSIDC sea ice and ERA-Interim reanalysis

We examine monthly sea ice concentrations derived from Goddard edited passive microwave retrievals that have been compiled by the National Snow and Ice Data Center (NSIDC; Cavalieri et al. 1996; Fetterer and Knowles 2004). Our analysis is based on comparisons between total sea ice area (SIA) from the NSIDC and model simulations. Total sea ice volume and average sea ice thickness show consistent changes to SIA; therefore, we focus on SIA for simplicity. Total SIA is defined as the summed total of the product of the grid element area and sea ice concentration (>15%) in each Arctic grid cell. Total September SIA

is primarily used to represent the annual minimum and aggregation of the preceding melt season. For winds and other atmospheric variables, we use the European Centre for Medium-Range Weather Forecasts (ECMWF)'s ERA-Interim (ERA-I; Dee et al. 2011) product. The ERA-I product has been evaluated over the Arctic in the previous studies, including surface temperature, radiative fluxes, precipitation, wind speed, and cloud properties (Lindsay et al. 2014; Graham et al. 2019; Wang et al. 2019).

2.2.2 CESM1-LE and long preindustrial control simulation

As a comprehensive resource for studying climate change in the presence of internal climate variability, the Community Earth System Model Large Ensemble (CESM1-LE; Kay et al. 2015) is run with fully coupled atmosphere, ocean, land, and sea ice components from 1920 to 2100. We use the mean of the 40 ensemble members, simulated using the same model and external forcing but with small round-off level variations in their initial air temperature field, as representative of our best estimate of the anthropogenically forced changes in total September SIA. To quantify the range of internal variability in the same model, we use 1800 years of the preindustrial (1850) fully coupled simulation, that uses fixed greenhouse gases to simulate internal processes inherent to the CESM1. Both the CESM1-LE and preindustrial control simulations use a nominal 1° resolution in the atmosphere model. CESM1 has shown an ability to capture general features of Arctic temperature, humidity, clouds, radiation, and sea ice. Particularly, the CESM1 simulated seasonal cycle of Arctic sea ice extent and the spatial distribution of sea ice thickness matches well with observations in the late twentieth century (Labe et al. 2018; England et al. 2019).

2.2.3 EBAF surface and TOA radiative fluxes

To compare the radiative flux response to nudged winds in the CESM1 experiments we compare with the monthly and 1° × 1° spatial resolution CERES EBAF-Surface Edition 4.1 radiative fluxes (EBAF). EBAF surface fluxes were calculated using the Langley modified Fu–Liou radiative transfer model with inputs from MODIS retrieved cloud properties, adjusted CERES outgoing TOA fluxes, meteorological data from NASA GMAO reanalysis, and aerosol data from an aerosol assimilation system. EBAF fluxes have been considered as a key benchmark for evaluating simulations of the Arctic radiation budget by previous studies (Boeke and Taylor 2016; Christensen et al. 2016; Huang et al. 2017).

2.2.4 EKF400v2 and PHYDA Global Paleo-reanalysis

We use the EKF400 version 2400-yr paleo-reanalysis reconstruction dataset, which utilizes an ensemble Kalman fitting method to assimilate multiple observations (including instrumental observations, historical climate indices, and proxy data) with the ECHAM5.4 AGCM simulations (EKF400; Franke et al. 2017). This dataset provides monthly 500 hPa geopotential height (Z500) and surface temperatures over the period from 1603 to 2003, which allows us to better examine global circulation variability in each season over the past 400 years. In the ERA-I and EKF400 products, the detrended correlation between JJA Z500 and JJA surface temperature is 0.52 (1979–2018, ERA-I) and 0.59 (1600–1920, EKF400), respectively. The correlation between ERA-I JJA Z500 and NSIDC total September SIA is −0.54 (1979–2018, detrended). Observations and proxy data are taken from only over land. From 1600 to 1800, tree-ring width and maximum latewood density constitute the majority of the assimilated data outside of Greenland and Europe at high latitudes and are only assimilated from April to

September. Instrumental station data from southern Greenland and northern Europe become more prominent after 1800 and are available year-round. We compare surface temperatures from EKF400 with those from the Paleo Hydrodynamics Data Assimilation product (PHYDA; Steiger et al. 2018) to confirm we are obtaining a consistent signal from the proxy data. PHYDA, an updated version of the Last Millennium Reanalysis (LMR2; Tardif et al. 2019), assimilates PAGES2k proxy records into bias-corrected output from the CESM1 Last Millenium Ensemble (CESM1-LME; Otto-Bliesner et al. 2016). The CESM1-LME uses the same model as the CESM1-LE but with ∼2° atmosphere and land components. Brennan and Hakim (2022) have used a similar paleoclimate proxy data assimilation framework based on LMR2 in skillful reconstructions of annual mean Arctic sea ice using surface air temperature and sea ice concentration from the same model priors as the two products shown in this study. In these reconstructions much of the variance and skill comes from regions closest to land-based proxy records in the PAGES2k database that are also assimilated into EKF400 and PHYDA, suggesting that the most important information for sea ice reconstructions is coming from these proxies via surface air temperatures, which should lend confidence in establishing the connections between atmospheric circulation and surface changes in the Arctic since the year 1600. This may introduce biases in the reconstruction of sea ice and surface temperature further away from these land-based proxy records, such as in the central Arctic. The sea ice state may have been different prior to the rise of anthropogenic forcing in the mid twentieth century, and the sea ice sensitivity to atmospheric circulation and surface temperature changes may not have behaved exactly as it has in recent decades. When examining these reconstructions, we focus on the 10-yr non-overlapping periods of EKF400 JJA Z500 and its

relationship with JJA surface temperatures from EKF400 (r = 0.81) and PHYDA (r = 0.68) as well as annual mean total SIA from Brennan and Hakim (2022, r = −0.52).

2.2.5 CESM1.2.2.1 nudging experiment design

Previous work by Huang et al. (2021), nudging winds in the CESM1 from 2000 to 2016, found an important role of atmospheric circulation variability in contributing to observed low-level clouds in the Arctic. Li et al. (2022) and Roach and Blanchard-Wrigglesworth (2022) also used a similar nudging approach to quantify the contribution from wind forcing to recent trends in Arctic upper ocean warming and sea ice, respectively. In this study, we seek to build on the concepts employed in Huang et al. (2021), Li et al. (2022), and Roach and Blanchard-Wrigglesworth (2022) by nudging high latitude winds in the Community Earth System Model version 1.2.2.1 (CESM1, see Table 2.1; Hurrell et al. 2013) over the period from 1979 to 2018, using the same resolution (~1°) and components as the CESM1-LE (CESM1.1.1), with an emphasis on the sea ice response. The goal of these experiments is to examine the role of tropospheric wind patterns on Arctic sea ice; therefore, we nudge above ~850 hPa, allowing the surface and lower troposphere to interact with one another. This level was decided based on correlations between total September sea ice and Arctic-averaged (70°–90°N) geopotential heights, which are limited to above ~800 hPa in the reanalysis (Supplementary Fig. A3). We find that extending nudging down to the surface does not alter these results or their conclusions (not shown). To nudge the model to ERA-I horizontal winds, we follow the methodology from Blanchard-Wrigglesworth et al. (2021):

$$\frac{dx}{dt} = F(x) + F_{nudge}$$

$$F_{nudge} = \alpha[O(t'_{next} - x(t))]/\tau$$

where $x(t)$ is the model state vector at the model time step t; $F(x)$ is the internal tendency of the system with no nudging; and F_{nudge} is the nudging term, proportional to the difference between the target analysis (ERA-I horizontal winds) at a future analysis time step, $O(t'_{\text{next}})$, and the model state at the current model time step, $x(t)$. In the atmosphere, the analysis that the model is nudged toward is updated every 6 h (the analysis time step t' next) while F_{nudge} is adjusted at each model time step (in CAM5, Δt = 30 min). The nudging coefficient α is set to an intermediate strength (0.5) everywhere within the nudging domain to further allow the model's own variability to influence the circulation pattern, though the results do not show a sensitivity to nudging factors (ranging from 0 to 1) greater than 0.5 (Huang et al. 2021).

Name	Model	Domain	Reanalysis	Description
Continuous	CESM1.2.2.1	60°–90°N < 850 hPa fixed CO2 (397 ppm)	ERA-Interim, 1979–2018	10-member nudging runs to continuous 40-yr reanalysis record branched from member of CESM1-LE
Perpetual	CESM1.2.2.1	60°–90°N < 850 hPa fixed CO2 (397 ppm)	ERA-Interim, 1979–2018	40-member nudging runs repeating each reanalysis year (1 Jan–31 Dec) for 10–21 model years each from same init. conditions branched from same member of CESM1-LE

Table 1.1: Nudging Simulations Descriptions

Nudging experiment design. Model and nudging specifications for perpetual and continuous nudging simulations in the CESM1.2.2.1 using fixed CO2 concentrations (367 ppm).

2.2.6 Continuous (10-member, 40-yr simulations)

To examine the model's capability in replicating some features of observed sea ice changes over the past 40 years, we first run a 10-member ensemble of 40-yr continuous simulations with winds nudged to reanalysis from 1979 to 2018 and fixed greenhouse gas concentrations at the level of the year 2000 (367 ppm), which are very close to the mean concentrations of greenhouse gases over the period. These simulations suggest that the model has a reasonable skill to capture some features of the observed sea ice decline since 1979 under continuous wind

forcing (see section 3a for more details). We test the sensitivity of our wind nudging approach to CO2 forcing by conducting the same continuous nudging experiments with time-evolving CO2 concentrations during the period 1979–2018 (not shown). While we find that the overall trends are more negative with increasing CO2 concentrations, the year-to-year variability in total September SIA remains unchanged, suggesting a relatively small influence of CO2 forcing on our analysis of the perpetual wind nudging simulations described in the following section.

2.2.7 Perpetual simulations (40-member, 10–21-yr simulations)

One limitation of the continuous simulation is that it is unclear whether strong melting over some years is due to winds over immediately preceding periods, or an accumulation of changes induced by winds occurring previously. Arctic sea ice likely has memory that can last for several years through the persistence of thickness changes and absorption of heat in the ocean that can complicate our understanding of the sea ice response to wind patterns associated with a specific year (Blanchard-Wrigglesworth et al. 2011; Tietsche et al. 2011). Repetitively forcing the model with winds from the same year may overcome this limitation and provides a new opportunity to search the optimal internal mode favoring the strongest sea ice melting.

To do so, we separate the ERA-Interim record into individual years and conduct 40 additional perpetual simulations using the same configuration (Table 1; e.g., the nudging parameter and domain, and anthropogenic forcing: year 2000). In each simulation, the model is integrated for 10 years, with atmospheric circulation within the Arctic (60°–90°N) repeatedly nudged to the ERA-Interim 6-hourly wind field from an individual year in the

reanalysis. All simulations are initialized from identical conditions, branched from the same member of the CESM1-LE that is representative of moderate conditions in terms of its sea ice area and volume in 2000/1/1 among a total of 40 members. By repeating the same wind pattern for consecutive model years, the responses of sea ice and other characteristics of the Arctic climate to circulation changes are enhanced, making them easier to differentiate from confounding processes. We can then better assess the mechanisms resulting from atmospheric circulation variability affecting Arctic sea ice cover at the end of the melt season for each year. This perpetual approach also partially compensates for issues associated with initialization, since memory associated with initial conditions is likely limited to 3–4 years (Blanchard-Wrigglesworth et al. 2011), and greenhouse gas forcing, which is the same in all runs. Atmospheric carbon dioxide concentrations are fixed at the same concentration as the continuous nudging simulations (367 ppm).

For some perpetual runs that have the strongest melting and strongest growth in September sea ice over the 10 years we extend the simulations to 21 years under wind forcing of the same year [Table 2.2]. For these reanalysis years, extending the length of integration ensures that Arctic sea ice has stabilized in response to the nudged wind patterns and provides a quasi-equilibrium response to imposed wind forcing.

Product	Strong melting years ($\leq 1\sigma$)	Strong growth years ($\geq 1\sigma$)
Perpetual nudging	1993, 2007, 2011, 2012, 2015	1996, 2001, 2002, 2010, 2017
NSIDC (detrended, ERA-I years)	1979, 1990, 2007, 2008, 2012	1992, 1994, 1996, 2001
NSIDC (detrended, EBAF years)	2007, 2008, 2012	2001, 2014

Table 2.2: Extreme years in perpetual nudging simulations

Extreme sea ice years from 10-yr nudging simulations. Composites in Figs. 2.1–4 are based on the mean of the five low sea ice years minus the mean of the five high sea ice years in total September SIA from the perpetual nudging simulations and NSIDC sea ice concentration product. Low sea ice and high sea ice years are calculated using periods matching ERA-I (1979–2018) and EBAF (2000–18) availability.

2.3 An optimal sea ice melting mode in the nudging simulations

2.3.1 Strong and weak sea ice melting years determined by different wind patterns

We first examine the continuous 40-yr simulation (see methods) using the same nudging domain and fixed greenhouse gas concentrations (Fig. 2.1a) but with nudged winds varying from 1979 to 2018. The continuous simulations agree well with observed sea ice changes from the NSIDC (detrended r = 0.58, raw r = 0.65, Fig. 2.1a). Considering the optimal conditions for low Arctic sea ice years, the imposed wind patterns in the continuous 40-yr simulations capture many of the important features of total September SIA observed in recent decades (extreme years, rapid decline from 1996 to 2012, year-to-year fluctuations, significant decline since the early 2000s). The nudging simulations deviate from the observed sea ice changes in the early 1990s, possibly due to a lack of aerosol cooling from the Pinatubo eruption in our wind-only constrained nudging simulations (Lehner et al. 2015; Yang et al. 2019; Brennan and Hakim 2022), the use of year 2000 initial conditions and CO2 concentrations, or issues in the assimilated data. During this period there is also an increase in total September SIA in the forced response of the CESM1-LE reflecting a cooling effect from aerosols (green curve in Fig. 2.1a).

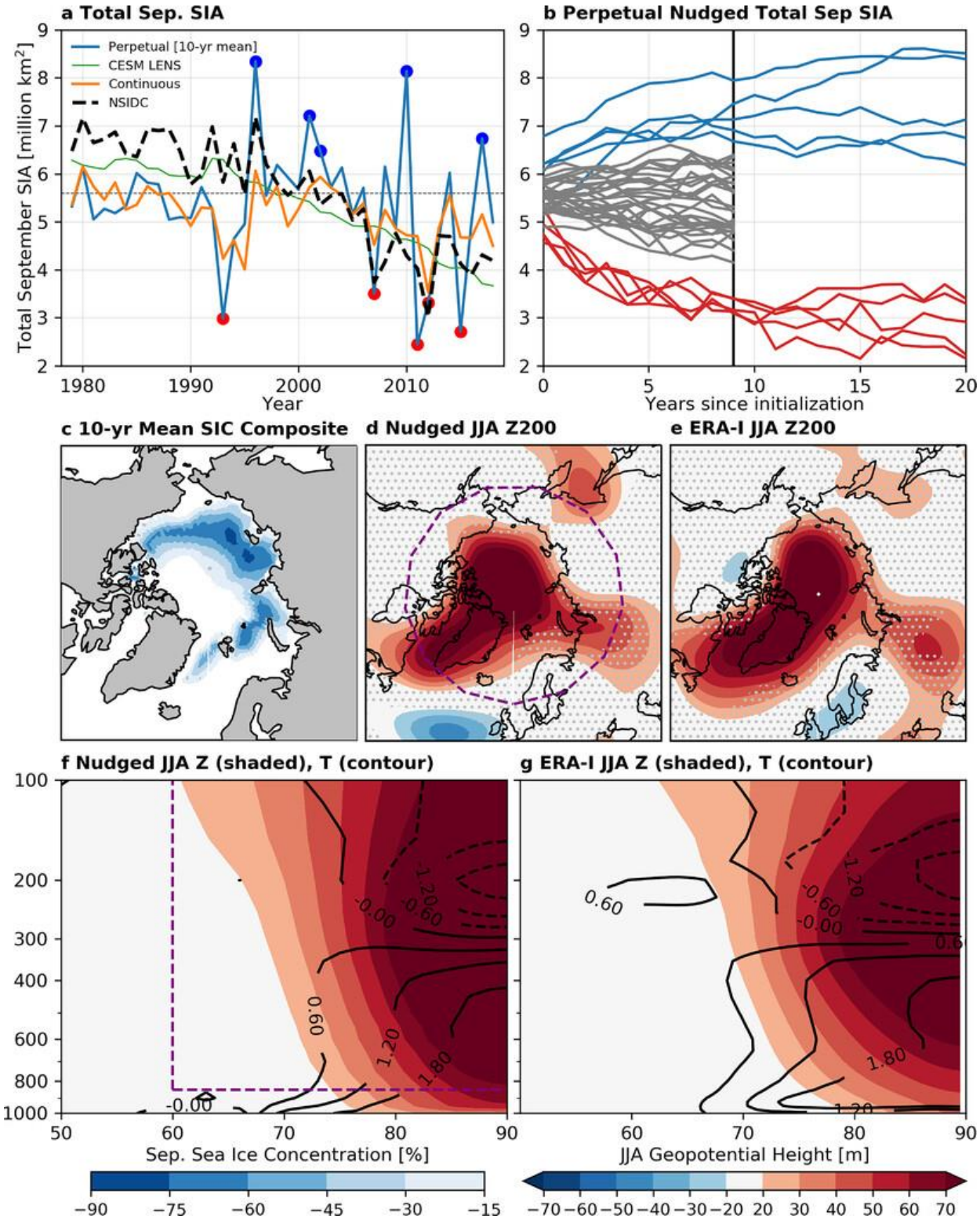

Figure 2.1 Composites of nudging simulations and reanalysis. (a) Total September SIA from the CESM1-LE (LENS, green), NSIDC (dashed black), 10-member mean from the continuous simulations (orange), and 10-yr means from the perpetual simulations (blue). In (a), red dots

show the low sea ice years and blue dots show the high sea ice years from the perpetual nudging simulations. (b) Total September SIA from the perpetual simulations. In (b), red lines represent the low sea ice group, blue lines represent the high sea ice group, and the gray curves represent all remaining years. (c) 10-yr-mean composites of sea ice concentration, (d) JJA 200 hPa geopotential height, and JJA zonal mean geopotential height (shading) and (f) temperature (contours) based on the years from the low sea ice group minus the high sea ice group in the perpetual simulations [row 1 in Table 2, red minus blue in (a)]. Composites of (e) JJA 200 hPa geopotential height and (g) JJA zonal mean geopotential height (contours) and temperature (shading) based on the low sea ice years minus the high sea ice years in the detrended NSIDC record (row 2 in Table 2). Dashed purple contours indicate the nudging domain within the Arctic (60°–90°N) and above ~850 hPa. Stippling indicates composite differences are not statistically significant at the 95% confidence level based on a two-sample Student's t test.

We then separate the wind patterns from each year into its own simulation and repeat the same nudging for 10–21 years to magnify the wind patterns over individual years. This set of experiments will be referred to as the perpetual simulations (see methods). The model exhibits very different behavior across these 40 perpetual simulations with some runs experiencing a strong sea ice decline and some with substantial ice growth. Since the only difference in forcing imposed in these runs is large-scale winds in the Arctic, the bifurcation of these sea ice changes is primarily due to wind forcing.

In the perpetual nudging simulations, sea ice responds quickly to changes in atmospheric forcing. As can be seen by first year total September SIA between the different runs (Fig. 2.1a), sea ice characteristics diverge within the initial year in response to wind forcing. This difference increases to around 4 million km2 in the first 10 years when repeating these wind patterns (red lines in Fig. 2.1b). The largest observed declining trend over any periods long than 10 years in total September SIA (−2.0 million km2 decade^{-1}) is from 2000 to 2012 (black line in Fig. 2.1a), which is well captured by the perpetual nudging experiments (blue line in Fig. 2.1a), with the largest 13-yr declining trend (2000–12, blue line) in the 10-yr means of the perpetual nudging simulation occurring during the same period with a similar magnitude of

−1.7 million km2 decade^{-1}. The largest declining trend over any periods longer than 10 years in the ensemble mean of the CESM1-LE is much lower than the observations (−1.1 million km2 decade^{-1}) and does not show the rapid acceleration from 1996 to 2012 or the slowed decline thereafter as seen in the observations and nudging simulations, indicating that the rise of CO2 forcing over the same period (around 2 ppm yr^{-1}) cannot solely explain this decline. Instead, the largest 13-yr decline in the CESM1-LE ensemble mean is from 2006 to 2018, likely associated with the sea ice state (Holland et al. 2019) and the transition from historical to RCP8.5 forcing. Year-to-year variability in the 10-yr means from these perpetual nudging simulations also agrees with total September SIA from the NSIDC (detrended r = 0.50, Fig. 2.1a).

We begin by compositing based on the means of the first 10 years of total September SIA loss in each member of the perpetual simulations. The results are insensitive to the approach for quantifying sea ice loss, with the 10-yr means, 10-yr trends, and final (year 10 or 21) total September SIA, as well as using total sea ice volume or average sea ice thickness. Nudging winds from 1993, 2007, 2011, 2012, and 2015 produce the strongest declines above one standard deviation in total September SIA and are defined as the low sea ice group (Table 2.2). Though many of the years in the low sea ice group coincide with the lowest observed years, it should be noted that the 2015 and 1993 simulations experienced strong simulated sea ice loss but are not among the lowest recorded years, suggesting there is likely confounding effects from the sea ice and ocean states, previous years, or other unaccounted processes (e.g., moisture and heat transport from the lower latitudes to the Artic by the atmosphere and ocean) in the real world that are critical in determining the observed sea ice state in each year. In addition, low sea ice cases in the perpetual simulations reflect an amplified response of sea ice

to specified winds over a 10-yr period in the model. However, in nature, the same wind patterns can only apply this forcing on sea ice in a short 1-yr time window in the presence of many other forcings. This amplification along with fixed greenhouse gas concentrations in the nudging simulations likely explains some of the mismatch in the rankings of these extreme melting years between the simulations and observations.

In the perpetual simulations, nudging winds from 1996, 2001, 2002, 2010, and 2017 generates the strongest growth in total September SIA over 10 years and are defined as the high sea ice group. 1996 stands out as a particularly strong sea ice growth outlier and is the highest recorded total September sea ice year in the satellite record. Four out of the five same years also constitute the low sea ice and high sea ice members in terms of total volume and average thickness of September Arctic sea ice in these simulations (Supplementary Fig. A1).

Compositing sea ice concentration based on the sea ice change groups yields a relatively uniform difference across the Arctic, likely resulting from contributions associated with thermodynamic processes (i.e., radiative fluxes, albedo) as well as mechanical break up and export. The composites show the greatest differences in the East Siberian–Laptev–Kara Sea regions and a weak increasing signal along the eastern coast of Greenland during low sea ice years. These regions with strong sea ice decline in response to wind forcing are also the regions seeing strong sea ice melting trends over recent decades in observations (Baxter et al. 2019).

2.3.2 Local atmospheric, radiative, and sea ice melting processes associated with strong melting summers

In observations and the continuous nudging simulations, autocorrelations of total September SIA with SIA in the preceding months only show statistically significant

coefficients with June–August (JJA) sea ice (Supplementary Fig. A2). In the nudging simulations, there is a statistically significant pattern in regressions of observed JJA Arctic geopotential height and temperature onto total September SIA but no statistically significant pattern in January–May (Supplementary Fig. A3). This phenomenon has been referred to as the spring predictability barrier for September Arctic sea ice (Bushuk et al. 2020). To maintain consistency with the observed relationship, we focus on JJA atmospheric circulation. Composites of JJA 200 hPa geopotential height in both the perpetual nudging experiments and ERA-I, constructed using the definition of the low sea ice and high sea ice years (Table 2.2), show a prominent "Figure-8" anticyclonic patterns with centers over southwest Greenland and the central Arctic in the strongest melting years relative to the sea ice growth years consistent with the regression pattern from ERA-I (Figs. 2.1d,e). Friction at the surface of the anticyclone generates large-scale subsidence throughout the mid- to lower troposphere, consistent with the reanalysis, but with differences in the vertical structure near the surface below the nudging domain (Figs. 2.1f,g). Adiabatic descent of air induces warming and moistening (not shown, Ding et al. 2017) of the lower Arctic atmosphere that then increases the emission of longwave radiation. The strong similarity between the vertical structure of atmospheric fields n the nudging run and ERA-I indicates that wind forcing is critical in governing changes of tropospheric temperature in the Arctic, which is essential for determining radiation in the entire air column, as well as sea ice and upper-ocean temperature variability.

Despite the anticyclonic-dominated regime seen in the composites, there is an increase in low cloud cover along the Eurasian coast (not shown), consistent to the analysis in Huang et al. (2021). Huang et al. (2021) argue that the high pressure may increase the low-level clouds throughout much of the Arctic through advection and subsidence-induced entrainment of

moisture into the inversion layers. However, we do not go into detail on cloud radiative effects in these simulations because there are well-documented biases in microphysical and boundary layer processes that may lead to the differences seen between the products (Sotiropoulou et al. 2016; Tan and Storelvmo 2019; McIlhattan et al. 2020).

To better understand the radiation balance associated with the melting process in the perpetual nudging runs, we compare the simulated radiation fluxes at the surface and TOA in the Arctic with their observed counterparts in ERA-I and EBAF. Since EBAF is only available after 2000 and the sample size of the extreme sea ice melting/growth years over this period is smaller (Table 2.2), the composite using EBAF may contain large uncertainty or be biased by changes in certain individual years, and sensor-related artifacts, especially in the computed surface fluxes.

Since the radiation response in our nudging simulations represents an extreme scenario in which winds have a chance to solely regulate the radiation fields over 10 years, there are discrepancies among the three datasets. At the surface, the three products show consistent signals for most fluxes (Fig. 2.2a; Supplementary Fig. A5). Enhanced downwelling LW (LW_{down}) and less reflected SW (SW_{up}) in JJA appear to be the two main components contributing to a gain of heat at the surface, conducive for strong sea ice melting. As expected, JJA atmospheric anticyclonic circulation anomalies can enhance downwelling LW and the ice–albedo feedback is triggered, explaining less reflected SW. The ice–albedo feedback in these simulations also includes conversion of the ice surface from snow to bare ice and melt ponds as the enhanced shortwave absorption is uniformly distributed wherever there is sea ice not just sea ice loss (Figs. 2e,h). In the meantime, the impacts of less reflected SW at the surface are also translated to the TOA to reduce upwelling SW. Thus, the ice–albedo feedback which

is triggered by winds plays a key role in determining the radiation balance in the Arctic atmosphere in summer.

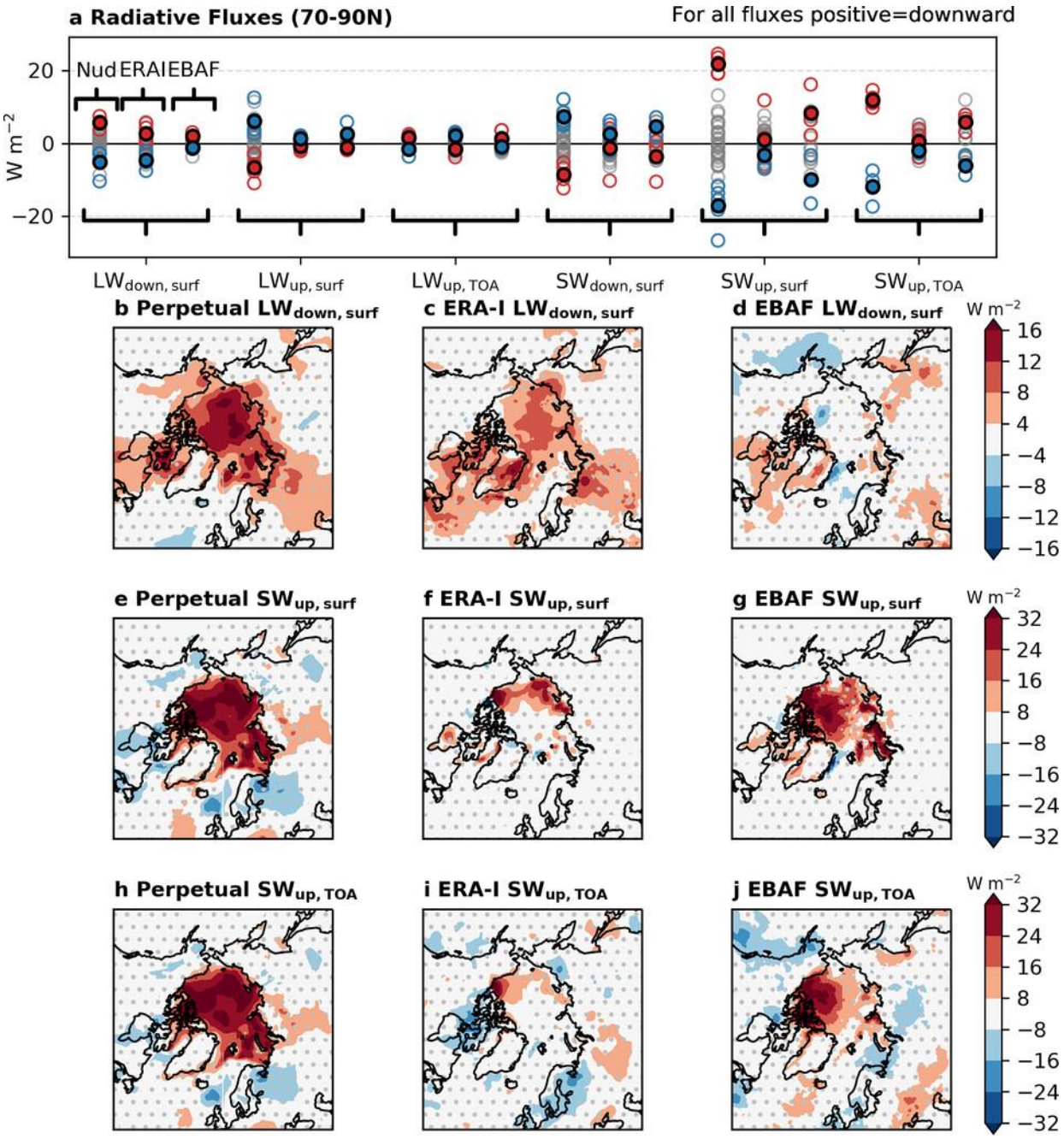

Figure 2.2 Surface radiative flux response to nudged winds. (a) JJA surface and TOA radiative fluxes averaged within the Arctic (70°–90°N) from the perpetual nudging simulations, ERA-Interim, and EBAF. Filled circles indicate low sea ice (red) and high sea ice (blue) group means. Low sea ice years minus high sea ice years JJA (b)–(d) downwelling surface longwave,

(e)–(g) upwelling surface shortwave, and (h)–(j) upwelling TOA shortwave radiative fluxes from (left) the perpetual nudging simulations, (center) ERA-Interim, and (right) EBAF. Stippling in (b)–(j) indicates where differences are not statistically significant at the 95% confidence interval according to a two-sample Student's t test. Groups for low sea ice years and high sea ice years are based on years listed in Table 2. For all fluxes shown here, positive values indicate downward fluxes into the surface.

To better illustrate the radiation balance at the surface and the TOA, we mainly focus on LW_{down} and SW_{up} at the surface and SW_{up} at the TOA (Figs. 2b–j). Downwelling longwave radiation at the surface is enhanced during years of strong sea ice melting throughout the Arctic in the perpetual nudging simulations and ERA-I (Figs. 2b,c). It is not as strong in EBAF likely due to differing impacts of clouds between these products (Fig. 2d). In the perpetual nudging simulations, strong shortwave absorption occurs throughout the Arctic, wherever there is sea ice or snow cover loss and melt pond formation (Fig. 2e). However, in ERA-I and EBAF, significant surface shortwave absorption primarily takes place in the Beaufort Sea (Figs. 2e,f). EBAF has a stronger signal of shortwave absorption in the Beaufort region than ERA-I near the center of anticyclonic circulation in certain low sea ice years (Kay et al. 2008; Wernli and Papritz 2018). The spatial patterns of SW_{up} at the TOA closely resembles that at the surface (Figs. 2h–j). This signal reaches the TOA throughout the Arctic in the perpetual simulations and in particular the Beaufort Sea in both ERA-I and EBAF. In all products, under the control of strong atmospheric anticyclonic winds during years of summertime sea ice loss, more shortwave absorption at the surface due to the ice–albedo feedback dominates the surface and TOA radiative budgets (Figs. 2e–j).

We separate the shortwave feedbacks resulting from changes in surface albedo and cloud optical properties using the approximate partial radiative perturbation method (APRP, Taylor et al. 2007). The differences between the low sea ice years and high sea ice years are dominated by the surface albedo feedbacks from March to October, peaking in July (Fig. 2.3). Changes

in cloud radiative effects, associated with anticyclonic circulation slightly contribute to increased surface shortwave absorption during June and July, but decreased absorption in August, that may be associated with decreased cloud cover above 900 hPa (Huang et al. 2021). Over 20 years of the perpetual simulations, the surface albedo feedback more than doubles, while the cloud and atmospheric components remain relatively small (Fig. 2.3b).

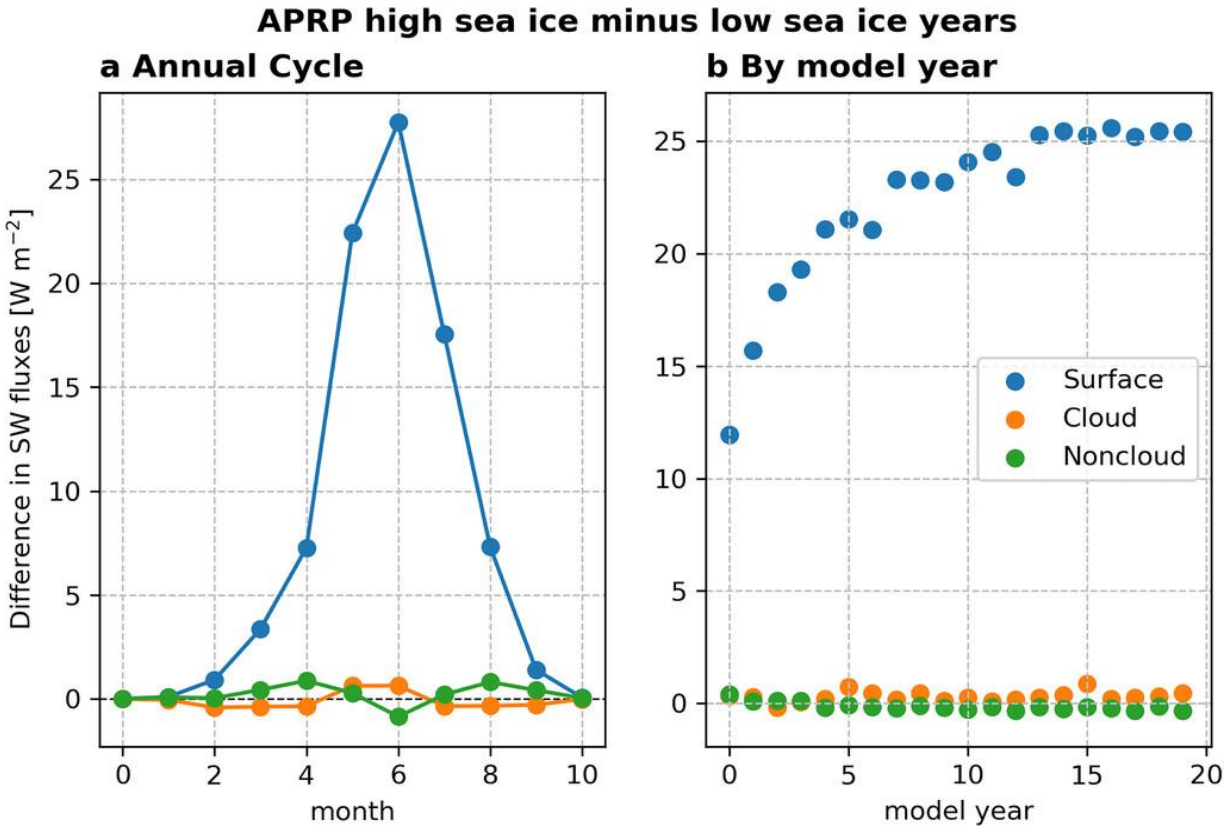

Figure 2.3 APRP differences in low sea ice minus high sea ice years. (a) Monthly differences in surface, cloud, and atmospheric scattering/absorption obtained using APRP analysis between low sea ice and high sea ice years from the last 10 years of the perpetual simulations. (b) APRP differences in surface, cloud, and atmospheric scattering/absorption between low sea ice and high sea ice years for each year of the perpetual nudging simulations.

Next, we shift our focus to the melting processes that contribute to decreased surface albedo through strong sea ice loss in the perpetual nudging simulations as these processes cannot be easily quantified from available observations and reanalysis. In low sea ice years, top melting

primarily occurs near the sea ice edge in June and throughout the Artic during July in response to warmer temperatures, downwelling longwave radiation, and shortwave absorption (Fig. 2.4). Years with the most extreme top melting in July coincide with the same years that are in the low sea ice and high sea ice years in terms of total September SIA, leading to a difference in melting of up to 1.5 cm day−1 in the Pacific Arctic. This correspondence with total September SIA is not seen in other months or in bottom and lateral melting, indicating that July is the month in which the ice–albedo feedback is the most active and sensitive, as it coincides with the peak of incoming solar radiation at the TOA and the mean state of sea ice is thinner and more fragile (little snow, extensive melt ponds).

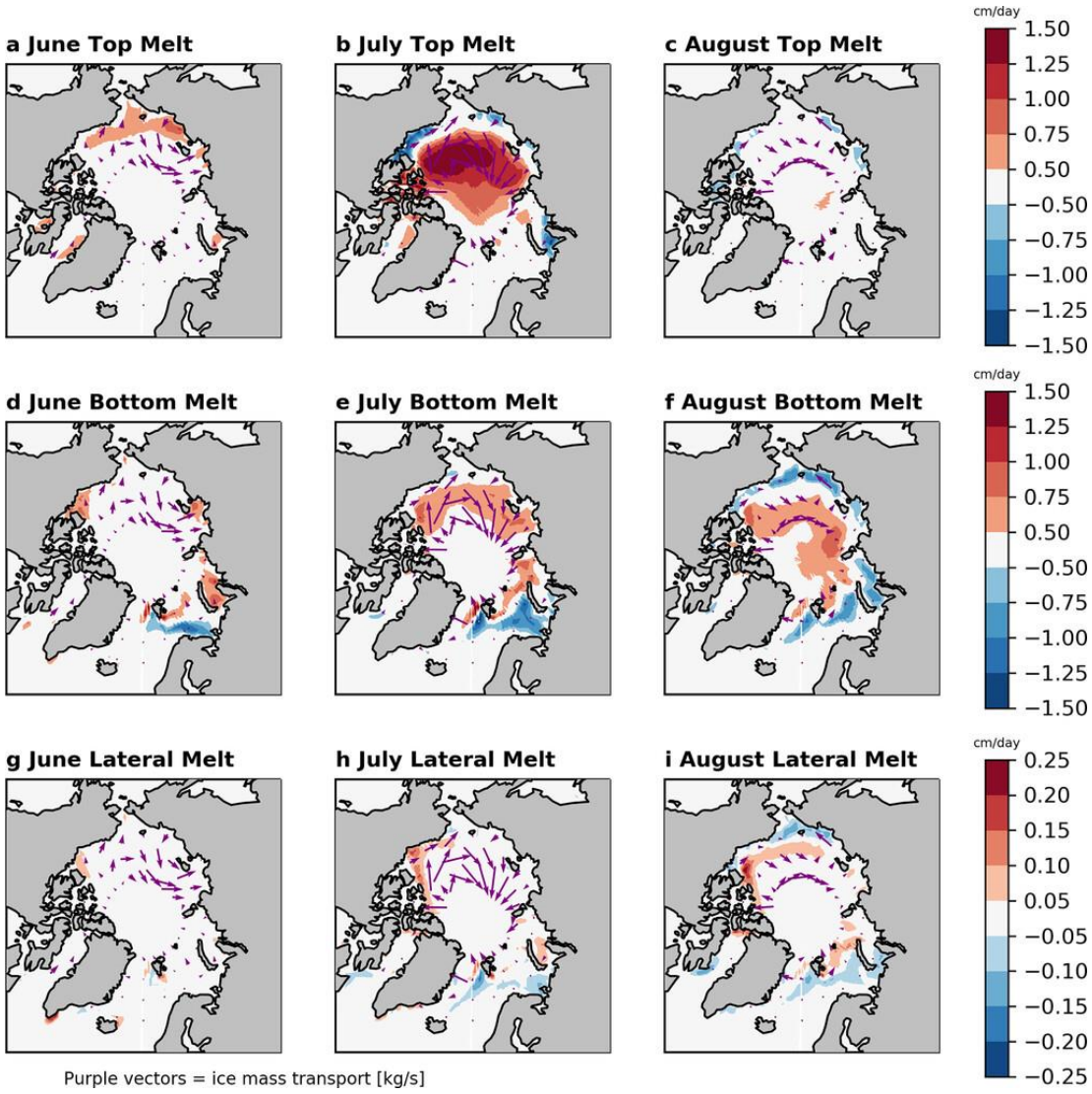

Figure 2.4 dMonthly melting and ice mass transport. Monthly mean (left) June, (center) July, and (right) August (a)–(c) top melt (units: cm day−1), (d)–(f) bottom melt (units: cm day−1), and (g)–(i) lateral melt (units: cm day−1) in the low sea ice minus high sea ice total September SIA years from the perpetual nudging simulations. Purple vectors show 10-yr-mean ice mass transport (units: kg s−1) based on the same composites as melting.

Bottom melting, in contrast to top melting, occurs at a weaker magnitude (up to 1 cm day^{-1}) and in the later stages of the melt season as the ocean takes more time to absorb shortwave radiation and warm (Figs. 2.4d–f) due to its large heat capacity. Shortwave absorption and melting are also enhanced by ice mass transport in the Pacific sector that breaks up the ice pack and exposes open ocean in the Beaufort Sea (purple vectors in Fig. 2.4). Sea ice export into the

Atlantic increases slightly as the sea ice is thinned and primed for movement in response to perpetual wind forcing following a similar pattern as the 10-yr means (Figs. 2.5d–f).

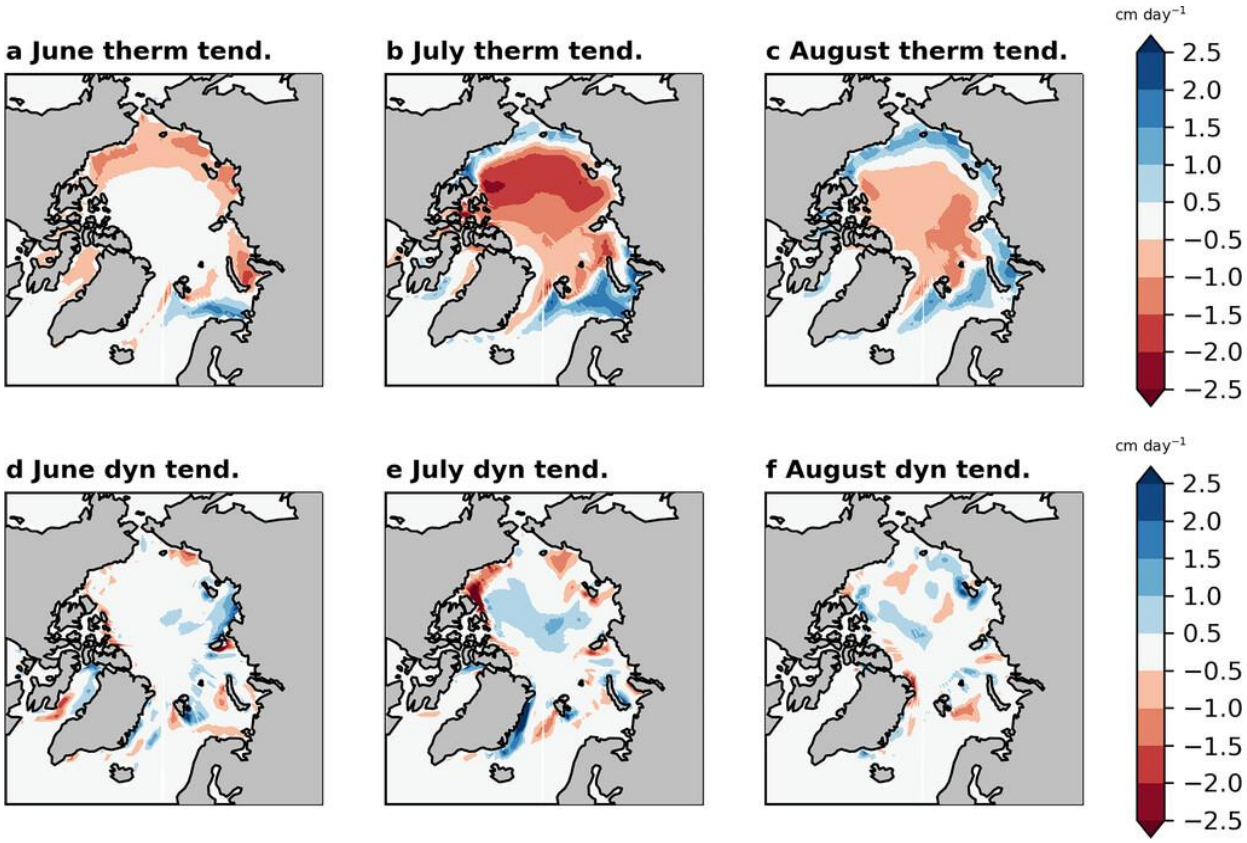

Figure 2.5 Monthly volume changes due to thermodynamics vs dynamics. Monthly mean (left) June, (center) July, and (right) August (a)–(c) thermodynamic sea ice volume tendency (units: cm day−1) and (d)–(f) dynamic sea ice volume tendency (units: cm day−1) in the low sea ice minus high sea ice total September SIA years from the perpetual nudging simulations. Note that the colors are flipped relative to the values in Fig. 2.4 to maintain correspondence between melting and volume/thickness tendency.

Composite analysis of the perpetual nudging simulations highlights a leading role of wind-driven radiative impacts relative to dynamics on Arctic sea ice loss; however, in most studies, the loss of sea ice due to winds is generally examined in the context of these dynamical effects, specifically export of sea ice out of the basin. But by using the partitioning of sea ice volume tendency into thermodynamic and dynamic components we find in low sea ice years there is

weak sea ice export through the Fram Strait during July, and little to none in other months (Fig. 2.5). The strong anticyclonic ice mass transport during July also leads to a convergence of sea ice within the central Arctic and along the eastern coast of Greenland (Fig. 2.5e; Thorndike and Colony 1982). The pattern of the thermodynamic tendency term coincides with that of top melting in June and July, contributing to as much as 2.5 cm day^{-1} of melting, as well as to bottom melting in August (Figs. 2.5a–c). During JJA, thermodynamics contribute to 91% of the total volume change relative to dynamics (Fig. 2.5) with dynamically driven convergence of the ice resulting from anticyclonic circulation producing increasing sea ice volume in the central Arctic. Therefore, the thermodynamic component associated with horizontal temperature advection and shortwave absorption triggered by adiabatic processes should be accounted for as it plays a leading role in wind-driven forcing.

2.4 An optimal sea ice melting mode in a preindustrial run and paleoclimate reanalysis

Results from the nudging simulations suggest that the CESM1 can capture many of the observed changes in September sea ice over the last 40 years once winds are constrained to reanalysis data. Since the 40-yr reanalysis is likely too short to cover all possible internal wind variability and the increased anthropogenic forcing over this period may be imprinted in these wind patterns, we need to search for a similar optimal mode in a longer simulation and reanalysis product containing a broader spectrum of internal climate variability and less influence of anthropogenic forcing. To achieve this goal, we first examine the relationship between local Arctic atmospheric circulation and sea ice in a long preindustrial control simulation without anthropogenic forcing.

We take a pseudo-ensemble approach, dividing the 1800-yr CESM1 preindustrial control simulation into non-overlapping, running 10-yr means and composite based on the five low sea ice periods minus the five high sea ice periods for comparison with the 10-yr nudging experiments (Fig. 2.6a). We also test the sensitivity of our criteria by selecting more members in the extreme groups (e.g., 8, 10, etc.) and find that the composite results show consistent features regardless of group size. We continue focusing on summertime (JJA) since that is the primary season linked with September sea ice.

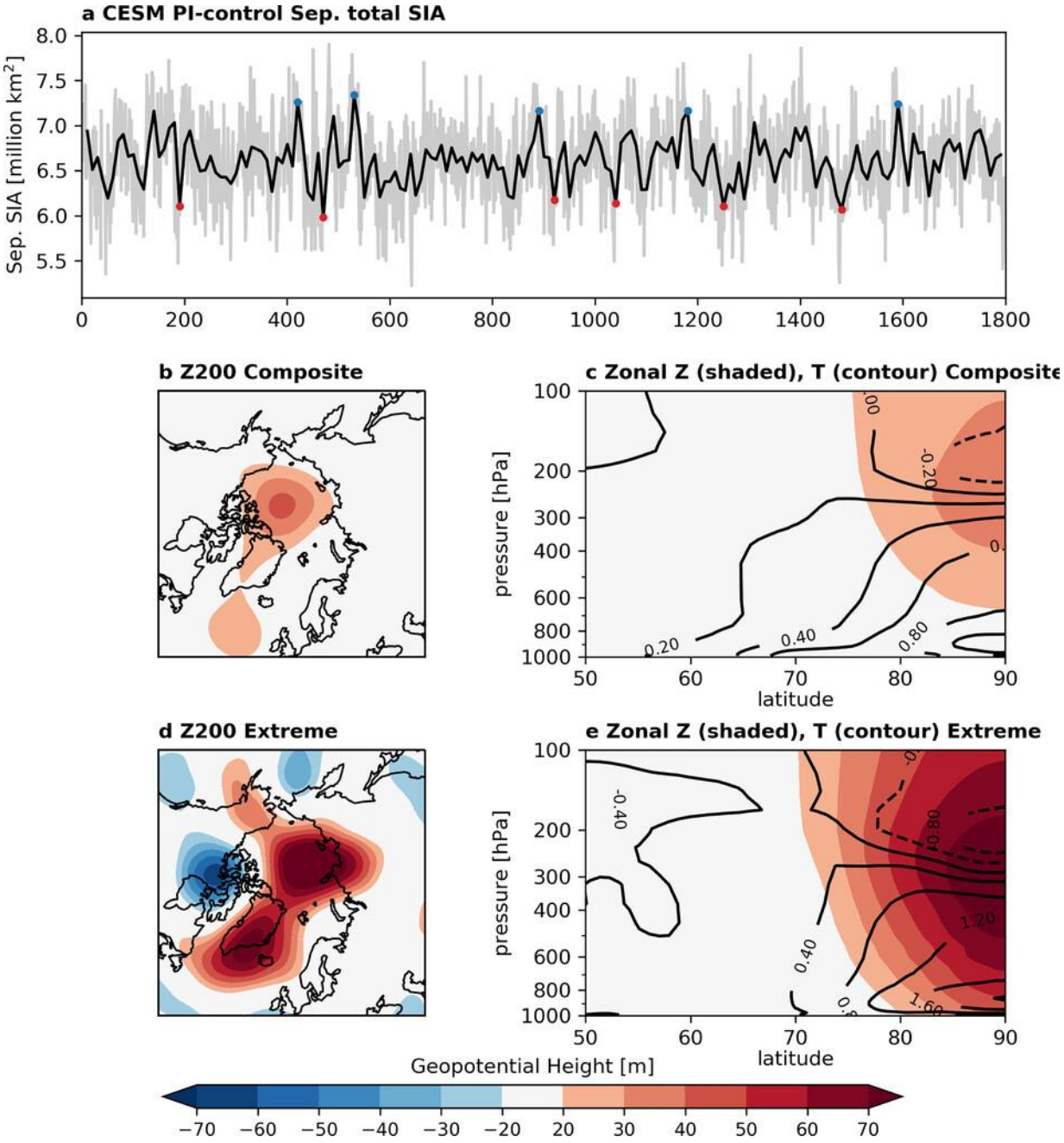

Figure 2.6 Model-based internal variability. (a) Non-overlapping, running 10-yr means of total September SIA (black) and its raw year-to-year variability (gray). Red dots indicate lowest total September SIA years over non-overlapping 10-yr periods and blue dots indicate the highest total September SIA 10-yr periods. (b) JJA 200 hPa geopotential height and (c) zonal mean geopotential height (shading) and temperature (contour) from low minus high total September SIA 10-yr periods from the 1800-yr CESM1 preindustrial control simulation. Extreme or optimal (d) Z200 and (e) zonal mean geopotential height pattern favoring the strongest 10-yr September sea ice melting period in the CESM1 preindustrial control simulation. The extreme melting pattern is multiplied by 2 for comparison with the composites of the low sea ice minus high sea ice years from the perpetual simulations.

The CESM1 preindustrial control simulation is able to capture a similar structure over the Arctic basin to the nudged simulations, showing high pressure over the central Arctic during years of the strongest sea ice decline (Fig. 2.6). This comparison serves as an independent test of the model dynamics, suggesting that the processes linking winds and sea ice seen in the nudging experiments are not an artifact of the nudging method but inherent to the model itself and constrained by reanalysis winds. The preindustrial control simulation shows a high pressure system confined to the Beaufort high region during 10-yr periods of low sea ice cover but has a much weaker magnitude of geopotential height rise compared with the composites from the nudging simulations. Similar magnitudes of sea ice change coinciding with weaker circulation changes may be due to the free running model's ability to sustain very high JJA geopotential height rise over a 10-yr period or coupling between the atmosphere and surface. In the nudging simulations, we force the model to experience this strong 10-yr wind pattern continuously. A period of 10 or more years with sustained wind forcing in the free run would likely need to be sourced either from the local or lower latitude oceans but models have been shown to not accurately capture tropical forcing and may not be able to capture this strong height rise despite a similar circulation–sea ice relationship strength (Topál et al. 2020). However, the local geopotential height changes relative to total SIA change yields similar magnitudes in the 10-yr mean of the perpetual nudging simulations (72 m height rise versus 3.1 million km^2 melt) and preindustrial control simulation (25 m height rise versus 1.1 million km^2 melt). The zonal mean temperatures are also similar to those from the nudging simulations, suggesting that the differences in lower tropospheric temperatures between the nudging simulations and ERA-I are not associated with the nudging but due to a surface-driven or

boundary layer response inherent to the CESM1. Therefore, the model is still determining this sea ice response to wind forcing and the nudging is only providing a realistic forcing.

We also use the same non-overlapping, running 10-yr window to find a single 10-yr period with the largest decline out of the entire integration (Figs. 2.6d,e). The most extreme event shows a very similar structure to the composites and observations, but the magnitude is still half that in observations and the center of high pressure is shifted toward the central Eurasian coast. The "Figure-8" anticyclonic circulation pattern is the optimal mode in the free run, similar to the pattern in ERA-I, suggesting that the observed optimal mode is robust and can exist without CO2 forcing. Furthermore, the CESM1 can capture the relationship between the strongest sea ice melting and high pressure over the Arctic. The shifted high pressure system toward the Eurasian coast and over the ice-free ocean surface, produces a zonal mean temperature profile much more consistent with ERA-I, where there is not a surface-driven warming response at the periphery of the basin.

In addition to the CESM1 preindustrial control simulation, we use the same compositing approach and linear detrending to examine two climate proxy-assimilated reanalysis simulations, EKF400 and PHYDA, as well as a sea ice reconstruction from Brennan and Hakim (2022), to further establish the relationship between atmospheric circulation and sea ice changes over the last 400 years (Fig. 6). We compare EKF400 JJA 500 hPa geopotential heights with the optimal circulation pattern from the perpetual nudging simulations, though it should be noted that EKF400 uses an AMIP-style approach with prescribed sea ice that may lead to errors in surface temperature through the omission of important surface-based feedbacks (Graff et al. 2019). Composites are made using surface temperature because paleo-reanalysis products generally do not include sea ice output due to the rarity of sea ice proxy

records. By using surface temperature from the three products, we aim to give more weight to the assimilated PAGES2k paleo-records and reduce some of the uncertainty from model related biases. In addition, JJA Arctic surface temperature (70°–90°N) in the modern era reanalysis and the nudging experiments strongly correlates with total September SIA ($r = -0.895$ in nudging simulations, Olonscheck et al. 2019, Bonan et al. 2021a). Wang et al. (2021) also used a sea ice model simulation driven by near-surface air temperatures to indicate that September sea ice closely follows changes in 2 m temperature in summer. Thus, we believe that JJA surface temperature variability within the Arctic may reflect changes of sea ice in summer to a certain extent. Composites of surface temperature based on surface temperature from both EKF400 and PHYDA show consistent centers of warming near the Canadian archipelagos and central Eurasia, though the magnitudes in EKF400 are much smaller (Supplementary Fig. A8). EKF400 Z500 composites, despite not including proxy data in or closely around the Arctic, are able to capture a similar JJA high pressure center in Z500 over the Canadian archipelagos and western Greenland that extends into the central Arctic and over the Ural Mountain region in years that have higher surface temperatures (Fig. 2.7). If the observed relationship between sea ice, surface temperature, and atmospheric circulation observed during recent decades holds, these paleo-reanalyses suggest that a similar mode may have contributed to extreme sea ice loss in the last 400 years in the absence of rapidly increasing carbon dioxide concentrations.

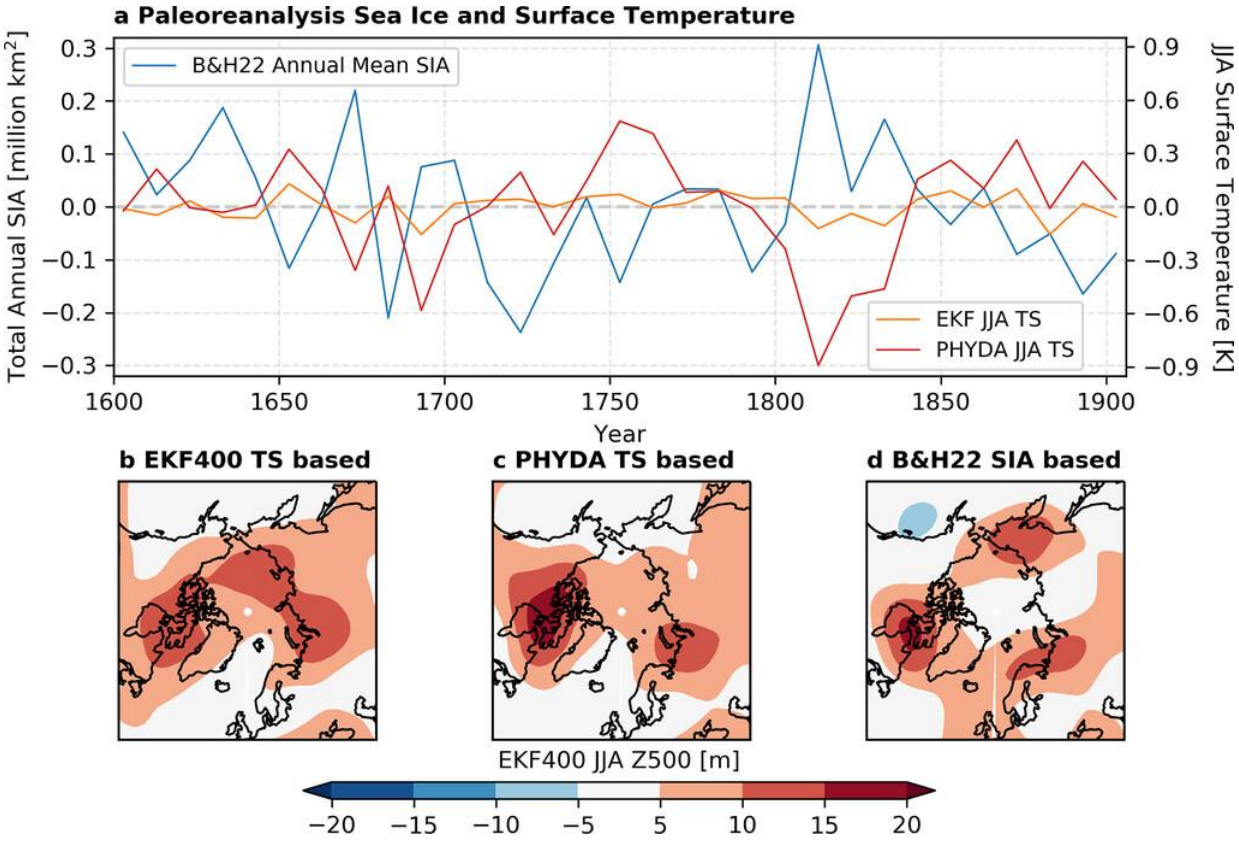

Figure 2.7 Influence of wind forcing on Arctic sea ice in paleoreanalysis. (a) Detrended annual mean total SIA reconstruction from Brennan and Hakim (2022) and Arctic-averaged (70°–90°N) surface temperatures from EKF400 and PHYDA paleoclimate reanalysis. Composites of Z500 (shading) based on the most extreme non-overlapping 10-yr periods from Arctic-averaged (b) EKF400 JJA surface temperature, (c) PHYDA JJA surface temperature, and (d) Brennan and Hakim (2022) annual mean total SIA. In the nudging experiments, JJA Arctic surface temperature (70°–90°N) strongly correlates with total September SIA ($r = -0.895$), indicating that pan-Arctic JJA surface temperature can be used as an approximation of September sea ice variability.

2.5 Discussion

2.5.1 Sensitivity of sea ice to internal circulation forcing

Currently the common practice for quantifying internal variability associated with a model is carried out using a long preindustrial control simulation or large ensembles (Deser et al. 2020). In this approach, internal variability is determined by model physics and coupling among different components of the system. However, models still have deficiencies in their

ability to simulate important relationships between sea ice and the atmosphere, as well as teleconnections between high latitude circulation and remote forcing (Ding et al. 2014, 2017; Rosenblum and Eisenman 2016; Luo et al. 2021). By nudging winds, we can overcome these hurdles to some degree and more effectively evaluate the climate response to atmospheric variability in a manner more representative of observed rather than model-dependent variability. The composites using the preindustrial control simulation, which are representative of the inherent wind forcing pattern most conducive to enhanced sea ice loss, show an ability to capture many of the observed relationships between the Arctic atmosphere and sea ice.

Due to difficulties with model limitations, previous studies have often focused on a qualitative relationship between circulation and sea ice. This information is important but insufficient for us to understand the detailed sensitivity of September sea ice to preceding JJA circulation change. To achieve a better quantification of this sensitivity we calculate the slope of the linear regression between total September SIA and the preceding JJA Z200 within the Arctic (70°–90°N) and use this slope as a measure of the sensitivity (Fig. 8). This slope (km^2 m^{-1}) will tell us the extent a higher Z200 rise in m (indicating a warmer atmosphere below 200 hPa) could induce a certain areal change in summertime sea ice. In both the continuous nudging and preindustrial control simulations, the mean sensitivities (7700 and 6600 km^2 m^{-1}, respectively) are slightly lower than in observations (9000 km^2 m^{-1}), though the observed sensitivity falls within the spread of all three simulations. The continuous nudging simulations, with a nudging strength of 0.5, reduce the spread in sea ice sensitivity to wind forcing in half relative to the preindustrial control simulation. When conditions favoring strong melting or growth are allowed to persist, such as in the perpetual simulations, the response of sea ice to wind forcing saturates at a little over 20,200 km^2 m^{-1}, which is over double that of observations

and 3 times the continuous and preindustrial control simulations. The much higher sensitivity later in the perpetual simulations suggests that if the optimal circulation pattern could last longer in the CESM1, as done in the perpetual nudging simulations, the sea ice becomes more responsive to wind forcing through the ice–albedo feedback. However, this effectiveness of this mechanism will be saturated with the upper bound at 23,500 km^2 m^{-1} after 5–6 years even if the optimal wind pattern could persist continuously.

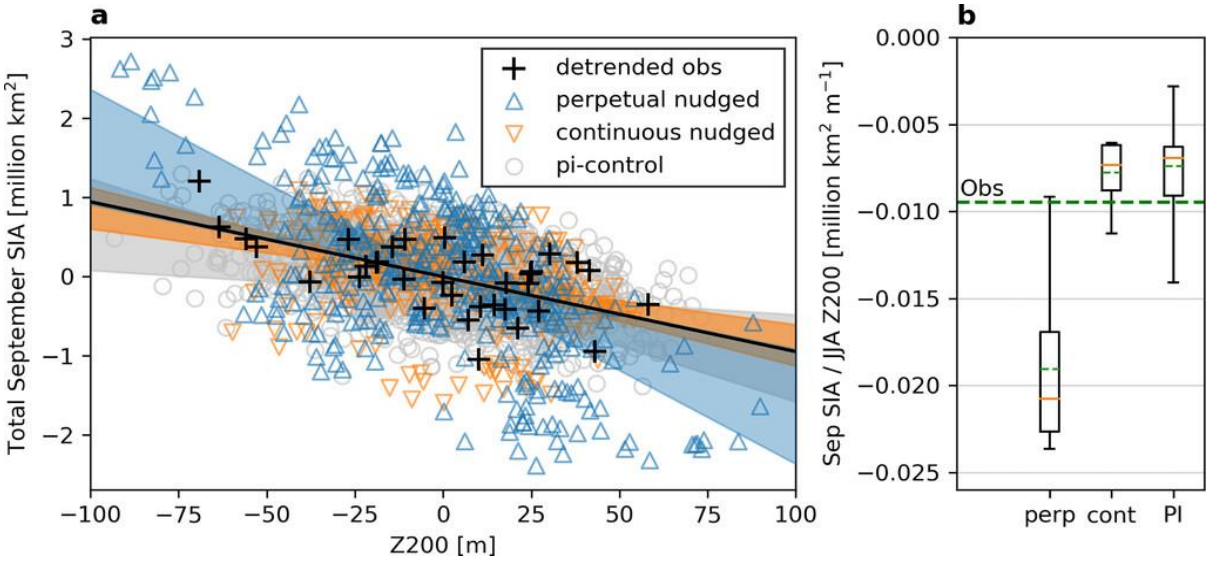

Figure 2.8 Observed and simulated sea ice sensitivity to wind forcing. (a) Relationship between JJA Z200 within the Arctic (70°–90°N) and total September Arctic SIA from the detrended ERA-Interim and NSIDC products (black), all years from the perpetual nudging simulations (blue), continuous nudging simulations (orange), and CESM1 pi-control simulation (gray). Shaded envelopes show the range of SIA regressed onto Z200 from each member or pseudomember in the simulations. (b) Regression slopes of total September SIA onto Z200 in the observations (dashed green line), perpetual simulations, continuous simulations, and pi-control simulation. Dashed green lines in boxes show ensemble mean and orange lines show ensemble medians.

The nudging approach, where wind patterns from each year are repeated, also provides novel insight into the role of wind forcing on the ice–albedo feedback. Surface shortwave absorption leading to polar amplification is generally attributed to the consistent and increasing influence of anthropogenic forcing (Curry et al. 1995). However, it should be considered that

these model simulations show observed wind patterns are similarly capable of modulating the radiative fluxes entering and leaving the Arctic surface and producing an ice–albedo feedback over several years of persistent, favorable atmospheric conditions for melting. This is important because there are sources of interannual-to-decadal variability, such tropical–Arctic teleconnections, that can generate successive years of wind patterns favoring strong melting (Screen and Deser 2018; Meehl et al. 2018; Baxter et al. 2019; Bonan and Blanchard-Wrigglesworth 2020; Topál et al. 2020). Separating this contribution of internal variability from that of anthropogenic forcing is important for quantifying future trends in melting and warming within the Arctic.

2.5.2 Possible caveats associated with the nudging approach

Previously, Huang et al. (2021) found improved agreement relative to satellite-constrained products of cloud changes using the wind nudging approach, as weak air–sea gradients during the melt season generate very little surface influence on cloud changes leaving large-scale circulation as a dominant driver (Kay et al. 2016; Morrison et al. 2019). However, constraining large-scale atmospheric dynamics cannot alleviate all the biases associated with the representation of cloud physics or boundary layer schemes needed to fully understand their role in modulating radiative fluxes and therefore sea ice changes (Huang et al. 2021; Luo et al. 2021). The CESM1, like most Earth system models, has been shown to underestimate supercooled cloud liquid in the Arctic, likely resulting in the small influence of cloud shortwave feedbacks relative to surface albedo in our perpetual simulations (Cesana et al. 2012; Middlemas et al. 2020; McIlhattan et al. 2020).

It is also possible that the arbitrary initialization on 1 January used here introduces inconsistencies, especially when repeated over 21 years, that could impact aspects of preconditioning and seasonal transitions that were not assessed in this study (Stroeve et al. 2014; Smith and Jahn 2019). Composites of the preceding January–May averaged geopotential height and temperature based on the same extreme nudging years from the perpetual simulations (row 1 in Table 2.2) reproduces a very prominent positive NAO pattern and warming over Siberia, referred to as the warm Arctic–cold Eurasia (WACE) pattern (Supplementary Fig. A6, Mori et al. 2014; Labe et al. 2020). A similar pattern can also be seen in composites using the CESM1 preindustrial control simulation (Supplementary Fig. A7), but not in the reanalysis using the extreme detrended years from the NSIDC record (row 2 in Table 2.2). Features of this predominantly wintertime pattern have been linked to the atmospheric response to sea ice loss, but the physical mechanisms explaining the relationship found here are not well understood (Ogi et al. 2003; Nakamura et al. 2015; Banerjee et al. 2021). It remains uncertain whether this discrepancy is introduced by our arbitrary initialization on 1 January and how important this WACE pattern is in driving summer sea ice. These questions are beyond the scope of this study's experimental framework, but this result should garner further attention and modeling studies in the future.

Another caveat of the approach is that the reanalysis fields are regridded to the nominal 1° resolution of the model. Therefore, nudging to higher resolution reanalysis, such as ERA5, may capture finer resolution processes (Smirnova and Golubkin 2017), though improvement may be limited within our current model setup. Finer model resolution may improve the representation of cyclones in the nudging simulations, which may have had an impact during years with strong cyclonic activity late in the melt season, such as 2012 (Simmonds and Rudeva

2012; Yamagami et al. 2017). Improved simulations of Arctic cyclones or small-scale circulations could enhance the dynamical contribution to sea ice loss, in addition to biases associated with the underestimation of sea ice motion (Rampal et al. 2011) or melt pond and thermodynamic parameterization schemes (Keen et al. 2021).

Despite these limitations in the experimental design, the nudging approach used here offers many new opportunities for further evaluating different climate scenarios in global climate models and responses of a wide array of climate processes (e.g., Arctic Ocean temperature, clouds, high latitude land processes, hydrological and biogeochemical cycles) by partially constraining model dynamics and internal variability to observed or idealized cases over targeted regions. This potential is highlighted by the nudging approach's ability to constrain sea ice in the CESM1 by inducing wind patterns well above the surface and reveals how atmospheric forcing can shape Arctic sea ice variability. Additionally, we focus only on better understanding of interannual variability of summertime Arctic sea ice, but the nudging approach shows tremendous promise in addressing many other processes on a broad range of time scales that contribute to lower atmospheric and surface changes in other seasons and regions as well as improving sea ice forecasts and projections. In particular, this methodology can help us constrain sea ice sensitivity to wind forcing and internal variability within models by quantifying the largest melting response to an optimal atmospheric circulation pattern following complete saturation of the ice–albedo feedback (~25,000 km^2 loss of total September SIA per meter increase in JJA Z200) and can help improve predictions of future changes, such as the first occurrence of an ice-free Arctic.

2.6 Conclusions

In this study, we conduct a 40-yr continuous simulation and a set of perpetual simulations using the CESMv1.2.2.1, keeping carbon dioxide concentrations fixed and nudging free tropospheric winds within the Arctic (above 850 hPa, 60°–90°N) to those from ERA-I, then repeating each reanalysis year for up to 21 years. Only by partially nudging Arctic winds toward those from ERA-I in the continuous and perpetual nudging simulations, the model can replicate key features of long-term trends and year-to-year changes in total September SIA over the satellite era, despite a slightly weaker relationship between sea ice and winds in the model (Topál et al. 2020). Furthermore, the perpetual nudging simulations allow for the examination of a quasi-equilibrium response of Arctic climate to wind forcing during years of the strongest sea ice change. Four key conclusions were drawn from the perpetual nudging simulations:

- The optimal atmospheric mode that is associated with melt in all datasets is a summertime "Figure-8" quasi-barotropic anticyclone centered over the Arctic and extending over Greenland.

- The wind impacts on sea ice are primarily thermodynamic, not dynamic, resulting from subsidence-driven warming of the lower troposphere and the surface ice–albedo feedback.

- Sea ice sensitivity to atmospheric circulation change is ~25,000 km^2 loss of total September SIA per meter increase in JJA Z200, taking ~5–6 years to saturate if the same forcing could be perpetually applied.

- Nudging provides a novel method for studying coupled climate model experiments by constraining atmospheric circulation to examine other components of the Earth system.

In all, this novel application of nudging in a fully coupled climate model shows that the most extreme climate scenario that could cause an abrupt significant sea ice melting epoch is a multiple year-long persistence of the summertime high pressure circulation pattern in the Arctic that enhances a prolonged sea ice–albedo feedback. This pattern can dramatically increase the sea ice sensitivity to internal variability and induce significant Arctic warming. The same process with an opposite sign may also cause a strong recovery of sea ice and a temporary Arctic cooling. In the reanalysis, this optimal mode contributing to sea ice retreat does not occur more than two years in a row. Though infrequent, the CESM1 pi-control simulation and EKF400 experience consecutive years of extreme high pressure over the Arctic greater than +1 std for a maximum of 4 (0.4%) and 3 (3.0%) years in any given 40-yr window, respectively. If considering positive anomalous high pressure over the Arctic (>0 m detrended, 70°–90°N), the maximum consecutive occurrence is 6 (2007–12), 10, and 9 years in ERA-I, the CESM1 pi-control simulation, and EKF400, respectively. Prolonged periods with frequent years characterized by prominent Arctic warming and anomalous high pressure, such as 2007–12, may reflect an emergence of this scenario, which appears to be sensitive to remote forcing over the tropical oceans (Baxter et al. 2019), although this relationship is found to be nonstationary over a longer period (Meehl et al. 2018; Bonan and Blanchard-Wrigglesworth 2020). Thus, the main driving force of this type of persistent anticyclonic circulation pattern in the Artic remains as an important source of uncertainty in projecting future sea ice change.

In this study, the nudging approach allows us to control for this uncertainty locally within the Arctic and to directly quantify this relationship using observed atmospheric circulation patterns and may be applied to remote Arctic teleconnections in the future.

2.7 Declarations

2.7.1 Funding

This study was supported by Climate Variability and Predictability (NA18OAR4310424) and Modeling, Analysis, Predictions, and Projections (NA19OAR4310281) programs as part of NOAA's Climate Program Office, and NSF's Polar Programs (OPP-1744598). We acknowledge the CESM Large Ensemble Community Project and supercomputing resources provided by NSF/CISL/Yellowstone (https://doi.org/10.5065/D6RX99HX). We thank the CESM Polar Climate Working Group for discussion and computing support.

2.7.2 Conflicts of interest/Competing interests

The authors declare that they have no conflict of interest.

2.7.3 Data Availability

ERA-I can be accessed at https://www.ecmwf.int/en/forecasts/dataset/ecmwf-reanalysis-interim and ERA5 can be accessed at https://cds.climate.copernicus.eu/cdsapp#!/home. The CESM can be download from https://github.com/ESCOMP/CESM.

References

Banerjee, A., A. H. Butler, L. M. Polvani, A. Robock, I. R. Simpson, and L. Sun, 2021: Robust winter warming over Eurasia under stratospheric sulfate geoengineering—The role of stratospheric dynamics. Atmos. Chem. Phys., 21, 6985–6997, https://doi.org/10.5194/acp-21-6985-2021.

Baxter, I., and Coauthors, 2019: How tropical Pacific surface cooling contributed to accelerated sea ice melt from 2007 to 2012 as ice is thinned by anthropogenic forcing. J. Climate, 32, 8583–8602, https://doi.org/10.1175/JCLI-D-18-0783.1.

Blanchard-Wrigglesworth, E., K. C. Armour, C. M. Bitz, and E. DeWeaver, 2011: Persistence and inherent predictability of Arctic sea ice in a GCM ensemble and observations. J. Climate, 24, 231–250, https://doi.org/10.1175/2010JCLI3775.1.

Blanchard-Wrigglesworth, E., L. A. Roach, A. Donohoe, and Q. Ding, 2021: Impact of winds and Southern Ocean SSTs on Antarctic sea ice trends and variability. J. Climate, 34, 949–965, https://doi.org/10.1175/JCLI-D-20-0386.1.

Boeke, R. C., and P. C. Taylor, 2016: Evaluation of the Arctic surface radiation budget in CMIP5 models. J. Geophys. Res. Atmos., 121, 8525–8548, https://doi.org/10.1002/2016JD025099.

Bonan, D. B., and E. Blanchard-Wrigglesworth, 2020: Nonstationary teleconnection between the Pacific Ocean and Arctic sea ice. Geophys. Res. Lett., 47, e2019GL085666, https://doi.org/10.1029/2019GL085666.

Bonan, D. B., T. Schneider, I. Eisenman, and R. C. J. Wills, 2021a: Constraining the date of a seasonally ice-free Arctic using a simple model. Geophys. Res. Lett., 48, e2021GL094309, https://doi.org/10.1029/2021GL094309.

Bonan, D. B., F. Lehner, and M. M. Holland, 2021b: Partitioning uncertainty in projections of Arctic sea ice. Environ. Res. Lett., 16, 044002, https://doi.org/10.1088/1748-9326/abe0ec.

Brennan, M. K., and G. J. Hakim, 2022: Reconstructing Arctic Sea ice over the common era using data assimilation. J. Climate, 35, 1231–1247, https://doi.org/10.1175/JCLI-D-21-0099.1.

Bushuk, M., M. Winton, D. B. Bonan, E. Blanchard-Wrigglesworth, and T. L. Delworth, 2020: A mechanism for the Arctic sea ice spring predictability barrier. Geophys. Res. Lett., 47, e2020GL088335, https://doi.org/10.1029/2020GL088335.

Cavalieri, D. J., C. L. Parkinson, P. Gloersen, and H. J. Zwally, 1996: Sea ice concentrations from Nimbus-7 SMMR and DMSP SSM/I-SSMIS passive microwave data, version 1 (NSIDC-0051). NASA/National Snow and Ice Data Center Distributed Active Archive Center, accessed 25 November 2020, https://doi.org/10.5067/8GQ8LZQVL0VL.

Cesana, G., J. E. Kay, H. Chepfer, J. M. English, and G. De Boer, 2012: Ubiquitous low-level liquid-containing Arctic clouds: New observations and climate model constraints from CALIPSO-GOCCP. Geophys. Res. Lett., 39, L20804, https://doi.org/10.1029/2012GL053385.

Christensen, M. W., A. Behrangi, T. S. L'ecuyer, N. B. Wood, M. D. Lebsock, and G. L. Stephens, 2016: Arctic observation and reanalysis integrated system: A new data product for validation and climate study. Bull. Amer. Meteor. Soc., 97, 907–916, https://doi.org/10.1175/BAMS-D-14-00273.1.

Curry, J. A., J. L. Schramm, and E. E. Ebert, 1995: Sea ice–albedo climate feedback mechanism. J. Climate, 8, 240–247, https://doi.org/10.1175/1520-0442(1995)008<0240:SIACFM>2.0.CO;2.

Dee, D. P., and Coauthors, 2011: The ERA-Interim reanalysis: Configuration and performance of the data assimilation system. Quart. J. Roy. Meteor. Soc., 137, 553–597, https://doi.org/10.1002/qj.828.

Deser, C., A. Phillips, V. Bourdette, and H. Teng, 2012: Uncertainty in climate change projections: The role of internal variability. Climate Dyn., 38, 527–546, https://doi.org/10.1007/s00382-010-0977-x.

Deser, C., and Coauthors, 2020: Insights from Earth system model initial-condition large ensembles and future prospects. Nat. Climate Change, 10, 277–286, https://doi.org/10.1038/s41558-020-0731-2.

Diebold, F. X., and G. D. Rudebusch, 2021: Probability assessments of an ice-free Arctic: Comparing statistical and climate model projections. J. Econometrics, https://doi.org/10.1016/j.jeconom.2020.12.007, in press.

Ding, Q., and Coauthors, 2017: Influence of high-latitude atmospheric circulation changes on summertime Arctic sea ice. Nat. Climate Change, 7, 289–295, https://doi.org/10.1038/nclimate3241.

Ding, Q., and Coauthors, 2019: Fingerprints of internal drivers of Arctic sea ice loss in observations and model simulations. Nat. Geosci., 12, 28–33, https://doi.org/10.1038/s41561-018-0256-8.

Ding, Q., J. M. Wallace, D. S. Battisti, E. J. Steig, A. J. Gallant, H.-J. Kim, and L. Geng, 2014: Tropical forcing of the recent rapid Arctic warming in northeastern Canada and Greenland. Nature, 509, 209–212, https://doi.org/10.1038/nature13260.

England, M., A. Jahn, and L. Polvani, 2019: Nonuniform contribution of internal variability to recent Arctic sea ice loss. J. Climate, 32, 4039–4053, https://doi.org/10.1175/JCLI-D-18-0864.1.

Fetterer, F., and K. Knowles, 2004: Sea ice index monitors polar ice extent. Eos, Trans. Amer. Geophys. Union, 85, 163–164, https://doi.org/10.1029/2004EO160007.

Franke, J., S. Brönnimann, J. Bhend, and Y. Brugnara, 2017: A monthly global paleo-reanalysis of the atmosphere from 1600 to 2005 for studying past climatic variations. Sci. Data, 4, 170076, https://doi.org/10.1038/sdata.2017.76.

Graff, L. S., and Coauthors, 2019: Arctic amplification under global warming of 1.5° and 2°C in NorESM1-Happi. Earth Syst. Dyn., 10, 569–598, https://doi.org/10.5194/esd-10-569-2019.

Graham, R. M., and Coauthors, 2019: Evaluation of six atmospheric reanalyses over Arctic sea ice from winter to early summer. J. Climate, 32, 4121–4143, https://doi.org/10.1175/JCLI-D-18-0643.1.

Holland, M. M., and J. Stroeve, 2011: Changing seasonal sea ice predictor relationships in a changing Arctic climate. Geophys. Res. Lett., 38, L18501, https://doi.org/10.1029/2011GL049303.

Holland, M. M., L. Landrum, D. Bailey, and S. Vavrus , 2019: Changing seasonal predictability of Arctic summer sea ice area in a warming climate. J. Climate, 32, 4963–4979, https://doi.org/10.1175/JCLI-D-19-0034.1.

Huang, Y., X. Dong, B. Xi, E. K. Dolinar, R. E. Stanfield, and S. Qiu, 2017: Quantifying the uncertainties of reanalyzed Arctic cloud and radiation properties using satellite surface observations. J. Climate, 30, 8007–8029, https://doi.org/10.1175/JCLI-D-16-0722.1.

Huang, Y., Q. Ding, X. Dong, B. Xi and I. Baxter, 2021: Summertime low clouds mediate the impact of the large-scale circulation on Arctic sea ice. Commun. Earth Environ., 2, 38, https://doi.org/10.1038/s43247-021-00114-w.

Hurrell, J. W., and Coauthors, 2013: The Community Earth System Model: A framework for collaborative research. Bull. Amer. Meteor. Soc., 94, 1339–1360, https://doi.org/10.1175/BAMS-D-12-00121.1.

Jahn, A., 2018: Reduced probability of ice-free summers for 1.5°C compared to 2°C warming. Nat. Climate Change, 8, 409–413, https://doi.org/10.1038/s41558-018-0127-8.

Jahn, A., J. Kay, M. Holland, and D. Hall, 2016: How predictable is the timing of a summer ice-free Arctic? Geophys. Res. Lett., 43, 9113–9120, https://doi.org/10.1002/2016GL070067.

Kay, J. E., T. L'Ecuyer, A. Gettelman, G. Stephens, and C. O'Dell, 2008: The contribution of cloud and radiation anomalies to the 2007 Arctic sea ice extent minimum. Geophys. Res. Lett., 35, L08503, https://doi.org/10.1029/2008GL033451.

Kay, J. E., M. M. Holland, and A. Jahn, 2011: Inter-annual to multi-decadal Arctic sea ice extent trends in a warming world. Geophys. Res. Lett., 38, L15708, https://doi.org/10.1029/2011GL048008.

Kay, J. E., and Coauthors, 2015: The Community Earth System Model (CESM) large ensemble project: A community resource for studying climate change in the presence of internal climate variability. Bull. Amer. Meteor. Soc., 96, 1333–1349, https://doi.org/10.1175/BAMS-D-13-00255.1.

Kay, J. E., T. L'Ecuyer, H. Chepfer, N. Loeb, A. Morrison, and G. Cesana, 2016: Recent advances in Arctic cloud and climate research. Curr. Climate Change Rep., 2, 159–169, https://doi.org/10.1007/s40641-016-0051-9.

Keen, A., and Coauthors, 2021: An inter-comparison of the mass budget of the Arctic sea ice in CMIP6 models. Cryosphere, 15, 951–982, https://doi.org/10.5194/tc-15-951-2021.

Labe, Z., G. Magnusdottir, and H. Stern, 2018: Variability of Arctic sea ice thickness using PIOMAS and the CESM large ensemble. J. Climate, 31, 3233–3247, https://doi.org/10.1175/JCLI-D-17-0436.1.

Labe, Z., Y. Peings, and G. Magnusdottir, 2020: Warm Arctic, cold Siberia pattern: Role of full Arctic amplification versus sea ice loss alone. Geophys. Res. Lett., 47, e2020GL088583, https://doi.org/10.1029/2020GL088583.

Lehner, F., F. Joos, C. C. Raible, J. Mignot, A. Born, K. M. Keller, and T. F. Stocker, 2015: Climate and carbon cycle dynamics in a CESM simulation from 850 to 2100 CE. Earth Syst. Dyn., 6, 411–434, https://doi.org/10.5194/esd-6-411-2015.

Li, Z., Q. Ding, M. Steele, and A. Schweiger, 2022: Recent upper Arctic Ocean warming expedited by summertime atmospheric processes. Nat. Commun., 13, 362, https://doi.org/10.1038/s41467-022-28047-8.

Lindsay, R., and J. Zhang, 2005: The thinning of Arctic sea ice, 1988–2003: Have we passed a tipping point? J. Climate, 18, 4879–4894, https://doi.org/10.1175/JCLI3587.1.

Lindsay, R., M. Wensnahan, A. Schweiger, and J. Zhang, 2014: Evaluation of seven different atmospheric reanalysis products in the Arctic. J. Climate, 27, 2588–2606, https://doi.org/10.1175/JCLI-D-13-00014.1.

Liu, J., M. Song, R. Horton, and Y. Hu, 2013: Reducing spread in climate model projections of a September ice-free Arctic. Proc. Natl. Acad. Sci. USA., 110, 12 571–12 576, https://doi.org/10.1073/pnas.1219716110.

Luo, R., Q. Ding, Z. Wu, I. Baxter, M. Bushuk, Y. Huang and X. Dong, 2021: Summertime atmosphere–sea ice coupling in the Arctic simulated by CMIP5/6 models: Importance of

large-scale circulation. Climate Dyn., 56, 1467–1485, https://doi.org/10.1007/s00382-020-05543-5.

McIlhattan, E. A., J. E. Kay, and T. S. L'Ecuyer, 2020: Arctic clouds and precipitation in the Community Earth System Model version 2. J. Geophys. Res. Atmos., 125, e2020JD032521, https://doi.org/10.1029/2020JD032521.

Meehl, G. A., C. T. Chung, J. M. Arblaster, M. M. Holland, and C. M. Bitz, 2018: Tropical decadal variability and the rate of Arctic sea ice decrease. Geophys. Res. Lett., 45, 11 326–11 333, https://doi.org/10.1029/2018GL079989.

Middlemas, E. A., J. E. Kay, B. M. Medeiros, and E. A. Maroon, 2020: Quantifying the influence of cloud radiative feedbacks on Arctic surface warming using cloud locking in an Earth system model. Geophys. Res. Lett., 47, e2020GL089207, https://doi.org/10.1029/2020GL089207.

Mori, M., M. Watanabe, H. Shiogama, J. Inoue, and M. Kimoto, 2014: Robust Arctic sea-ice influence on the frequent Eurasian cold winters in past decades. Nat. Geosci., 7, 869–873, https://doi.org/10.1038/ngeo2277.

Morrison, A., J. E. Kay, W. Frey, H. Chepfer, and R. Guzman, 2019: Cloud response to Arctic sea ice loss and implications for future feedback in the CESM1 climate model. J. Geophys. Res. Atmos., 124, 1003–1020, https://doi.org/10.1029/2018JD029142.

Msadek, R., G. A. Vecchi, M. Winton, and R. Gudgel, 2014: Importance of initial conditions in seasonal predictions of Arctic sea ice extent. Geophys. Res. Lett., 41, 5208–5215, https://doi.org/10.1002/2014GL060799.

Nakamura, T., K. Yamazaki, K. Iwamoto, M. Honda, Y. Miyoshi, Y. Ogawa, and J. Ukita, 2015: A negative phase shift of the winter AO/NAO due to the recent Arctic Sea-ice reduction in late autumn. J. Geophys. Res. Atmos., 120, 3209–3227, https://doi.org/10.1002/2014JD022848.

Export Citation

Notz, D., and J. Marotzke, 2012: Observations reveal external driver for Arctic Sea-ice retreat. Geophys. Res. Lett., 39, L08502, https://doi.org/10.1029/2012GL051094.

Notz, D., and SIMIP Community, 2020: Arctic sea ice in CMIP6. Geophys. Res. Lett., 47, e2019GL086749, https://doi.org/10.1029/2019GL086749.

Ogi, M., Y. Tachibana, and K. Yamazaki, 2003: Impact of the wintertime North Atlantic Oscillation (NAO) on the summertime atmospheric circulation. Geophys. Res. Lett., 30, 1704, https://doi.org/10.1029/2003GL017280.

Olonscheck, D., T. Mauritsen, and D. Notz, 2019: Arctic sea-ice variability is primarily driven by atmospheric temperature fluctuations. Nat. Geosci., 12, 430–434, https://doi.org/10.1038/s41561-019-0363-1.

Otto-Bliesner, B. L., and Coauthors, 2016: Climate variability and change since 850 CE: An ensemble approach with the Community Earth System Model. Bull. Amer. Meteor. Soc., 97, 735–754, https://doi.org/10.1175/BAMS-D-14-00233.1.

Overland, J. E., and M. Wang, 2013: When will the summer Arctic be nearly sea ice free? Geophys. Res. Lett., 40, 2097–2101, https://doi.org/10.1002/grl.50316.

Papritz, L., 2020: Arctic lower-tropospheric warm and cold extremes: Horizontal and vertical transport, diabatic processes, and linkage to synoptic circulation features. J. Climate, 33, 993–1016, https://doi.org/10.1175/JCLI-D-19-0638.1.

Perlwitz, J., M. Hoerling, and R. Dole, 2015: Arctic tropospheric warming: Causes and linkages to lower latitudes. J. Climate, 28, 2154–2167, https://doi.org/10.1175/JCLI-D-14-00095.1.

Polyakov, I. V., and Coauthors, 2020: Weakening of cold halocline layer exposes sea ice to oceanic heat in the eastern Arctic Ocean. J. Climate, 33, 8107–8123, https://doi.org/10.1175/JCLI-D-19-0976.1.

Rampal, P., J. Weiss, C. Dubois, and J.-M. Campin, 2011: IPCC climate models do not capture Arctic sea ice drift acceleration: Consequences in terms of projected sea ice thinning and decline. J. Geophys. Res., 116, C00D07, https://doi.org/10.1029/2011JC007110.

Roach, L. A., and E. Blanchard-Wrigglesworth, 2022: Observed winds crucial for September Arctic Sea ice loss. Geophys. Res. Lett., 49, e2022GL097884, https://doi.org/10.1029/2022GL097884.

Rosenblum, E., and I. Eisenman, 2016: Faster Arctic sea ice retreat in CMIP5 than in CMIP3 due to volcanoes. J. Climate, 29, 9179–9188, https://doi.org/10.1175/JCLI-D-16-0391.1.

Screen, J. A., and C. Deser, 2019: Pacific Ocean variability influences the time of emergence of a seasonally ice-free Arctic Ocean. Geophys. Res. Lett., 46, 2222–2231, https://doi.org/10.1029/2018GL081393.

Shepherd, T. G., 2014: Atmospheric circulation as a source of uncertainty in climate change projections. Nat. Geosci., 7, 703–708, https://doi.org/10.1038/ngeo2253.

Sigmond, M., J. C. Fyfe, and N. C. Swart, 2018: Ice-free Arctic projections under the Paris Agreement. Nat. Climate Change, 8, 404–408, https://doi.org/10.1038/s41558-018-0124-y.

Simmonds, I., and I. Rudeva, 2012: The great Arctic cyclone of August 2012. Geophys. Res. Lett., 39, L23709, https://doi.org/10.1029/2012GL054259.

Smedsrud, L. H., M. H. Halvorsen, J. C. Stroeve, R. Zhang, and K. Kloster, 2017: Fram Strait sea ice export variability and September Arctic sea ice extent over the last 80 years. Cryosphere, 11, 65–79, https://doi.org/10.5194/tc-11-65-2017.

Smirnova, J., and P. Golubkin, 2017: Comparing polar lows in atmospheric reanalyses: Arctic system reanalysis versus ERA-Interim. Mon. Wea. Rev., 145, 2375–2383, https://doi.org/10.1175/MWR-D-16-0333.1.

Smith, A., and A. Jahn, 2019: Definition differences and internal variability affect the simulated Arctic sea ice melt season. Cryosphere, 13, 1–20, https://doi.org/10.5194/tc-13-1-2019.

Sotiropoulou, G., J. Sedlar, R. Forbes, and M. Tjernström, 2016: Summer Arctic clouds in the ECMWF forecast model: An evaluation of cloud parametrization schemes. Quart. J. Roy. Meteor. Soc., 142, 387–400, https://doi.org/10.1002/qj.2658.

Spreen, G., L. de Steur, D. Divine, S. Gerland, E. Hansen, and R. Kwok, 2020: Arctic sea ice volume export through Fram Strait from 1992 to 2014. J. Geophys. Res. Oceans, 125, e2019JC016039, https://doi.org/10.1029/2019JC016039.

Steiger, N. J., J. E. Smerdon, E. R. Cook, and B. I. Cook, 2018: A reconstruction of global hydroclimate and dynamical variables over the Common Era. Sci. Data, 5, 180086, https://doi.org/10.1038/sdata.2018.86.

Stroeve, J. C., M. M. Holland, W. Meier, T. Scambos, and M. Serreze, 2007: Arctic sea ice decline: Faster than forecast. Geophys. Res. Lett., 34, L09501, https://doi.org/10.1029/2007GL029703.

Stroeve, J. C., V. Kattsov, A. Barrett, M. Serreze, T. Pavlova, M. Holland, and W. N. Meier, 2012: Trends in Arctic sea ice extent from CMIP5, CMIP3 and observations. Geophys. Res. Lett., 39, L16502, https://doi.org/10.1029/2012GL052676.

Stroeve, J. C., T. Markus, L. Boisvert, J. Miller, and A. Barrett, 2014: Changes in Arctic melt season and implication for sea ice loss. Geophys. Res. Lett., 41, 1216–1225, https://doi.org/10.1002/2013GL058951.

Swart, N. C., J. C. Fyfe, E. Hawkins, J. E. Kay, and A. Jahn, 2015: Influence of internal variability on Arctic sea-ice trends. Nat. Climate Change, 5, 86–89, https://doi.org/10.1038/nclimate2483.

Tan, I., and T. Storelvmo, 2019: Evidence of strong contributions from mixed-phase clouds to Arctic climate change. Geophys. Res. Lett., 46, 2894–2902, https://doi.org/10.1029/2018GL081871.

Tardif, R., and Coauthors, 2019: Last millennium reanalysis with an expanded proxy database and seasonal proxy modeling. Climate Past, 15, 1251–1273, https://doi.org/10.5194/cp-15-1251-2019.

Taylor, K. E., M. Crucifix, P. Braconnot, C. D. Hewitt, C. Doutriaux, A. J. Broccoli J. F. B. Mitchell, and M. J. Webb, 2007: Estimating shortwave radiative forcing and response in climate models. J. Climate, 20, 2530–2543, https://doi.org/10.1175/JCLI4143.1.

Thorndike, A. S., and R. Colony, 1982: Sea ice motion in response to geostrophic winds. J. Geophys. Res., 87, 5845–5852, https://doi.org/10.1029/JC087iC08p05845.

Tietsche, S., D. Notz, J. H. Jungclaus, and J. Marotzke, 2011: Recovery mechanisms of Arctic summer sea ice. Geophys. Res. Lett., 38, L02707, https://doi.org/10.1029/2010GL045698.

Topál, D., Q. Ding, J. Mitchell, I. Baxter, M. Herein, T. Haszpra, R., Luo, and Q. Li, 2020: An internal atmospheric process determining summertime Arctic sea ice melting in the next three decades: Lessons learned from five large ensembles and multiple CMIP5 climate simulations. J. Climate, 33, 7431–7454, https://doi.org/10.1175/JCLI-D-19-0803.1.

Wang, B., X. Zhou, Q. Ding, and J. Liu, 2021: Increasing confidence in projecting the Arctic ice-free year with emergent constraints. Environ. Res. Lett., 16, 094016, https://doi.org/10.1088/1748-9326/ac0b17.

Wang, C., R. M. Graham, K. Wang, S. Gerland, and M. A. Granskog, 2019: Comparison of ERA5 and ERA-Interim near-surface air temperature, snowfall and precipitation over Arctic sea ice: Effects on sea ice thermodynamics and evolution. Cryosphere, 13, 1661–1679, https://doi.org/10.5194/tc-13-1661-2019.

Wang, W., M. Chen, and A. Kumar, 2013: Seasonal prediction of Arctic sea ice extent from a coupled dynamical forecast system. Mon. Wea. Rev., 141, 1375–1394, https://doi.org/10.1175/MWR-D-12-00057.1.

Wernli, H., and L. Papritz, 2018: Role of polar anticyclones and mid-latitude cyclones for Arctic summertime sea-ice melting. Nat. Geosci., 11, 108–113, https://doi.org/10.1038/s41561-017-0041-0.

Wettstein, J. J., and C. Deser, 2014: Internal variability in projections of twenty-first-century Arctic sea ice loss: Role of the large-scale atmospheric circulation. J. Climate, 27, 527–550, https://doi.org/10.1175/JCLI-D-12-00839.1.

Winton, M., 2011: Do climate models underestimate the sensitivity of Northern Hemisphere sea ice cover? J. Climate, 24, 3924–3934, https://doi.org/10.1175/2011JCLI4146.1.

Yamagami, A., M. Matsueda, and H. L. Tanaka, 2017: Extreme Arctic cyclone in August 2016. Atmos. Sci. Lett., 18, 307–314, https://doi.org/10.1002/asl.757.

Yang, W., G. A. Vecchi, S. Fueglistaler, L. W. Horowitz, D. J. Luet, Á. G. Muñoz, D. Paynter, and S. Underwood, 2019: Climate impacts from large volcanic eruptions in a high-resolution climate model: The importance of forcing structure. Geophys. Res. Lett., 46, 7690–7699, https://doi.org/10.1029/2019GL082367.

Zhang, R., 2015: Mechanisms for low-frequency variability of summer Arctic sea ice extent. Proc. Natl. Acad. Sci. USA, 112, 4570–4575, https://doi.org/10.1073/pnas.1422296112.

Chapter 3

Remote sources of moisture and land capacitor effects driving summertime Arctic water vapor feedback

I.T. Baxter, Q. Ding

In collaboration with: T. Ballinger, H. Wang, M. Holland, H. Wang, Z. Li, Y. Wu, N. Feldl, B. Guan, J. Zhu

Abstract

The primary sources and drivers of recent observed summer Arctic moistening trends are still unclear, which represents a significant research gap hindering attribution and detection analyses of observed Arctic warming. Here, using combined water tagging and circulation nudging techniques, we find that the summertime large-scale circulation trend pattern and land capacitor processes in the Northern Hemisphere play key roles in moistening the Arctic over recent decades. The circulation trend pattern directs more atmospheric rivers (ARs) into the Arctic along three narrow pathways, with the high latitude land surface facilitating more moisture transport through the land capacitor effect. Using a radiative kernel approach, we attribute 83% of the summertime water vapor feedback to remote sources transported from North America and Eurasia. A North American pathway sources moisture from the tropical Atlantic, transported poleward by anticyclones over the subtropics and Greenland, being recycled in central and eastern Canada. In contrast, overlying anticyclonic circulation over Eurasia facilitates moisture evaporation from the soil and transports it to the Arctic, while reducing incoming moisture into the region. Thus, the impacts of large-scale circulation on

ARs and diverse land-atmosphere interactions over high latitudes should be considered to explain the underlying mechanisms of the recent moistening and warming of the Arctic as well as on global scales.

3.1 Introduction

Over the last four decades, the Arctic has warmed at a rate more than 3-4 times than the global mean surface temperature (Manabe and Wetherald 1975; Holland and Bitz 2003; Serreze and Francis 2006; Screen and Simmonds 2010). The warming has led to a rapid decline in Arctic sea ice and Greenland Ice Sheet (GrIS) surface mass balance (SMB) (Stroeve et al. 2012; Topál and Ding 2023). Following the temperature rise, sea ice cover has retreated, which is expected to increase evaporation within the Arctic, leading to greater cloud cover and precipitation (Bintanja and Selten 2014; Kopec et al. 2016; Pithan and Jung 2021; Bonan et al. 2023). Understanding moisture changes in the Arctic is important for constraining water vapor (WV) feedbacks, which are the second strongest contributor to summertime Arctic warming following the sea ice albedo feedback and represent a leading source of model uncertainties in projecting the future climate response in the Arctic (Pithan and Mauritsen 2014; Chung and Feldl 2023).

Under the anthropogenic warming, atmospheric humidity is expected to increase at a rate of 7% per degree warming, as constrained by the Clausius-Clapeyron (CC) relation, leading to increases in downwelling longwave radiation, changes in cloud and precipitation characteristics, and many other alterations to the hydrological cycle (Held and Soden 2006; Trenberth 2011). This constraint has led to a proposed response of the hydrological cycle in the tropics and subtropics to global warming: “the wet gets wetter, and the dry gets drier” due

to the forced response of large-scale circulation, including the Walker circulation, the Hadley cell, and the Ferrel cell (Held and Soden 2006; Trenberth 2011). However, the "wet gets wetter" mechanism has been shown to primarily apply to zonal means and over oceans, but breaks down on regional scales and over land (Byrne and O'Gorman 2015; Wills and Schneider 2016). The Arctic is also unique in this regard because fewer studies have focused on assessing whether the scenario can readily explain the Arctic response to global warming , as it is situated at the far end of the thermally and dynamically driven global circulation. Furthermore, the circulation response at high latitudes usually exhibits very diverse patterns from model to model (Wills and Schneider 2016). In the tropics and mid-latitudes, the moistening scenario across models due to global warming is still thermodynamically determined but modulated by dynamical changes. However, in regions not directly over the tropical oceans, such as over land or in the Arctic, it remains unclear how global warming has shaped the moistening pattern (Simpson et al. 2024).

Despite being relatively dry, the Arctic is expected to become wetter as sea ice retreats, exposing more open ocean and increasing local evaporation and precipitation, as well as resulting from phase changes in cloud moisture roughly following temperature (Box et al. 2019). Additionally, preferential moistening at lower latitudes is expected to strengthen faster than that in the Arctic, resulting in equator-to-pole moist static energy (MSE) gradients that enhance transport towards higher latitudes (Chung and Feldl 2023; Merlis and Henry 2018; Armour et al. 2019; Hahn et al. 2021). However, prior studies have found that the local changes in precipitation associated with decreased sea ice cover and increased evaporation only explain a limited fraction of the simulated changes (Singh et al. 2016, 2017; Harrington et al. 2021). Contributions from remote land and ocean sources play leading roles during different seasons

in these studies but are based on idealized frameworks derived from climate model simulations (Hahn et al. 2021). These theories focusing on the forced response of locally sourced moisture and MSE-gradient-driven moisture transport often do not fully account for land-sea differences and rely on the moisture availability and transport from free-running models (Chapin et al. 2005; Laguë et al. 2023). Differences in the sources of moisture transport are known to have a wide range of impacts on humidity, clouds, and radiation upon entering the Arctic (Harrington et al. 2021). However, it is still unknown how these sources have contributed to observed hydroclimatic changes. These analyses also tend to focus on annual mean changes despite extreme weather features, such as polar lows and atmospheric rivers (ARs), contributing to high-latitude transport variability in different seasons (Wernli and Papritz 2018; Webster et al. 2019; Parker et al. 2022; Fearon et al. 2023).

Moisture transport studies have also focused on impacts to Arctic sea ice, driving melting or preconditioning in colder months, but there has been limited exploration of the relationships between moisture and Arctic surface conditions during summer (Webster et al. 2019; Parker et al. 2022; Yang and Magnusdottir 2017; Huang et al. 2019; Zheng et al. 2021). Therefore, a comprehensive understanding of the origins of moisture sources in the Arctic atmosphere, how moisture is transported into the Arctic in summer, and how such moisture changes contribute to summertime radiative forcing in the Arctic remains elusive. This knowledge gap hinders our ability to assess the models' skill in projecting future moisture, precipitation, and radiation changes and the resultant sea ice variability. Analysis of model simulations has highlighted important questions regarding the ability of models to reproduce observed circulation trend patterns, suggesting that imposing observed winds in the models serves as a plausible approach to estimate how the observed circulation trend patterns drive moisture transport into the Arctic

(Baxter and Ding 2022; Ding et al. 2022). In particular, the recently available water tagging capability in the isotope-enabled Community Earth System Model (iCESM, Brady et al. 2019) and radiative kernels built using ECMWF Reanalysis v5 (ERA5, Hersbach et al. 2020) and atmospheric climate models (Community Atmosphere Model version 5, CAM5) enables us to further trace the sources and sinks of moisture transport and their related radiative impact (Soden et al. 2008; Shell et al. 2008; Held and Shell 2012; Pendergrass et al. 2018; Huang and Huang 2023; Feldl and Merlis 2023). With these new, publicly available tools in iCESM, it has recently become possible to gain an improved understanding of a number of key processes that collectively induce the recent moistening trends and enhanced radiative forcing, including local and remote evaporation, moisture transport into the Arctic, and variations of specific humidity, precipitation, and radiative forcing within the Arctic. In particular, if proven useful to provide a new lens to investigate moisture variations in the Arctic, the method generating global results can also be used to study similar problems for various regions across the globe.

3.2 Data and Methods

3.2.1 Reanalysis

Gridded winds (u,v), temperature, precipitation rate, and specific/relative humidity from the ERA5 atmospheric reanalysis are used to derive year-to-year variability and trends in the Arctic hydrological cycle over the satellite era (1979-2022, Hersbach et al. 2020). ERA5 has been shown to capture precipitation relatively well in the Arctic region compared with other major reanalysis products (Graham et al. 2019; Wang et al. 2019; Barrett et al. 2020). We compute total column-integrated water vapor (TMQ) as vertically integrated total specific

humidity at each grid cell and integrated vapor transport (IVT) to evaluate changes in moisture and transport, respectively:

$$TMQ = -\frac{1}{g}\int_{1000\,hPa}^{300\,hPa} q\,dp$$

$$uIVT = -\frac{1}{g}\int_{1000\,hPa}^{300\,hPa} qu\,dp$$

$$vIVT = -\frac{1}{g}\int_{1000\,hPa}^{300\,hPa} qv\;\,dp$$

In these equations, q is specific humidity, u represents the zonal horizontal wind, v is the meridional horizontal wind, and g is the gravity acceleration. The quantities are computed on standard pressure levels.

Atmospheric rivers (ARs) are detected and tracked using the Guan and Waliser (2019) tARget v3 AR detection and tracking algorithm. It is an updated version of Guan and Waliser (2015), one of the earliest and most widely used AR detection tool. The tARget algorithm has been recommended by the Atmospheric River Tracking Method Intercomparison Project (ARTMIP) as a scheme suitable for both global and regional studies, particularly regions with climatologically low IVT such as at high latitudes (Kay et al. 2016), due to the season- and location-dependent AR thresholds used in this algorithm.

The AR contribution to trends in poleward IVT is quantified by computing the ratio of trends with the IVT fields from ARs removed to those using the full IVT fields. For AR detection, we use daily output from the iCESM1 simulations and 6-hourly outputs from the CESM2-LE and ERA5. The contributions and magnitudes of AR frequency and poleward IVT between ERA5 and iCESM1 are nearly identical, even despite using daily output from iCESM1 for AR detection and tracking. In the CESM2-LE, the strongest moistening members (Arctic total precipitable water > 1 standard deviation), shows strong poleward transport east

of Greenland, over the Bering Strait, and over central Eurasia, but not west of Greenland or over northern Europe (Supplementary Fig. B1b). In these strong moistening members, CESM2-LE also lacks the high-pressure trend over Europe but rather has very strong increasing high pressure over eastern Eurasia (Supplementary Fig. B1b).

3.2.2 Precipitation and Soil Moisture Products

To evaluate the ability of iCESM1 simulations to replicate observed precipitation, we examine high latitude total precipitation trends using a wide range of precipitation products to sample the large uncertainties in a data sparse region (Walsh et al. 2023). Observation-derived precipitation products used include Global Precipitation Climatology Project version 2.3 (GPCP, Huffman et al. 1997), Global Precipitation Climatology Centre (GPCC, Huffman et al. 1997), Climate Prediction Center Merged Analysis of Precipitation (CMAP, Xie and Arkin 1997), the University of Delaware Terrestrial Precipitation product (UDEL-TS, Willmott and Matsuura 1995), and the Integrated Multi-satellitE Retrievals for NASA-JAXA Global Precipitation Measurement (GPM-IMERG). We use the GPCP monthly satellite-gauge product at 1°x1° resolution from 1979 to 2022. CMAP merges measurements from 5 satellite products and rain gauge data averaged to monthly means. UDel-TS interpolates monthly total precipitation from station rain gauge data over land from 1979 to 2014. GPM-IMERG is a NASA product estimating monthly mean global surface precipitation rates at a horizontal resolution of 0.1° from 2000 to the present. Simulated soil moisture trends are compared with trends from SSMV-PASSIVE soil moisture product, which combines measurements from 15 different satellite products from 1981 to 2022.

3.2.3 Models

To evaluate the differences of using the model's inherent circulation and quantify the role of anthropogenic forcing (which we do not directly quantify in the nudged iCESM1 simulations), we examine a suite of available output from CESM1 and CESM2 simulations. We use CESM1-GOGA as a comparison with the fully-coupled and AMIP-style tagging simulations to verify that there are small differences between the iCESM1 configurations (Supplementary Fig. B8). To quantify the contribution from the forced response to anthropogenic climate change and the spread due to internal variability, we examine JJA AR frequency, IVT, and 200 hPa geopotential height trends in 40-members from the CESM2-LE with smoothed biomass burning. Although CESM2-LE provides a total of 100 members for public use, only the 40 members (with smoothed biomass burning) out of the entire 100 ensemble members provides 6-hour data that can be used to identify ARs.

3.2.4 Nudged, water isotope enabled CESM1 simulations

We use the isotope-enabled Community Earth System Model version 1 (iCESM1). iCESM1 uses as its base the CESM1.2 (Kay et al. 2015), which has the Community Atmosphere Model version 5.3 (CAM5.3, Neale et al.), Community Land Model version 4 (CLM4, Oleson et al. 2010), Parallel Ocean Program version 2 (POP2, Smith et al.), and Los Alamos Sea Ice Model version 4 (CICE4, Hunke 2010). The atmosphere and land components have the nominal 1° (0.9° x 1.5° finite volume grid) and 2° (1.9° x 2.5° finite volume grid) resolution and finite-volume dynamical core (CESM1-FV2). Previously, iCESM1 has only been run with the nominal 2° resolution grid and, therefore, we examine both to gauge the

impacts of horizontal resolution on moisture transport and precipitation. In the future, higher resolutions with regional-refinement or global cloud resolving models would be more ideal to address issues of resolution. CAM5.3 has 30 active atmospheric levels in hybrid-sigma coordinates. POP2 and CICE4 are on the nominal 1° resolution grid with displaced poles over Greenland and Antarctica. These experiments are run with prescribed monthly sea surface temperatures and sea ice concentrations taken from ERA5 that are remapped to the iCESM1 ocean model grid. Tagged WV and specific humidity reflects the grid point or region from which it evaporates.

3.2.5 iCESM1 Experiment Design

The isotope-enable Community Earth System Model (iCESM1) uses numerical water tracers to follow movement and phase changes beginning from evaporation, when moisture is tagged based on its region, to when it is precipitated out of the atmosphere (Brady et al. 2019; Nusbaumer et al. 2017). The model is nudged to ERA5 horizontal winds (u, v) and temperature throughout the atmosphere, and specific humidity in the lowest model level nearest the surface. A number of sensitivity experiments are conducted, and the nudging simulation does not appear to be sensitive to whether observed specific humidity is constrained at the lowest model level (not shown). Sea surface temperatures and sea ice concentration from ERA5 are prescribed. Greenhouse gas concentrations are fixed at year-2000 levels, so as not to double count the effects from greenhouse gas driven warming and thereby introduce artificial heating. Previous moisture tagging experiments have employed free-running iCESM1 simulations, but the combination of nudging and tagging in this manner allows us to replay observed atmospheric conditions (derived from ERA5) in iCESM1 so that the hydrological cycle (i.e.,

evaporation, transport, and precipitation) can be decomposed into its observed sources and pathways.

We construct 54 evenly dispersed regions (in terms of latitude and longitude, rather than area) around the globe without consideration for land or ocean surfaces. We also use an additional water tagging simulation, with 2 individual regions over North America and Eurasia land masses, to verify that the majority of moisture being sourced from 50-70° N originates from the land rather than ocean (not shown). To ensure that these runs correctly simulate the climatological patterns of humidity and rainfall, we check the annual cycles in the iCESM1 simulations against reanalysis, finding that the two products agree and the results from the iCESM1 simulations are representative of the changes over the satellite era (Fig. 3.1a-b). In Appendix B we also include an additional 9-region tagging simulation, with the 9 smaller domains within central and eastern Canada (region 47 in the 54-region simulation) to show the moisture sources within this key area.

Since the 54 tagging regions are evenly distributed based on latitude and longitude, larger source region areas closer to the equator may disproportionately contribute to Arctic WV changes. Therefore, we normalize specific humidity from each region by its total area, giving greater weighting to the smaller, high latitude regions. This shifts relative contributions to regions that are closer to or within our target region in the Arctic but does not change the overall qualitative results. In the text we present both raw and normalized contributions.

In addition, we use both atmosphere and land only or atmospheric model intercomparison project-style (AMIP) and fully-coupled approaches. Prescribing sea surface temperatures and sea ice concentrations may not accurately reflect important atmosphere-ocean-sea ice coupling processes that contribute to evaporation or stability of the lower Arctic troposphere. In this

study, we focus on boreal summer, finding that the conclusions are not sensitive to ocean-atmosphere coupling due to weak air-sea gradients within the Arctic. The differences between the AMIP-style and fully-coupled simulations generate canceling effects when averaging over the Arctic as in Fig. 4 and do not change the pattern of WV radiative effect (Supplementary Fig. B9). Future examination of the interactions between the atmosphere and ocean during other seasons is necessary, though this is outside the scope of the present study.

3.2.6 Radiative feedback analysis

To better understand how increasing Arctic moisture contributes to a change in radiative forcing, we follow the traditional radiative kernel approach using the ERA5 and CAM5 surface, all-sky surface radiative kernels from Huang and Huang (2023) and Pendergrass et al. (2018), respectively. iCESM1 outputs are regridded to the same resolution (2.5°x2.5°) and 37 vertical levels as the ERA5 and CAM5 kernels[41]. The moisture kernel quantifies the radiative response to the moistening caused by 1 K warming, assuming constant relative humidity. The WV radiative effect is integrated through the tropospheric column (below ~300 hPa), and we use the local feedback, which considers the surface temperature response at each latitude or an area-weighted average over the Arctic region (70-90° N). The contribution of each moisture source region to the Arctic WV radiative effect is computed by subtracting the WV tagged from each region individually from the total WV at each level and grid point then computing

the radiative effect. All analyses focus on monthly mean or June-July-August (JJA) means to examine the summertime Arctic WV feedback and its associated moisture transport.

Following Huang and Huang (2023), the traditional water vapor feedback (Soden et al. 2008; Shell et al. 2008) associated with total and regional humidity change is computed as:

$$dR_i = K_q dT_i$$

Where,

$$dT_i = \frac{dq_i}{q_0}\frac{R_v}{L_v}{T_0}^2$$

Here, the subscript i denotes each tagged region (1-54), dq_i is the trend in total specific humidity minus the trend in specific humidity from each tagged region, q_0 and T_0 are baseline or climatological specific humidity and temperature based on the 1981-1999 reference period, R_v is the gas constant for water vapor (J), and L_v is the latent heat of vaporization for liquid water at 0° C for water vapor (J kg^{-1}). The local feedback is then computed by dividing by the trend in surface temperature (T_s) at each latitude (ϕ):

$$\lambda_{qi} = dR_i/\Delta T_s(\phi)$$

Note that after computing the local feedback, the sum of the individual regions (1.70 W m^{-2} K^{-1}) is not equal to the total feedback parameter (1.83 W m^{-2} K^{-1}) (Feldl and Merlis 2023). The vertically integrated feedback parameter is computed from 1000 hPa to the tropopause, estimated as 100 hPa in the tropics then linearly decreasing to 300 hPa in the polar regions.

We also provide additional radiative feedback calculations to place our traditional fixed relative humidity kernel approach into a broader context of the established feedback framework. Following the relative humidity framework detailed in Held and Shell (2012), we first compute the traditional total water vapor (LW+SW), Planck, and lapse rate feedbacks, using trends in specific humidity and temperature from the iCESM1 simulations convolved

with the ERA5 radiative kernels (Supplementary Fig. B10). We then compute the alternative Planck, lapse rate, and relative humidity feedbacks (Supplementary Fig. B10). Note that if comparing the feedback magnitudes from our nudged simulations, a La Nina-like trend in the eastern tropical Pacific generates negative water vapor and temperature feedbacks in the tropics that would likely not be seen in the traditional approach that differences pre-industrial control and abrupt doubling or quadrupling CO_2 simulations.

During JJA, the surface longwave water vapor radiative feedback (2.92 W m^{-2} K^{-1}) is dominated by the response to departures from fixed relative humidity (1.79 W m^{-2} K^{-1}), with the required adjustment to maintain fixed relative humidity in response to uniform (alternative Planck minus Planck, 1.09 W m^{-2} K^{-1}) and nonuniform warming (alternative lapse rate minus lapse rate, 0.03 W m^{-2} K^{-1}) being second order (Supplementary Fig. B10). In contrast, the opposite conclusions can be drawn using TOA radiative kernels due to the dominance of the Planck TOA radiative response (Supplementary Fig. B10). The results do not change the relative radiative impacts of the moisture transport from each tagged region, however this suggests that future studies should more thoroughly consider the impacts of relative humidity trends in Arctic climate change. Additionally, future examination of other seasons as well as cloud radiative effects and their interactions with these feedbacks would also be beneficial.

We also test the radiative impacts of moisture transport on the Arctic surface using radiative kernels derived from both ERA5 and CAM5 (Supplementary Fig. B3,B8). Examining the zonal mean patterns of the summertime WV radiative effect, we find good agreement when using either ERA5 or CAM5 surface radiative kernels. Both show a negative feedback in the tropics due to cooling SSTs in the eastern equatorial Pacific and a strong positive feedback in the subtropical midlatitudes. The primary differences in the patterns occur within the central

Arctic. Specifically, the radiative kernels computed using a single-year simulation with CAM5 show a much stronger positive magnitude from 850 to 600 hPa, north of 75°N (Supplementary Fig. B3, B8). In contrast, the ERA5 kernels use the average of 5 years (2011-2015), that provides a relatively broad sampling of the variability in the Arctic, with 2011-2012 and 2015 being dominated by strong anticyclones and 2013-2014 being dominated by strong cyclonic patterns. Anticyclonic circulation over the Arctic, similar to the trends examined in this study, are known to induce cloud increases along the periphery of the anticyclone and in the lowest model layers, but decreases in the mid-troposphere where there is strong subsidence in ERA5. The cloud component generates a cooling effect during boreal summer that dampens the net warming in the all-sky WV radiative effect (Supplementary Fig. B8). Therefore, the differences between ERA5 and CAM5 are likely the result of a combination of internal variability driven atmospheric processes (e.g., subsidence over the central Arctic) and model physics. Ultimately, we find small differences between the two products, and therefore focus on results using the ERA5 kernels.

3.3 Historical and model simulated trends

The iCESM1 simulations with atmospheric nudging yield nearly identical replays of anomalous JJA atmospheric WV within the Arctic from ERA5 (Fig. 3.1a, black and magenta lines), with moistening trends of 0.35 kg m^{-2} $decade^{-1}$ in iCESM1 and 0.27 kg m^{-2} $decade^{-1}$ in ERA5. The 40-member ensemble mean from the Community Earth System Model version 2 Large Ensemble (CESM2-LE) with smoothed biomass burning exhibits a slightly enhanced trend over 1981-2022 (0.53 kg m^{-2} $decade^{-1}$) relative to iCESM1, though the nudged simulations largely fall within the envelope from CESM2-LE members (Fig. 3.1a). While there

is an increasing trend over the satellite era in both atmospheric WV and precipitation, total precipitation in the CESM2-LE, iCESM1, and ERA5 do not increase as strongly as observations from the Global Precipitation Climatology Project (GPCP, green curve in Fig. 3.1b, Huffman et al. 1997). Unlike GPCP, other observational products, such as CPC Merged Analysis of Precipitation (CMAP, Xie and Arkin 1997), Global Precipitation Climatology Centre (GPCC, Schneider et al. 2014), and the University of Delaware Terrestrial Precipitation product (UDel-TS, Willmott and Matsuura 1995), do not show a rapid increase in Arctic precipitation around 2000 and have insignificant trends consistent with iCESM1 and ERA5 (Fig. 3.1b). Detrended total precipitation over the Arctic in nudged iCESM1 strongly correlates with detrended observational precipitation products from 1981-2022: CMAP (r=0.79), GPCP (r=0.59), GPCC (r=0.58), and UDel-TS (r=0.44, 1981-2014). The Integrated Multi-satellitE Retrievals for NASA-JAXA Global Precipitation Measurement (GPM-IMERG, dashed brown curve in Fig. 3.1b) shows a similar peak in Arctic precipitation during the early 2010s but rapidly decreases thereafter, and the product is not significantly correlated with any of the other products examined. Despite the large spread in the magnitude of JJA Arctic precipitation amongst our model simulations and observation-derived datasets, the iCESM1 simulations generally agree well with the observed year-to-year variability and trends of most products examined here. The large uncertainty of current precipitation data in reflecting long-term variability of Arctic precipitation indicates the necessity of the current modeling analysis to aide in better assessment of hydrological variability in high latitudes from a new perspective.

During boreal summer there is significant moistening throughout most of the Northern Hemisphere below 400 hPa (Fig. 3.1d,f). The Arctic experiences moistening of the atmospheric column (0.35 kg m^{-2} $decade^{-1}$, black curve in Fig. 3.1a), except for a small patch

over the Beaufort Sea and parts of the Pacific sector (Fig. 3.1c,e). Moistening trends follow circulation, occurring where there are increases in geopotential height and poleward integrated water vapor transport (IVT). There has been an increasing geopotential height trend extending from the North Atlantic, over Greenland, and into the Arctic that has transported WV poleward to the west of Greenland (16.8 m decade^{-1}). Poleward WV transport has also occurred between a low-pressure center over the Northeast Atlantic and high-pressure center over Europe, as well as east of a low-pressure center over central Eurasia. Zonal mean trends show an increase in specific humidity focused ~800 hPa and throughout the entire Northern Hemisphere (Fig. 3.1d,f). The only non-significant specific humidity trends occur near the surface in the tropics and Arctic and at upper tropospheric levels (Fig. 3.1d,f). Geopotential height trends show the strongest increases in the uppermost troposphere that extend downward closer to the pole (contours in Fig. 3.1d,f). Nudged iCESM1 simulations accurately simulate the long-term variability in humidity and precipitation within the Arctic when atmospheric fields and boundary forcing derived from reanalysis are imposed. This lends more confidence to the ability of the simulated water tagging results in the iCESM1 to reflect observed moisture trends, which will be extensively discussed in the following sections.

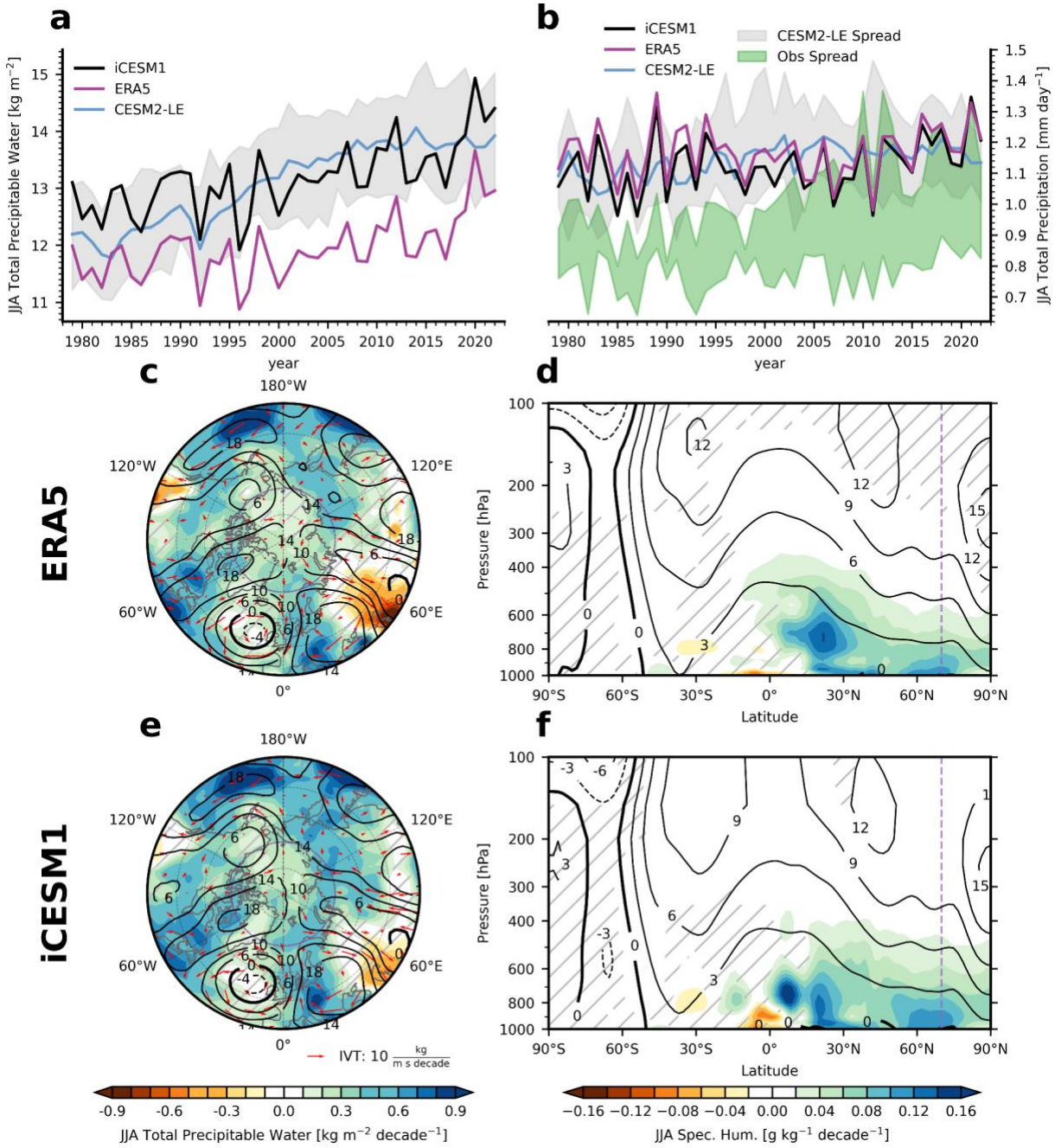

Figure 3.1 Variability and trends in moisture transport from nudged iCESM1 simulations and observation-based datasets. a,b, JJA total column precipitable water (i.e., vertically integrated specific humidity) (kg m^{-2}) within the Arctic (70-90° N) from CESM2-LE (blue, grey shading), iCESM1 (black) and ERA5 (magenta) (**a**). JJA total precipitation (snow+rain, large-scale+convective) within the Arctic (70-90°N) from the spread across observation-based precipitation products (green shading), iCESM1 (black), ERA5 (magenta), and the CESM2-LE (blue, grey shading) (**b**). **c,e**, 1981-2022 linear trends in total precipitable water (shading, kg m^{-2} decade^{-1}), 200 hPa geopotential height (contour, m decade^{-1}), and IVT (blue vectors, kg m^{-1} s^{-1} decade^{-1}) from ERA5 (**c**) and iCESM1 (**e**). **d,f,** 1979-2022 linear trends

in zonal mean specific humidity (shading, g kg^{-1} $decade^{-1}$) and geopotential height (contour, m $decade^{-1}$) from ERA5 (**d**) and iCESM1 (**f**). Gray stippling in panels (**c-f**) indicates insignificant trends (<95% confidence level) in total precipitable water or zonal mean specific humidity.

3.4 Role of ARs in increasing Arctic moisture trend

By definition, trends in JJA AR frequency show similar spatial patterns as the IVT trends (Fig. 2b). There are four primary pathways that transport large amounts of moisture into the Arctic: 1) Siberian, and 2) central Eurasian, 3) European, and 4.) western Greenland pathways. Each coincides with areas that have poleward trends in IVT driven by large-scale circulation (magenta polygons in Fig. 3.2b). These major pathways reside on the western flanks of anticyclonic circulation trends where poleward winds carry large amounts of moisture into the Arctic (Fig. 3.2b).

The simulated Arctic moistening results in large part from an increase in AR driven transport. The JJA total precipitable water trends in the Arctic associated with ARs is 2.56 g m^{-2} $decade^{-1}$ or 77.4% of the total trend (See Methods). Using JJA troposphere mean specific humidity or poleward zonally integrated IVT at 70° N yields contributions of 0.047 g kg^{-1} $decade^{-1}$ (80.0%) and 9.22 million kg m^{-1} s^{-1} (66.8%), respectively. Contributions to poleward IVT along 70° N over western Greenland, northern Europe, and central Eurasia is 3.16 million kg m^{-1} s^{-1} $decade^{-1}$ (65.2%), 0.67 million kg m^{-1} s^{-1} $decade^{-1}$ (73.0%), and 3.08 million kg m^{-1} s^{-1} $decade^{-1}$ (95.5%), respectively (magenta boxes in Fig. 3.2).

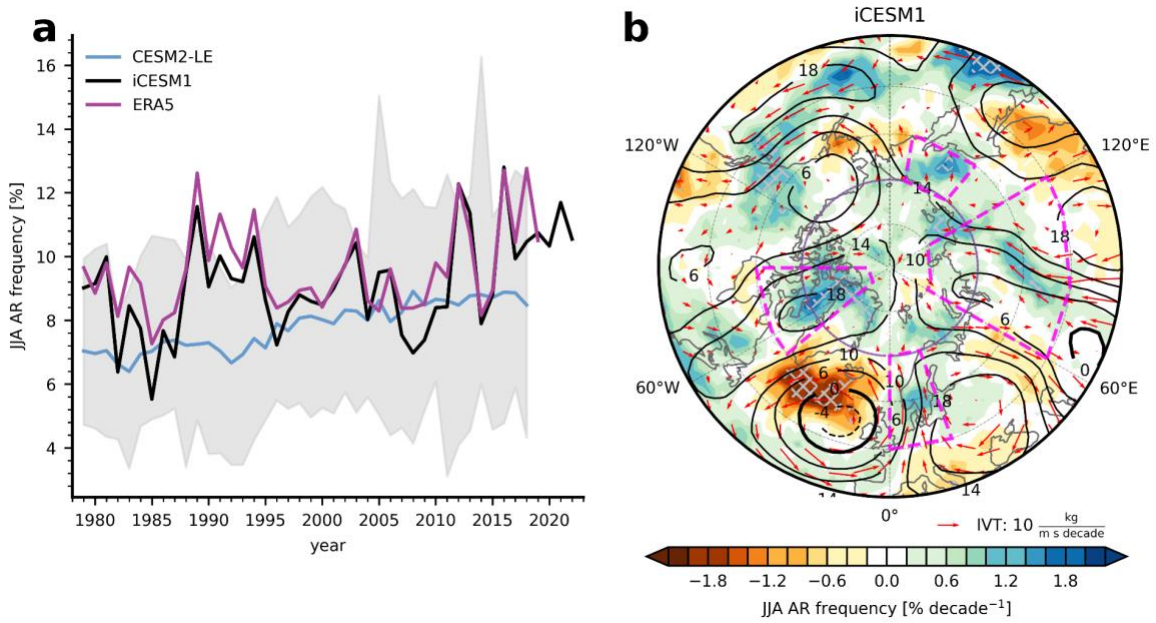

Figure 3.2 Atmospheric Rivers drive moisture transport into the Arctic. a, Area-weighted average of JJA atmospheric river (AR) frequency within the Arctic (70-90°N) from 2 members of the CESM2-LE with 40-yr trends greater than 1.5 standard deviations (dashed blue), CESM2-LE (ensemble mean: solid blue, gray shading), iCESM1 (black), and ERA5 (magenta). **b-d,** Linear trends in JJA AR frequency (shading, % decade^{-1}), 200 hPa geopotential height (black contours, m decade^{-1}), and integrated vapor transport (purple vectors, kg m^{-1} s^{-1} decade^{-1}) from 1981-2022 from iCESM1 (**b**). Gray hatching in panel (**b**) indicates statistically significant AR frequency trends at the 95% confidence level. Dashed purple boxes indicate primary moisture transport pathways into the Arctic.

Previous Arctic water tagging studies have noted the importance of central Eurasian moisture transport, but none have mentioned the importance of transport from North America (Singh et al. 2016, 2017; Harrington et al. 2021). Therefore, to determine if this discrepancy is due to internal variability or the implementation of nudging to reanalysis winds, we examine trends in JJA AR frequency using a 40-member subset of the "free-running" CESM2-LE (see methods). The CESM2-LE shows a comparable frequency of JJA AR events within the Arctic to iCESM1 and ERA5 (Fig. 3.2a); however, the historical model simulation (without nudging) possibly lacks the decadal variability that contributes to the trend in the reanalysis. In the forced response, represented by the CESM2-LE ensemble mean, trends in AR frequency show a relatively uniform increase in AR occurrence across most of the Northern Hemisphere

(Supplementary Fig. B1c). This is consistent with previous research showing GCMs exhibit uniform moistening throughout the entire troposphere in response to greenhouse gas forcing (Simpson et al. 2024).

Focusing on the missing transport from North America in free-running simulations, we find the CESM2-LE only captures the increasing AR frequency trends west of Greenland in two out of the 40 members analyzed in this study (magenta polygon in Supplementary Fig. B1d, 60-85° N, 90-50° W). In these members, the model replicates a slightly southeastward shifted wave train (with a high pressure center over Greenland) that contributes to increased AR frequency west of Greenland (black contours in Supplementary Fig. B1d). However, the free-running model lacks decreasing AR frequency trends in the North Atlantic and, therefore, does not reflect the observed redirection of ARs west of Greenland, but rather an increase coming from the west (Supplementary Fig. B1d). The IVT trends (red vectors in Fig. 3.2b vs. Supplementary Fig B1d) indicate strong zonally oriented transport from the North Pacific into the Arctic that is not observed in iCESM1 and ERA5. Rather, the nudged simulations display a redirection of North Atlantic moisture and ARs west of Greenland that has been linked to cyclonic wave breaking events that generate anticyclonic winds over Greenland (Liu and Barnes 2015) (Fig. 3.2b). It is likely that even when the CESM2-LE captures similar patterns in AR frequency and large-scale circulation, the moisture sources are different than in the nudged iCESM1 and ERA5. This highlights the need to consider the role of observed circulation variability on long-term changes in high latitude ARs.

3.5 Significance of land-sourced moisture for the Arctic summertime WV radiative effect

By nudging to ERA5 winds, the model reveals that the four major vapor transport pathways are responsible for climatological poleward moisture transport and the recent Arctic moistening in summer (Fig. 3.1a-b). We determine the contribution to Arctic moisture changes from each tagged region by computing an Arctic mean (area weighted within 70-90° N) of total precipitable water evaporated from individual regions (see methods, contribution from each tagged region is also normalized by the area of each tagged region).

To understand the contribution of each source region, we focus on the source contributions to both mean and trends in JJA Arctic averaged (70-90° N) total precipitable water. Consistent with previous water tagging studies, we find a leading contribution to the detrended mean being sourced from a narrow band between 50-70° N (7.50 g m^{-2}, 46.6%) and in the long-term trends (1981-2022, 1.63 g m^{-2} $decade^{-1}$, 41% when normalized by area) (Fig. 3.3). This 50-70° N band includes a large contribution from the North American land mass, contributing 7.67% (7.40% normalized) to the mean and 0.329 g m^{-2} $decade^{-1}$ or 16.1% (9.73% normalized) to the 1981-2022 trends (Fig. 3). This strong influence of North America has not been identified in previous free-running or historical simulations examining poleward moisture transport.

The 44-yr trends in source-region contributions to Arctic WV show some similar relationships as their mean contribution, with the strongest contributions coming from Northern Hemisphere land masses, particularly northern Europe, central Eurasia, and northeastern North America (Fig. 3.3b). Remote sources account for 84.2% (62% of total from land) of the moistening trend over the Arctic in the last 4 decades. These trends show less emphasis on Siberia and Alaska, as well as a decreased importance of the midlatitude oceans,

especially northern extensions of these regions. Locally, there is a strong normalized increase in moisture coming from the Kara Sea and Canadian Arctic Archipelago regions. When considering the colder seasons, as temperature gradients can reach up to 40° C between the atmosphere and ocean, there is a greater contribution from the local (Barents Sea and Kara Sea to the mean and Laptev Sea and East Siberian Sea in long-term trends) and high latitude oceans (Supplementary Fig. B2).

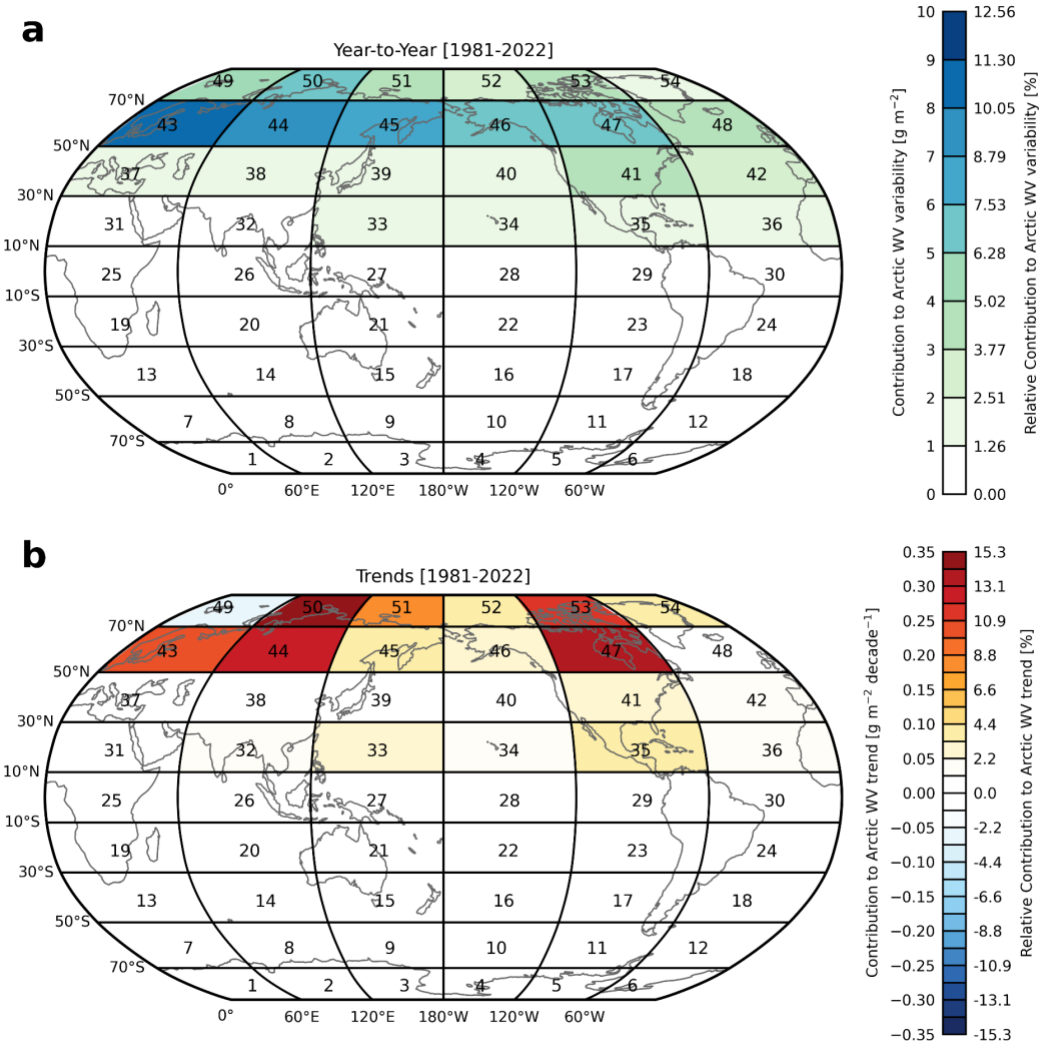

Figure 3.3 Sources of interannual variability and long-term trends in Arctic water vapor. a,b, Root mean square error (kg m^{-2}) when each region is removed from JJA Arctic (70-90° N) total column precipitable water (**a**) and linear decadal trends (1979-2022, g m^{-2} $decade^{-1}$) in JJA Arctic (70-90° N) total column precipitable water (**b**) sourced from each of the 54 tagged

source regions. Numbers indicate the source region number or tag. Shading corresponds to the magnitude of the RMSE (**a**) or trend (**b**) on the left side of the color bar and the relative contribution (% of total) on the right of the color bar. Contributions are standardized by the area of the source region (See Methods).

We quantify the radiative impacts of moisture transport by applying the ERA5 (Fig. 3.4) and CAM5 (Supplementary Fig. B3) radiative kernels to the linear trends (1981-2022) in specific humidity from iCESM1 (Pendergrass et al. 2018; Huang and Huang 2023). The total summertime Arctic WV surface radiative feedback determined from the trends in the nudged iCESM1 simulations is 1.82 W m^{-2} K^{-1}. Northeastern North America contributes 0.335 W m^{-2} K^{-1} (18.4%) to the Arctic WV feedback in terms of the long-term change over the satellite era. Locally, moisture sourced through evaporation from the Arctic Ocean contributes to 15.9% (0.291 W m^{-2} $decade^{-1}$) of the WV radiative feedback computed over the historical period, and remote sources account for the remaining 77%. This local contribution primarily results from a positive radiative effect originating from the Laptev Sea (region 50, 0.103 W m^{-2} K^{-1}) and the Canadian Arctic Archipelagos (region 53, 0.128 W m^{-2} K^{-1}). Though counterintuitive with global warming driving decreased sea ice cover over the Arctic, weak air-sea temperature gradients and lower tropospheric stability limit the local contribution to moistening and the WV radiative effect during summer, leaving remote transport the dominant contributor to the JJA Arctic WV radiative effect (Kay and Gettelman 2009; Morrison et al. 2019).

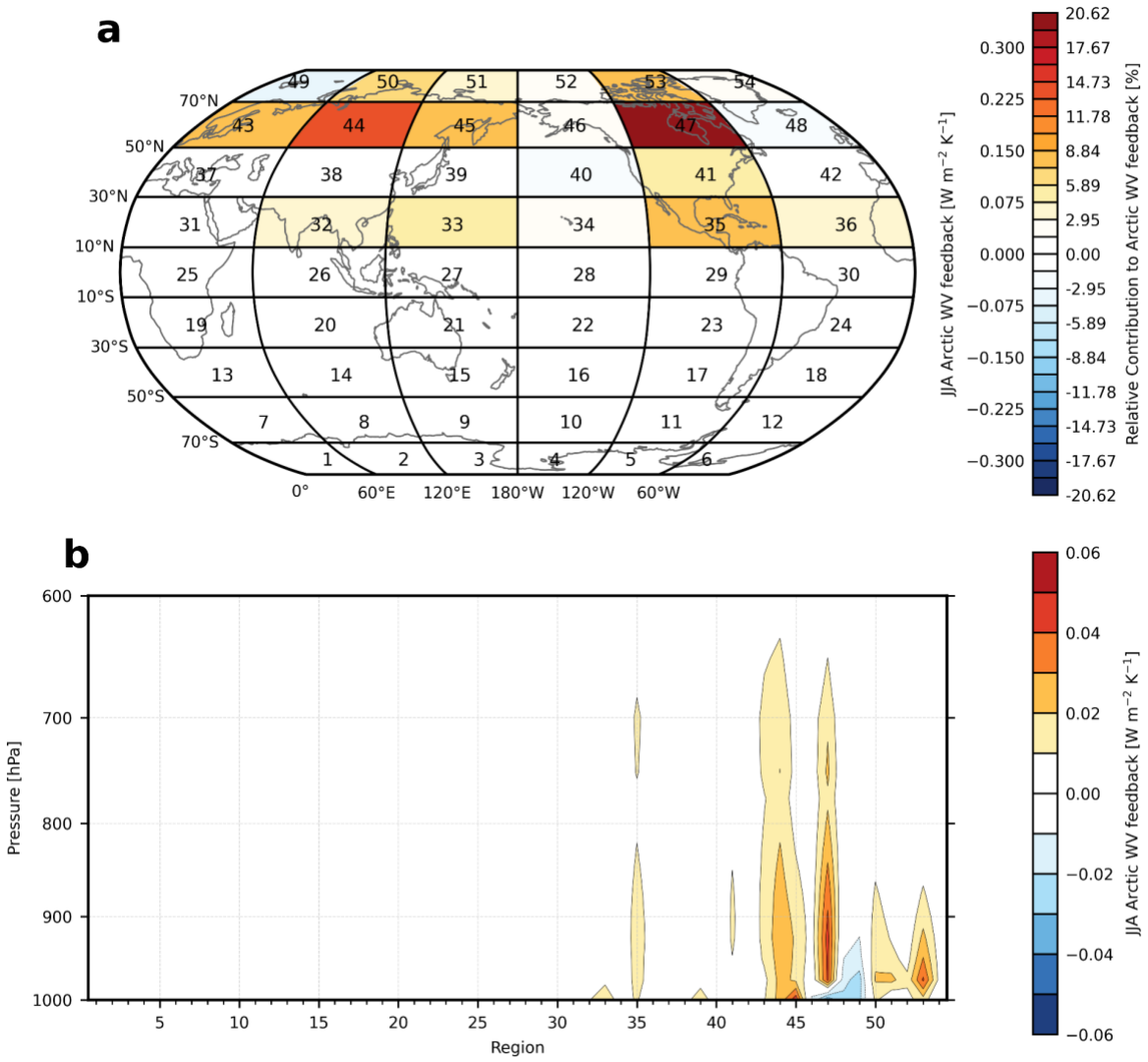

Figure 3.4 Regional contribution to the Arctic summertime surface water vapor radiative feedback. A, Total column integrated WV radiative effect (W m^{-2} K^{-1}) computed by removing WV sourced from each region using the ERA5 radiative kernel approach (**a**) (Methods). Numbers indicate the source region number or tag. Shading corresponds to the magnitude of the JJA Arctic WV radiative response (W m^{-2} K^{-1}) on the left side of the color bar and the relative contribution (% of total) on the right of the color bar. **B,** Vertical structure of Arctic (70-90° N) WV radiative (W m^{-2} K^{-1}), computed by removing WV from each tagged source region (x-axis) (**b**). Region numbers on x-axis in (**b**) correspond to numbered labels in panel (**a**).

Radiative feedbacks are typically examined using a column-integrated or surface perspective, but this can overlook the impacts of vertical changes in moisture and temperature

that modulate radiative fluxes. The radiative kernel approach used here reveals that the WV radiative effect within the column can be vertically uniform or unevenly distributed when considering changes over the satellite record. The strongest WV radiative effect occurs in the lower troposphere, between 850 and 1000 hPa, in the vertical range of the majority of poleward moisture transport (Fig. 3.4b). Moisture sourced from land sources over northeastern North America and northern Eurasia produce the strongest positive WV radiative effect throughout the atmosphere, with more remote, subtropical source regions affecting higher altitudes (~700 hPa) and the local sources affecting lower altitudes (>900 hPa). The moisture transport from western Eurasia (regions 43) exhibits a strong moistening trend (Fig. 3.3), but this transport contributes unevenly to the vertical structure of the WV radiative effect, being positive at mid- to upper levels but negative at lower levels (Supplementary Fig. B4a). In contrast, the WV changes originating from central and eastern Eurasia (regions 44, 45) extend down to the surface, inducing a much stronger radiative effect, despite region 45 having a much weaker moistening trend than region 43. Northeastern North America, despite a small negative radiative effect near the surface, has the most extensive warming throughout the lower levels of the column, creating the strongest contribution to the positive Arctic WV radiative effect (Supplementary Fig. B5c).

3.6 Diverse land capacitor effects between continental source regions

Because central and eastern Canada (region 47) appears to be particularly effective in inducing the summertime WV radiative effect (16.0%, Fig. 3.4a), we run an additional simulation with 9 smaller regions within the area of interest (Supplementary Fig. B5d). The vertical structure of trends originating from region 47 suggest this radiative efficiency is likely

due to increased transport at throughout middle to lower levels (Supplementary Fig. B5c). Other regions (i.e., 41, 43) have much weaker radiative impacts because over recent decades their transport has been pushed to higher elevations (Supplementary Fig. B4a-b), reducing their capability to travel farther distances into the Arctic and influence surface radiative fluxes.

The strongest source regions originating from central and eastern Canada (region 47) are from the southern and southwestern areas, just south of Hudson Bay (Supplementary Fig. B5d). These regions coincide with the strongest positive soil moisture trend (Supplementary Fig. B5e). Moisture sourced from the leading regions contributing to Arctic moistening generally leaves behind drying trends both globally and over midlatitude land masses (Supplementary Fig. B5e, Supplementary Fig. B6a). The one exception is over central and eastern Canada (region 47), where there is an increasing signal in soil moisture (red box in Supplementary Fig. B5e). This suggests that even though the region is a leading contributor to moisture redistribution from the midlatitudes to the Arctic, there is a capacitor effect, where recycling of moisture from the tropics or the buildup of soil moisture supplies transport into the Arctic over several decades. Land and soil processes in region 47 likely enhance moisture storage through time, which can then be transported to the Arctic and strongly influence summertime Arctic moistening and radiative feedbacks.

The soil creates a land capacitor effect by storing incoming precipitation from remote, equatorward regions. During spring, much of the moisture originates and is evaporated from the Caribbean and tropical Atlantic (regions 35 and 36), accounting for 54% of the precipitation trends over northeastern North America (Fig. 3.5a). During summer, the source of this moisture shifts to the Caribbean and continental United States (regions 35 and 41, 35.6%). The Caribbean and tropical Atlantic are the key source regions supplying this increase in soil

moisture over central and eastern Canada via precipitation in May and June (Fig. 3.5a). A Bermuda high type anticyclonic circulation trend over the subtropical Atlantic, paired with an elongated ridge extending over Greenland, drives this poleward moisture transport over northeastern North America (Supplementary Fig. B5e). Much of the transport originating from these tropical sources continues into the Arctic, though precipitation along the way feeds land-sourced moisture towards the end of the summer season. Changes in local recycling in both spring and summer can only explain as much as 18% of the precipitation trends driving increases in soil moisture, with most of the locally evaporated WV being transported and precipitated northward in the Arctic (Fig. 3.5d). Despite previous studies suggesting that land-sourced moisture is most important for summertime Arctic WV increases and the associated radiative impacts, this moisture originally comes from the Caribbean Sea and tropical Atlantic before being deposited in the land surface in northeastern North America and ultimately being transported into the Arctic. This highlights the importance of accurately capturing land surface processes because they facilitate the interactions between the Arctic and lower latitudes, and therefore the rate of Arctic Amplification. These results also highlight the need for caution when interpreting tagging and backtracking approaches to understand the sources of Arctic moisture change.

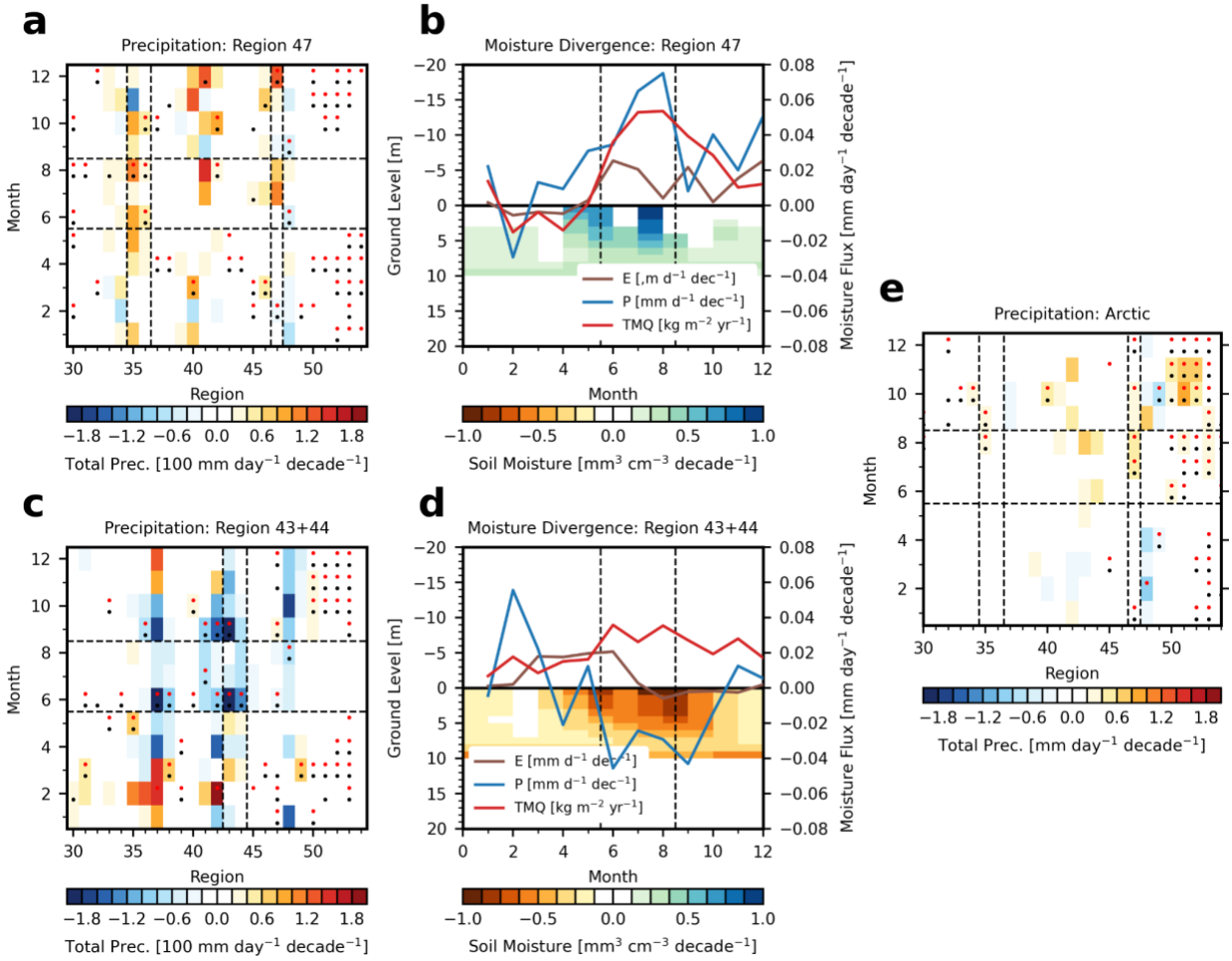

Figure 3.5 A land capacitor effect mediating poleward moisture transport. a,c, Linear trends (1981-2022) in rainfall precipitation (mm day^{-1} decade^{-1}) from regions in the Northern Hemisphere (regions 30-54) over region 47 (**a**) and regions 43 and 44 (**c**). Vertical dashed black lines denote region 35 and 36 (Caribbean Sea and tropical Atlantic) and region 47 (central and eastern Canada) in panel (**a**), and region 43 and 44 (western and central Eurasia) in panel (**c**). **b,** Linear trends (1981-2022) in column-mean soil moisture over vegetated land surfaces (mm^{-3} cm^{-3} decade^{-1}) over central and eastern Canada (region 47). Monthly mean trends (1981-2022) in evaporation (blue curve, cm day^{-1} decade^{-1}), total precipitation (brown curve, cm day^{-1} decade^{-1}), and total precipitable water (red curve, kg m^{-2} decade^{-1}) over central and eastern Canada (region 47) (**b**). **e,** Linear trends (1981-2022) in rainfall precipitation (mm day^{-1} decade^{-1}) over the Arctic from regions in the Northern Hemisphere (regions 30-54) (**c**). Horizontal (panel **a**, **c**, and **e**) and vertical (panel **b** and **d**) dashed black lines denote boreal summer (JJA). Black and red dots denote statistically significant trends at the 95% confidence level using a two-side t-test and Mann-Kendall test, respectively.

In contrast, moisture transport from western and central Eurasia (regions 43-44) exhibit decreasing precipitation trends in boreal summer (-0.033 mm day^{-1} $decade^{-1}$) but increases in February (0.056 mm day^{-1} $decade^{-1}$) due to increasing large-scale rainfall (0.048 mm day^{-1} $decade^{-1}$) (Fig. 3.5c-d). Between February and May, a South Asian high pattern over low latitude Eurasia contributes to rainfall over northern central Eurasia (Supplementary Fig. B4d). Sources of rainfall over the region primarily originate from lower latitudes, such as from the Mediterranean Sea (region 37, 16.8%) and local recycling (region 43+44, 24.4%). Decreasing precipitation from March through June coincides with increasing evaporation (0.0157 mm day^{-1} $decade^{-1}$), increasing moisture divergence (0.0158 mm day^{-1} $decade^{-1}$), and soil moisture drying (-0.036 mm mm^{-3} $decade^{-1}$) (Fig. 3.5d). These drying trends are associated with a strengthening anticyclonic circulation trend that is part of a high wavenumber feature along the jet over Europe and eastern/central Eurasia, which prevents transport to and precipitation in the region as well as induces subsidence-driven warming that enhances evaporation and soil moisture depletion (Supplementary Fig. B4). The Eurasian transport pathway shows an opposite influence, relative to that over North America, of large-scale circulation on the sources of moisture contributing to increasing WV in the Arctic.

3.7 Summary & Conclusions

Contrary to expectations, local open water and evaporation plays a relatively minor role in increasingly moistening the summertime Arctic atmosphere and the subsequent radiative impacts. Locally sourced moisture contributes to 15.8% (39% normalized for area) of total column WV trends and 17.1% of the WV radiative effect across the satellite era. Weak air-sea temperature gradients in the Arctic limit the surface's ability to influence the atmosphere

through evaporation or latent heat fluxes during summer (Kay et al. 2016). Conversely, remote sources contribute to 84.2% (61% normalized) of the moistening trend and 82.9% of the summer WV radiative feedback in the Arctic over the last 42 years. The dominant contribution from sources outside the Arctic highlights the need to understand the importance of large-scale circulation in steering to the processes driving poleward moisture transport and its impacts on polar climate. In our simulations, we also find changes in moisture sinks, represented by a decrease in precipitation efficiency (defined as the change in precipitation divided by change in water path) through reduction of cloud ice in Arctic mixed-phase clouds, which increases the lifetime of water vapor in the atmosphere and its radiative impact (Supplementary Fig. B7). Thus, remote moisture sources may induce stronger Arctic Amplification through an efficient phase "partitioning" change of local clouds.

Given that the WV feedback is a key component of Polar Amplification, more efforts should be spent to understand its significance. However, moisture transport over the historical period has shown a potentially strong response to internal variability, highlighting the need to understand changes in circulation over the historical record and into the future (Wills and Schneider 2016). In addition, models tend to be biased in their representations of large-scale SST trends (Wills et al. 2022). This is particularly evident in the negative tropical WV feedback from the iCESM1 simulations that use observed SSTs (Supplementary Fig. B7-8). Therefore, it is also important to consider large biases in simulated SSTs and their influence on moisture availability and atmospheric circulation when comparing observed trends from the satellite record.

Results from the iCESM1 simulations suggest that land processes are especially important in mediating poleward transport, especially in boreal summer, despite this moisture originating

from the ocean or the tropics. Soil moisture over the satellite record shows drying trends across most of the Earth, except over central and eastern Canada, (Fig. 3.5b). However, northern North America (region 47) shows increasing WV directly above the region that likely helps to retain soil moisture, while region 41 shows drying throughout the local atmosphere and soil (Fig. 3.5). A similar land capacitor effect also operates in other regions (west and central Eurasia), with soil moisture being key to supplying increased poleward transport, as the only potential sources feeding the trends over Eurasia are associated with wintertime precipitation originating from the Atlantic. This indicates that the Arctic moisture sources are very diverse and poleward transport is complex, including direct and indirect pathways that rely on high latitude land-ocean-atmosphere interactions. This is understandable, since the average residence time of WV in the atmosphere is only a few days, making a land capacitor effect, such as that identified in central and eastern Canada, necessary to relay the stronger moisture influx originating from the lower latitudes to the Arctic. This analysis also suggests that a shift in the phase of atmospheric circulation trends could alter the sources and pathways of moisture transport to the Arctic and therefore the importance of WV in determining the rate of Arctic Amplification.

Our new findings regarding the land capacitor's role in mediating poleward moisture transport still needs to be further reconciled with conceptual frameworks built on the importance of the tropics for determining polar moistening, as the pole-to-equator moist static energy (MSE) gradient framework may oversimplify issues of sources and transport pathways. For example, the upward branch of the Ferrel cell (around 60-70° N) may play a key role in determining the moistening trend in the Arctic, as the large-scale zonal mean circulation cells are likely very important for determining poleward and upward moisture transport. In

particular, transport over this zone is dominated by the zonal mean component of eddy transport ($v'q'$, omega'q') as indicated by the impact of ARs from 50 to 70° N. However, ARs are sensitive to circulation changes that are also driven by internal variability of the climate system. This suggests a scenario by which internal variability interacts with anthropogenic forcing. This is a potential mechanism that needs more attention in future model evaluations.

It has been theorized that changes in the equator-to-pole temperature and moisture gradients could modify large-scale circulation patterns and storm tracks. It should be noted that during boreal summer these gradients are relatively small, and the anthropogenically forced response from climate models induces very weak regional changes, especially in atmospheric circulation. Therefore, with the impacts of wind-driven changes for moisture transport highlighted in this study, we emphasize the importance of understanding atmospheric variability and the pattern effect – which can simultaneously drive evaporation and transport – while also modulating meridional gradients and global temperature imbalances that are the foundation for simplified feedback frameworks. These results also highlight the importance of the fully-coupled atmosphere-ocean-cryosphere-land system in determining regional climate change impacts. In the future, better constraints on the interaction of the forced response and internal variability can help us better project changes in Arctic moisture and precipitation under increasing greenhouse gas concentrations. This understanding will also help us better simulate the forced response in global climate models and reduce the uncertainty in earth system model climate sensitivity resulting from changes in moisture availability and transport. In particular, the combined approach including water tagging, circulation nudging and radiation calculation developed in this study may serve as a useful tool to enable us better understand the global hydrological cycle in reality.

3.8 Declarations

3.8.1 Funding

This study was supported by Climate Variability and Predictability (NA18OAR4310424) and Modeling, Analysis, Predictions, and Projections (NA19OAR4310281) programs as part of NOAA's Climate Program Office, and NSF's Polar Programs (OPP-1744598). We acknowledge the CESM Large Ensemble Community Project and supercomputing resources provided by NSF/CISL/Yellowstone (https://doi.org/10.5065/D6RX99HX). We thank the CESM Polar Climate Working Group for discussion and computing support.

3.8.2 Conflicts of interest/Competing interests

The authors declare that they have no conflict of interest.

3.8.3 Availability of data and material

ERA5 is available at https://cds.climate.copernicus.eu/#!/home. The iCESM1.2 is available for download at https://github.com/NCAR/iCESM1.2. Data and code for plotting in this study will be made available at https://github.com/itbaxter/Moisture-Tagging/ upon publication. Full model output is available upon request.

References

Armour, K. C., N. Siler, A. Donohoe, and G. H. Roe, 2019: Meridional Atmospheric Heat Transport Constrained by Energetics and Mediated by Large-Scale Diffusion. *J. Clim.*, **32**, 3655–3680, https://doi.org/10.1175/JCLI-D-18-0563.1.

Barrett, A. P., J. C. Stroeve, and M. C. Serreze, 2020: Arctic Ocean Precipitation From Atmospheric Reanalyses and Comparisons With North Pole Drifting Station Records.

J. Geophys. Res. Oceans, **125**, e2019JC015415, https://doi.org/10.1029/2019JC015415.

Baxter, I., and Q. Ding, 2022: An Optimal Atmospheric Circulation Mode in the Arctic Favoring Strong Summertime Sea Ice Melting and Ice–Albedo Feedback. *J. Clim.*, **35**, 6627–6645, https://doi.org/10.1175/JCLI-D-21-0679.1.

Bintanja, R., and F. M. Selten, 2014: Future increases in Arctic precipitation linked to local evaporation and sea-ice retreat. *Nature*, **509**, 479–482, https://doi.org/10.1038/nature13259.

Bonan, D. B., N. Feldl, M. D. Zelinka, and L. C. Hahn, 2023: Contributions to regional precipitation change and its polar-amplified pattern under warming. *Environ. Res. Clim.*, **2**, 035010, https://doi.org/10.1088/2752-5295/ace27a.

Box, J. E., and Coauthors, 2019: Key indicators of Arctic climate change: 1971–2017. *Environ. Res. Lett.*, **14**, 045010, https://doi.org/10.1088/1748-9326/aafc1b.

Brady, E., and Coauthors, 2019: The Connected Isotopic Water Cycle in the Community Earth System Model Version 1. *J. Adv. Model. Earth Syst.*, **11**, 2547–2566, https://doi.org/10.1029/2019MS001663.

Byrne, M. P., and P. A. O'Gorman, 2015: The Response of Precipitation Minus Evapotranspiration to Climate Warming: Why the "Wet-Get-Wetter, Dry-Get-Drier" Scaling Does Not Hold over Land. *J. Clim.*, **28**, 8078–8092, https://doi.org/10.1175/JCLI-D-15-0369.1.

Chapin, F. S., and Coauthors, 2005: Role of land-surface changes in arctic summer warming. *Science*, **310**, 657–660, https://doi.org/10.1126/SCIENCE.1117368.

Chung, P.-C., and N. Feldl, 2023: Sea Ice Loss, Water Vapor Increases, and Their Interactions with Atmospheric Energy Transport in Driving Seasonal Polar Amplification. *J. Clim.*, **1**, 1–28, https://doi.org/10.1175/JCLI-D-23-0219.1.

Ding, Q., A. Schweiger, and I. Baxter, 2022: Nudging Observed Winds in the Arctic to Quantify Associated Sea Ice Loss from 1979 to 2020. *J. Clim.*, **35**, 6797–6813, https://doi.org/10.1175/JCLI-D-21-0893.1.

Fearon, M. G., J. D. Doyle, and P. M. Finocchio, 2023: Soil Moisture Influences on Summer Arctic Cyclones and Their Associated Poleward Moisture Transport. *Mon. Weather Rev.*, **151**, 1699–1716, https://doi.org/10.1175/MWR-D-22-0264.1.

Feldl, N., and T. M. Merlis, 2023: A Semi-Analytical Model for Water Vapor, Temperature, and Surface-Albedo Feedbacks in Comprehensive Climate Models. *Geophys. Res. Lett.*, **50**, e2023GL105796, https://doi.org/10.1029/2023GL105796.

Graham, R. M., and Coauthors, 2019: Evaluation of Six Atmospheric Reanalyses over Arctic Sea Ice from Winter to Early Summer. *J. Clim.*, **32**, 4121–4143, https://doi.org/10.1175/JCLI-D-18-0643.1.

Guan, B., and D. E. Waliser, 2015: Detection of atmospheric rivers: Evaluation and application of an algorithm for global studies. *J. Geophys. Res. Atmospheres*, **120**, 12514–12535, https://doi.org/10.1002/2015JD024257.

——, and ——, 2019: Tracking Atmospheric Rivers Globally: Spatial Distributions and Temporal Evolution of Life Cycle Characteristics. *J. Geophys. Res. Atmospheres*, **124**, 12523–12552, https://doi.org/10.1029/2019JD031205.

Hahn, L. C., K. C. Armour, M. D. Zelinka, C. M. Bitz, and A. Donohoe, 2021: Contributions to Polar Amplification in CMIP5 and CMIP6 Models. *Front. Earth Sci.*, **9**.

Harrington, T. S., J. Zhu, and C. B. Skinner, 2021: Terrestrial sources of summer arctic moisture and the implication for arctic temperature patterns. *Npj Clim. Atmospheric Sci.*, **4**, 1–14, https://doi.org/10.1038/s41612-021-00181-y.

Held, I. M., and B. J. Soden, 2006: Robust Responses of the Hydrological Cycle to Global Warming. *J. Clim.*, **19**, 5686–5699, https://doi.org/10.1175/JCLI3990.1.

——, and K. M. Shell, 2012: Using Relative Humidity as a State Variable in Climate Feedback Analysis. *J. Clim.*, **25**, 2578–2582, https://doi.org/10.1175/JCLI-D-11-00721.1.

Hersbach, H., and Coauthors, 2020: The ERA5 global reanalysis. *Q. J. R. Meteorol. Soc.*, **146**, 1999–2049, https://doi.org/10.1002/qj.3803.

Holland, M. M., and C. M. Bitz, 2003: Polar amplification of climate change in coupled models. *Clim. Dyn.*, **21**, 221–232, https://doi.org/10.1007/s00382-003-0332-6.

Huang, H., and Y. Huang, 2023: Radiative sensitivity quantified by a new set of radiation flux kernels based on the ECMWF Reanalysis v5 (ERA5). *Earth Syst. Sci. Data*, **15**, 3001–3021, https://doi.org/10.5194/essd-15-3001-2023.

Huang, Y., and Coauthors, 2019: Thicker Clouds and Accelerated Arctic Sea Ice Decline: The Atmosphere-Sea Ice Interactions in Spring. *Geophys. Res. Lett.*, **46**, 6980–6989, https://doi.org/10.1029/2019GL082791.

Huffman, G. J., and Coauthors, 1997: The Global Precipitation Climatology Project (GPCP) Combined Precipitation Dataset. *Bull. Am. Meteorol. Soc.*, **78**, 5–20, https://doi.org/10.1175/1520-0477(1997)078<0005:TGPCPG>2.0.CO;2.

Hunke, E. C., 2010: Thickness sensitivities in the CICE sea ice model. *Ocean Model.*, **34**, 137–149, https://doi.org/10.1016/j.ocemod.2010.05.004.

Kay, J. E., and A. Gettelman, 2009: Cloud influence on and response to seasonal Arctic sea ice loss. *J. Geophys. Res. Atmospheres*, **114**, https://doi.org/10.1029/2009JD011773.

Kay, J. E., and Coauthors, 2015: The Community Earth System Model (CESM) Large Ensemble Project: A Community Resource for Studying Climate Change in the Presence of Internal Climate Variability. *Bull. Am. Meteorol. Soc.*, **96**, 1333–1349, https://doi.org/10.1175/BAMS-D-13-00255.1.

Kay, J. E., T. L'Ecuyer, H. Chepfer, N. Loeb, A. Morrison, and G. Cesana, 2016: Recent Advances in Arctic Cloud and Climate Research. *Curr. Clim. Change Rep.*, **2**, 159–169, https://doi.org/10.1007/s40641-016-0051-9.

Kopec, B. G., X. Feng, F. A. Michel, and E. S. Posmentiera, 2016: Influence of sea ice on Arctic precipitation. *Proc. Natl. Acad. Sci.*, **113**, 46–51, https://doi.org/10.1073/PNAS.1504633113.

Laguë, M. M., G. R. Quetin, and W. R. Boos, 2023: Reduced terrestrial evaporation increases atmospheric water vapor by generating cloud feedbacks. *Environ. Res. Lett.*, **18**, 074021, https://doi.org/10.1088/1748-9326/acdbe1.

Liu, C., and E. A. Barnes, 2015: Extreme moisture transport into the Arctic linked to Rossby wave breaking. *J. Geophys. Res. Atmospheres*, **120**, 3774–3788, https://doi.org/10.1002/2014JD022796.

Manabe, S., and R. T. Wetherald, 1975: The Effects of Doubling the CO2 Concentration on the climate of a General Circulation Model. *J. Atmospheric Sci.*, **32**, 3–15, https://doi.org/10.1175/1520-0469(1975)032<0003:TEODTC>2.0.CO;2.

Merlis, T. M., and M. Henry, 2018: Simple Estimates of Polar Amplification in Moist Diffusive Energy Balance Models. *J. Clim.*, **31**, 5811–5824, https://doi.org/10.1175/JCLI-D-17-0578.1.

Morrison, A. L., J. E. Kay, W. R. Frey, H. Chepfer, and R. Guzman, 2019: Cloud Response to Arctic Sea Ice Loss and Implications for Future Feedback in the CESM1 Climate Model. *J. Geophys. Res. Atmospheres*, **124**, 1003–1020, https://doi.org/10.1029/2018JD029142.

Neale, R. B., and Coauthors, Description of the NCAR Community Atmosphere Model (CAM 4.0).

Nusbaumer, J., T. E. Wong, C. Bardeen, and D. Noone, 2017: Evaluating hydrological processes in the Community Atmosphere Model Version 5 (CAM5) using stable isotope ratios of water. *J. Adv. Model. Earth Syst.*, **9**, 949–977, https://doi.org/10.1002/2016MS000839.

Oleson, K., and Coauthors, 2010: Technical Description of version 4.0 of the Community Land Model (CLM).

Parker, C. L., P. A. Mooney, M. A. Webster, and L. N. Boisvert, 2022: The influence of recent and future climate change on spring Arctic cyclones. *Nat. Commun.*, **13**, 6514, https://doi.org/10.1038/s41467-022-34126-7.

Pendergrass, A. G., A. Conley, and F. M. Vitt, 2018: Surface and top-of-atmosphere radiative feedback kernels for CESM-CAM5. *Earth Syst. Sci. Data*, **10**, 317–324, https://doi.org/10.5194/essd-10-317-2018.

Pithan, F., and T. Mauritsen, 2014: Arctic amplification dominated by temperature feedbacks in contemporary climate models. *Nat. Geosci.*, **7**, 181–184, https://doi.org/10.1038/ngeo2071.

——, and T. Jung, 2021: Arctic Amplification of Precipitation Changes—The Energy Hypothesis. *Geophys. Res. Lett.*, **48**, e2021GL094977, https://doi.org/10.1029/2021GL094977.

Schneider, U., A. Becker, P. Finger, A. Meyer-Christoffer, M. Ziese, and B. Rudolf, 2014: GPCC's new land surface precipitation climatology based on quality-controlled in situ data and its role in quantifying the global water cycle. *Theor. Appl. Climatol.*, **115**, 15–40, https://doi.org/10.1007/s00704-013-0860-x.

Screen, J. A., and I. Simmonds, 2010: The central role of diminishing sea ice in recent Arctic temperature amplification. *Nature*, **464**, 1334–1337, https://doi.org/10.1038/nature09051.

Serreze, M. C., and J. A. Francis, 2006: The Arctic Amplification Debate. *Clim. Change*, **76**, 241–264, https://doi.org/10.1007/s10584-005-9017-y.

Shell, K. M., J. T. Kiehl, and C. A. Shields, 2008: Using the Radiative Kernel Technique to Calculate Climate Feedbacks in NCAR's Community Atmospheric Model. *J. Clim.*, **21**, 2269–2282, https://doi.org/10.1175/2007JCLI2044.1.

Simpson, I. R., K. A. McKinnon, D. Kennedy, D. M. Lawrence, F. Lehner, and R. Seager, 2024: Observed humidity trends in dry regions contradict climate models. *Proc. Natl. Acad. Sci.*, **121**, e2302480120, https://doi.org/10.1073/pnas.2302480120.

Singh, H. K. A., C. M. Bitz, A. Donohoe, J. Nusbaumer, and D. C. Noone, 2016: A Mathematical Framework for Analysis of Water Tracers. Part II: Understanding Large-Scale Perturbations in the Hydrological Cycle due to CO2 Doubling. *J. Clim.*, **29**, 6765–6782, https://doi.org/10.1175/JCLI-D-16-0293.1.

——, ——, ——, and P. J. Rasch, 2017: A Source–Receptor Perspective on the Polar Hydrologic Cycle: Sources, Seasonality, and Arctic–Antarctic Parity in the Hydrologic Cycle Response to CO2 Doubling. *J. Clim.*, **30**, 9999–10017, https://doi.org/10.1175/JCLI-D-16-0917.1.

Smith, R., and Coauthors, The Parallel Ocean Program (POP) Reference Manual.

Soden, B. J., I. M. Held, R. Colman, K. M. Shell, J. T. Kiehl, and C. A. Shields, 2008: Quantifying Climate Feedbacks Using Radiative Kernels. *J. Clim.*, **21**, 3504–3520, https://doi.org/10.1175/2007JCLI2110.1.

Stroeve, J. C., V. Kattsov, A. Barrett, M. Serreze, T. Pavlova, M. Holland, and W. N. Meier, 2012: Trends in Arctic sea ice extent from CMIP5, CMIP3 and observations. *Geophys. Res. Lett.*, **39**, https://doi.org/10.1029/2012GL052676.

Topál, D., and Q. Ding, 2023: Atmospheric circulation-constrained model sensitivity recalibrates Arctic climate projections. *Nat. Clim. Change*, **13**, 710–718, https://doi.org/10.1038/s41558-023-01698-1.

Trenberth, K. E., 2011: Changes in precipitation with climate change. *Clim. Res.*, **47**, 123–138, https://doi.org/10.3354/cr00953.

Walsh, J. E., S. Bigalke, S. A. McAfee, R. Lader, M. C. Serreze, and T. J. Ballinger, 2023: NOAA Arctic Report Card 2023 : Precipitation. https://doi.org/10.25923/HCM7-AZ41.

Wang, C., R. M. Graham, K. Wang, S. Gerland, and M. A. Granskog, 2019: Comparison of ERA5 and ERA-Interim near-surface air temperature, snowfall and precipitation over Arctic sea ice: effects on sea ice thermodynamics and evolution. *The Cryosphere*, **13**, 1661–1679, https://doi.org/10.5194/tc-13-1661-2019.

Webster, M. A., C. Parker, L. Boisvert, and R. Kwok, 2019: The role of cyclone activity in snow accumulation on Arctic sea ice. *Nat. Commun.*, **10**, 5285, https://doi.org/10.1038/s41467-019-13299-8.

Wernli, H., and L. Papritz, 2018: Role of polar anticyclones and mid-latitude cyclones for Arctic summertime sea-ice melting. *Nat. Geosci.*, **11**, 108–113, https://doi.org/10.1038/s41561-017-0041-0.

Willmott, C. J., and K. Matsuura, 1995: Smart Interpolation of Annually Averaged Air Temperature in the United States. *J. Appl. Meteorol. Climatol.*, **34**, 2577–2586, https://doi.org/10.1175/1520-0450(1995)034<2577:SIOAAA>2.0.CO;2.

Wills, R. C., and T. Schneider, 2016: How Stationary Eddies Shape Changes in the Hydrological Cycle: Zonally Asymmetric Experiments in an Idealized GCM. *J. Clim.*, **29**, 3161–3179, https://doi.org/10.1175/JCLI-D-15-0781.1.

Wills, R. C. J., Y. Dong, C. Proistosecu, K. C. Armour, and D. S. Battisti, 2022: Systematic Climate Model Biases in the Large-Scale Patterns of Recent Sea-Surface Temperature and Sea-Level Pressure Change. *Geophys. Res. Lett.*, **49**, e2022GL100011, https://doi.org/10.1029/2022GL100011.

Xie, P., and P. A. Arkin, 1997: Global Precipitation: A 17-Year Monthly Analysis Based on Gauge Observations, Satellite Estimates, and Numerical Model Outputs. *Bull. Am.*

Meteorol. Soc., **78**, 2539–2558, https://doi.org/10.1175/1520-0477(1997)078<2539:GPAYMA>2.0.CO;2.

Yang, W., and G. Magnusdottir, 2017: Springtime extreme moisture transport into the Arctic and its impact on sea ice concentration. *J. Geophys. Res. Atmospheres*, **122**, 5316–5329, https://doi.org/10.1002/2016JD026324.

Zheng, C., Y. Wu, M. Ting, C. Orbe, X. Wang, and S. Tilmes, 2021: Summertime Transport Pathways From Different Northern Hemisphere Regions Into the Arctic. *J. Geophys. Res. Atmospheres*, **126**, e2020JD033811, https://doi.org/10.1029/2020JD033811.

Chapter 4

The role of atmospheric circulation in high latitude extreme aerosol transport events during the MOSAiC field expedition (2019-2020)

I.T. Baxter

In collaboration with: H. Wang, Q. Ding, H. Brown, Y. Huo, B. Guan, Y. Yang

Abstract

The role of atmospheric aerosols is a key uncertainty in the response of the polar regions to continued anthropogenic warming as aerosols can modulate radiative fluxes directly through absorption and scattering as well as indirectly through their interactions with clouds and surface albedo. In recent years, model development and analysis has highlighted an increasing importance of aerosols in determining simulated trends in Arctic climate change over the historical period. However, despite a strong sensitivity to aerosol forcing, global climate models, such as the Energy Exascale Earth System Model (E3SMv2), underestimate meridional transport and concentrations of aerosols at high latitudes relative to observations and reanalysis, degrading confidence in their ability to simulate historical and future changes in polar climate. To understand the causes and implications of this underestimation, we conduct

E3SMv2 simulations with winds nudged to those from the Modern Era Retrospective Reanalysis version 2 (MERRA-2) and aerosol source-region tagging. Our analysis focuses on the 2019-2020 Multidisciplinary drifting Observatory for the Study of Arctic Climate (MOSAiC) expedition period to utilize in situ measurements from the central Arctic. We find improved agreement between MOSAiC black carbon measurements and simulated transport events when specific large-scale circulation patterns determining key transport pathways are captured. Extending the concept of atmospheric rivers to extreme aerosol transport events, we also find a key role of aerosol atmospheric rivers (AARs) in contributing to extremely high concentrations during MOSAiC. We then compare AARs in the E3SMv2 to similar events simulated in E3SMv2-Arctic, which has regionally refined ocean and atmospheric horizontal grids poleward 45°N, to identify resolution sensitivity of the filamentary aerosol transport, finding improvement in AAR frequency but not transport with higher resolution.

4.1 Introduction

The Arctic has warmed at an accelerated rate compared to the global mean surface temperature, resulting the dramatic decline of snow and ice cover at high latitudes (Serreze and Francis 2006; Stroeve and Notz 2015; Comiso et al. 2008; Mouginot et al. 2019). This amplified warming has been attributed to complex interactions between the strong feedback processes in the region(Pithan and Mauritsen 2014; Goosse et al. 2018; Hahn et al. 2021). These processes, such as the surface albedo and cloud feedbacks, can be extremely sensitive to changes in black carbon (Serreze and Barry 2011; AMAP 2011). Black carbon (BC) can exacerbate this amplified polar warming through several direct and indirect ways (Flanner 2013; Schmale et al. 2021). It can directly impact Arctic climate through changes in albedo, as

it is deposited on snow or ice, leading to large increases in absorbed shortwave radiation (Twomey et al. 1984; Clarke and Noone 1985; Warren and Wiscombe 1980; Brown et al. 2022). BC and other aerosols can also influence climate indirectly, primarily through its interactions with clouds properties as cloud condensation nuclei or ice nucleating particles (Koch and Del Genio 2010; Ding et al. 2019). In addition, BC and the nutrients that are transported together have also shown a potential to modify the biogeochemistry, even being linked to large phytoplankton blooms, which then emit more aerosols and potentially create a feedback loop (Kramshøj et al. 2016; Nielsen et al. 2019). The redistribution and transport of BC and other aerosols is also very important for understanding Arctic Amplification because they can impact the polar regions remotely by modifying global heat and energy gradients, which can generate increased poleward heat and moisture transport into the Arctic (Sand et al. 2013, 2017).

Ultimately, the total climate impacts of aerosols is unclear due to large uncertainties in the representation of emissions, transport and aerosol-cloud interactions (Zelinka et al. 2013; Pithan and Mauritsen 2014). This has led to questions about model representations of key climate change metrics, such as equilibrium sensitivity in Coupled Model Intercomparison Project Phase 6 (CMIP6) models, which increased a lot relative to its Phase 5 counterparts in response to aerosol forcing (aerosol-cloud interactions in the Southern Ocean) (Zelinka et al. 2020). It was also shown that too strong variability associated with GFED biomass burning emissions from 1997-2014 also played a strong role in rapidly decreasing Arctic sea ice cover in the Community Earth System Model version 2 (CESM2) during the historical period (DeRepentigny et al. 2022). These studies have highlighted the need to better constrain what might be considered too strong climate responses to aerosol forcing.

Understanding the processes determining aerosol transport to high latitudes is, therefore, key in accurately simulating changes in polar and global climate. It has been difficult to validate model simulations because there is a lack of observations in the region. Satellites measuring aerosol properties generally have large pole holes over the central Arctic and unable to record observations during polar night. Reanalysis products, such the Modern Era Retrospective Reanalysis version 2 (MERRA-2; Randles et al. 2017), are susceptible to model biases and a lack of data to assimilate in. In situ measurements are incredibly sparse and sporadic, with the majority of these field studies occurring over short intervals far from the central Arctic, near the North Atlantic or over land. However, between October 2019 and October 2020, the MOSAiC field expedition was anchored in the Arctic sea ice, taking measurements of some aerosol species (Shupe et al. 2022; Heutte et al. 2023; Boyer et al. 2023). The expedition noted several different types of intrusion events that influenced the field site, including one warm air intrusion that led to an extreme aerosol concentration events (Kirbus et al. 2023; Dada et al. 2022). This field expedition also coincided with the second and third leading high latitude biomass burning emission years since 1997, which has followed an increasing trend in recent years (Voronova et al. 2020; Ponomarev et al. 2021).

Recent studies have highlighted the increasing importance and occurrence of extreme events determining changes in Arctic climate, such as wildfires as well as atmospheric rivers (ARs) (Overland 2022; Zhang et al. 2023; Gong et al.). Atmospheric rivers are narrow, filamentary ribbons of moisture that are responsible for as much as 90% of poleward propagating water vapor into the polar regions (Nash et al. 2018). Chakraborty et al. (2021) first adapted a commonly used global AR detection algorithm (Guan and Waliser 2015) to detecting transport of sulfate, dust, sea spray, organic carbon, and BC aerosols from reanalysis

data, calling them aerosol atmospheric rivers (AARs). Extending this approach, it was found that AARs contribute to 40-80% of global and more than 14% of poleward aerosol transport (Chakraborty et al. 2021, 2022; Lapere et al. 2024). Combining this importance of extreme aerosol transport on the redistribution of key species around the Earth and the uncertainties in the impacts of aerosols on global and polar climate we must understand how these processes are represented in climate models.

Thus, in this study, we examine the relative impacts of large-scale circulation and emissions on Arctic radiative fluxes and cloud changes during the exceptional biomass burning year of 2019-2020. The following is organized as follows: 1.) We place 2019-2020 into the context of large-scale circulation changes and aerosol transport over the recent 30 years, identifying a consistent pattern modulating BC transport into the Arctic. 2.) The following section evaluates the ability of MERRA-2 and E3SMv2 to capture high latitude extreme transport events based on a composite analysis of anomalously large BC measurements by MOSAiC. 3.) The last section evaluates the representation of AAR frequency and BC transport into the Arctic across the reanalysis and model simulations.

4.2 Data and Methods

4.2.1 MOSAiC field measurements

The Multidisciplinary drifting Observatory for the Study of Arctic Climate (MOSAiC; Shupe et al. 2022) mission recorded several aerosol events that they traced back to both North America and central/eastern Eurasia using backward trajectory modeling (Engelmann et al. 2021; Boyer et al. 2023). These events occurred primarily during winter (January-March 2020). Studies generally use HYSPLIT backward trajectories to understand the sources of

these events, but the model makes several assumptions, such as there is no mixing of the air parcels with the surrounding environment.

To make comparisons with surface black carbon concentrations from MERRA-2 and E3SMv2, we follow the conversion of black carbon to equivalent black carbon, trying to maintain consistency with the approach taken by the MOSAiC scientists. This entails converting black carbon mixing ratio to concentration by dividing by the density of air. We then convert black carbon mass concentration to equivalent black carbon using the ratios of the mass absorption coefficients (4.74 m^2 g^{-1} and 7.77 m^2 g^{-1}) as well as dust mass concentration to reconstruct the approach taken using the measurements from the Photoacoustic extinctiometer (Momenimovahed et al. 2021).

4.2.2 MERRA-2 reanalysis

The observed AARs are detected using the Modern Era Retrospective Reanalysis version 2 (MERRA-2) hourly vertically integrated u-wind and v-wind mass flux for black carbon (Randles et al. 2017). MERRA-2 has been assessed capture black carbon AOD reasonably well in the Arctic when evaluated against satellite and station measurements (Xian et al. 2022). In our analysis we also evaluate the ability of MERRA-2 to capture extreme black carbon measurements observed at the MOSAiC field site, finding good agreement in key properties of BC burden and BC-AARs.

4.2.3 Maximum covariance analysis

Maximum covariance analysis (MCA) is used to determine the primary covarying patterns of Arctic atmospheric circulation and tropical SSTs. MCA analysis uses singular value

decomposition of a covariance matrix between detrended, deseasoned 500 hPa stream function and total column integrated black carbon concentration (Bretherton et al. 1992; Wallace et al. 1992). The leading patterns calculated using this method show the time series and spatial patterns of the two fields that are optimally coupled.

4.2.4 Aerosol Atmospheric River (AAR) Detection

We use two separate detection algorithms to detect AARs. The first is the tARgetv3 scheme by Guan and Waliser (2015, 2019). TARget3 uses both vIAT and uIAT to compute total integrated transport when determining both the percentile thresholds (85th percentile) and the total transport thresholds (Universal/vIAT). Chakraborty et al. (2021, 2022) previously tested sensitivity of AARs to the percentile threshold and found little difference in the detected events on a global scale.

This approach has also been expanded upon to target polar AARs using another detection scheme employed is the Wille et al. (2021) algorithm (Lapere et al. 2024). This algorithm has often been used to detect high latitude ARs, specifically those traveling towards the Antarctic continent. It was found that ARs impacting West Antarctica travel predominantly in a meridional direction, so it was determined that using only vIVT -- or in this case vIAT-- more efficiently represented the observed events around Antarctica. A higher percentile threshold (98th percentile) is also used on only vIAT relative to tARgetv3's more global focus (85th percentile).

Ultimately, we find that the differences in detection scheme are minimal when it comes to detecting specific AAR events. However, there are key differences in the structures of the AARs and the masks used to quantify related impacts. It should also be noted that tARget3

includes life cycle tracking, that could be included in the Wille et al. (2021) package. We find that when considering impacts, in terms of AAR statistics and their relationship with in situ, reanalysis, and satellite measurements, is it much more important to understand the life cycle of these events and how that changes conclusions.

Because the MOSAiC-MIP E3SMv2 simulations are only run for 2019-2020, thresholds computed using MERRA2 3-hourly, total column-integrated BC fluxes are also applied to model output. There are possible model mean state biases that are necessary to consider in this context, but using MERRA2 thresholds also offers a more direct comparison of aerosol transport. We find that the differences between the mean states of meridional BC fluxes in MERRA2 and E3SMv2 are relatively small.

4.2.5 Standard resolution E3SMv2 and aerosol tagging

We use 30 regions based on the AR6 reference regions (Iturbide et al. 2020), modified based on GFED4.1 and HTAP2 regions for wildfire and anthropogenic emissions, respectively. We have a local Arctic region that is based on the E3SMv2 land mask and encompasses the Arctic Ocean north of 70° N and the Greenland landmass. We use 30 regions in total, including a single non-Arctic Ocean, with the remaining 28 being land-based regions (Fig. 1). Our control run uses the CMIP6-SSP245 forcing scenario for 2020 and interpolated from 2015 to 2020 for 2019.

The model is run in the AMIP-style configuration using the HadISST sea surface temperatures and sea ice concentration globally (Durack and Taylor 2016). There is likely some interaction between the ocean and atmosphere that contributes to discrepancies in transport that we are not able to address in this model configuration.

Global horizontal winds (u, v) are nudged to those from 3-hourly instantaneous MERRA-2 reanalysis, using a 6-hour relaxation timescale. Nudging is limited to above ~850 hPa. The model is initialized on January 1, 2019 and the 9 months preceding the beginning of the MOSAiC field expedition can be considered spinup. In this setup, the large-scale circulation is well constrained both in the upper atmosphere and near the atmosphere-ocean-ice interface as the lower troposphere adjusts very rapidly to the nudging, despite it not being specified (Baxter and Ding 2022).

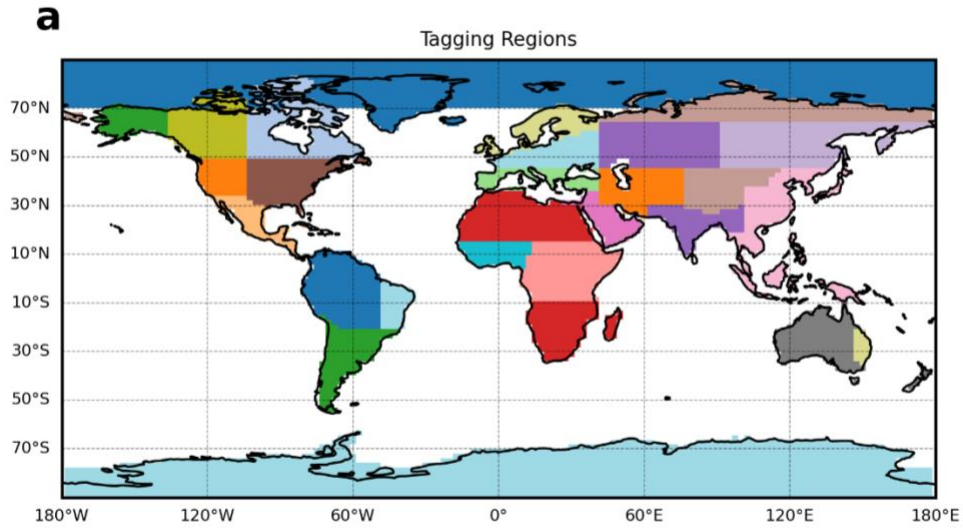

Figure 4.1. Map showing the 30 black carbon tagged source-receptor regions from industrial and biomass burning emissions. We consider the dark blue region, north of 70° N to be the local Arctic region and everywhere else to be remote.

4.2.6 E3SMv2-Arctic

E3SM-Arctic uses the regionally refined mesh grid capability of E3SMv2, having 0.25° resolution north of 45° N. This configuration requires a 15-minute time step, as opposed to the 30-minute time step of the standard resolution simulations. AARs are long, filamentary structures and therefore are expected to be sensitive to horizontal resolution. AARs are

typically 4000 km in length and 600 km in width and detection schemes generally use a xx km threshold as well as a 2.5 length-to-width cutoff. The purpose of comparisons using these runs is to quantify the sensitivity of extreme transport to resolution. We also examine the impacts of these AARs on Arctic climate, and their interactions with cloud processes are very sensitive to resolution and timestep. Winds are nudged to ERA5 reanalysis with a 6-hour relaxation timescale. The model is run in an AMIP-style configuration with the same sea surface temperature and sea ice specified as in the standard resolution simulation. The model also is forced with the same CMIP6-SSP245 scenario aerosol emissions and greenhouse gas concentrations as the standard resolution simulation.

4.3 Atmospheric Circulation Pattern transporting BC to the Arctic

We investigate the statistical connection between large-scale circulation and BC concentrations within the Arctic by first using Maximum Covariance Analysis (MCA) between MERRA-2 monthly detrend and deseasoned 500 hPa stream function in the Northern Hemisphere and total column BC burden with the Arctic (65-90° N) (Supplementary Fig. C1; see methods). The leading mode accounts for 63.2% of the covariance fraction and the spatial patterns show basin-wide decreases in BC burden coinciding with negative stream function magnitudes (cyclonic circulation) over the Arctic. The decrease in BC burden extends to over Siberia, where the magnitude becomes very large (Supplementary Fig. C1a). The negative circulation pattern covers the entirety of the Arctic and extends down over northeastern Canada and Greenland (Supplementary Fig. C1c). This is accompanied by an anticyclonic center in the midlatitudes over Europe, that can potentially divert pollution emitted from Europe westward rather directly north into the Arctic and leading to this negative BC pattern in the leading mode

(Supplementary Fig. C1c). One notable spike in the BC time series occurs in August 2019, which is unfortunately just before the beginning of the MOSAiC mission (Supplementary Fig. C1b).

To relate this change in Arctic BC to transport, we then project meridional BC flux from MERRA-2 onto the leading 500 hPa stream function mode to identify the leading pathways with the 500 hPa spatial pattern overlain (Fig. 4.1a). From this, we can more clearly see two anticyclonic centers – one over Europe and one over Siberia – that increase poleward transport on their western flanks and decrease transport on the eastern flanks. Again, this configuration reminiscent of a positive Artic Oscillation (AO; Thompson and Wallace 1998) coincides with lower concentrations of black carbon over the Arctic, and suggesting that to generate enhanced poleward transport this mode would need to be in its negative phase.

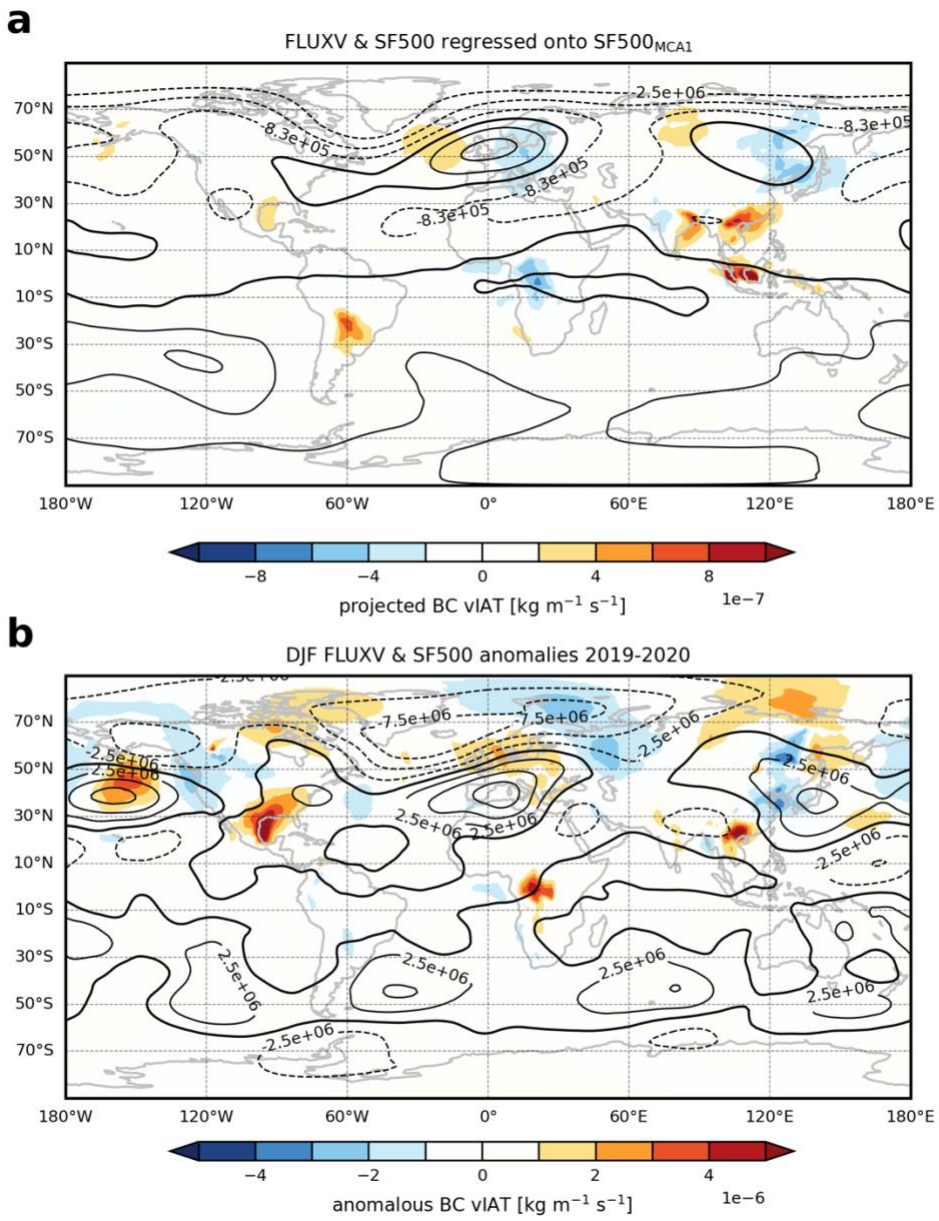

Figure 4.2 Optimal mode contributing to Arctic BC burden and its similarity with 2019-2020: (a) Projection of meridional BC IAT (shading, kg m^{-1} s^{-1}) and 500 hPa stream function (black contours) onto MCA1 500 hPa stream function time series. (b) Anomalous DJF meridional BC IAT and 500 hPa stream function relative to 1997-2018

If we examine the anomalous (relative to 1997-2018) circulation pattern represented by 200 hPa geopotential height anomalies, we find the 2019-2020 DJF, and to a lesser extent MAM, closely matches that from the leading MCA mode (r=0.87 for 30-90° N) (Supplementary Fig. C2a-b). 2019-2020 also saw a relatively strong positive AO during winter,

with cyclonic anomalies over the Arctic and anticyclonic structures over Europe and Siberia (Fig. 4.1b). In this year, there was stronger cyclonic circulation over the North Atlantic and Barents Sea and the high pressure over Europe and Siberia is displaced poleward. From its correlation with the leading MCA mode, circulation during winter and spring 2019-2020 likely worked to reduce transport of BC into the Arctic. Since the MCA signal is most representative of wintertime anomalies from 2019-2020, this might suggest that the basin-wide BC pattern might be linked to processes creating "Arctic haze" (Quinn et al. 2007; Engelmann et al. 2021).

4.4 Extreme eBC Events Measured by MOSAiC

Next, to link these changes in circulation, BC concentrations and transport to the MOSAiC expedition, we identify extreme BC events measured at the field site (Fig. 4.3). These extreme events are defined as equivalent BC (eBC) concentrations exceeding the 85th percentile per month, to maintain a definition roughly consistent with the AAR detection algorithm from Guan and Waliser (2019). Extreme events are identified and presented as time = 0, with the 5 preceding and 5 lagging days on either side. When compositing, we find large increases in the MOSAiC eBC measurements exceeding 900 ng m^{-3} and lasting approximately two days in total. We follow the same approach compositing MERRA-2 and E3SMv2 eBC based on the events identified from the MOSAiC dataset. Surface BC is converted from mixing ratio (kg kg^{-1}) to mass concentration (ng m^{-3}) and then converted to eBC using the ratios of the mass absorption coefficients for BC and dust to emulate the measurements taken using the Photoacoustic extinctiometer (Momenimovahed et al. 2021).

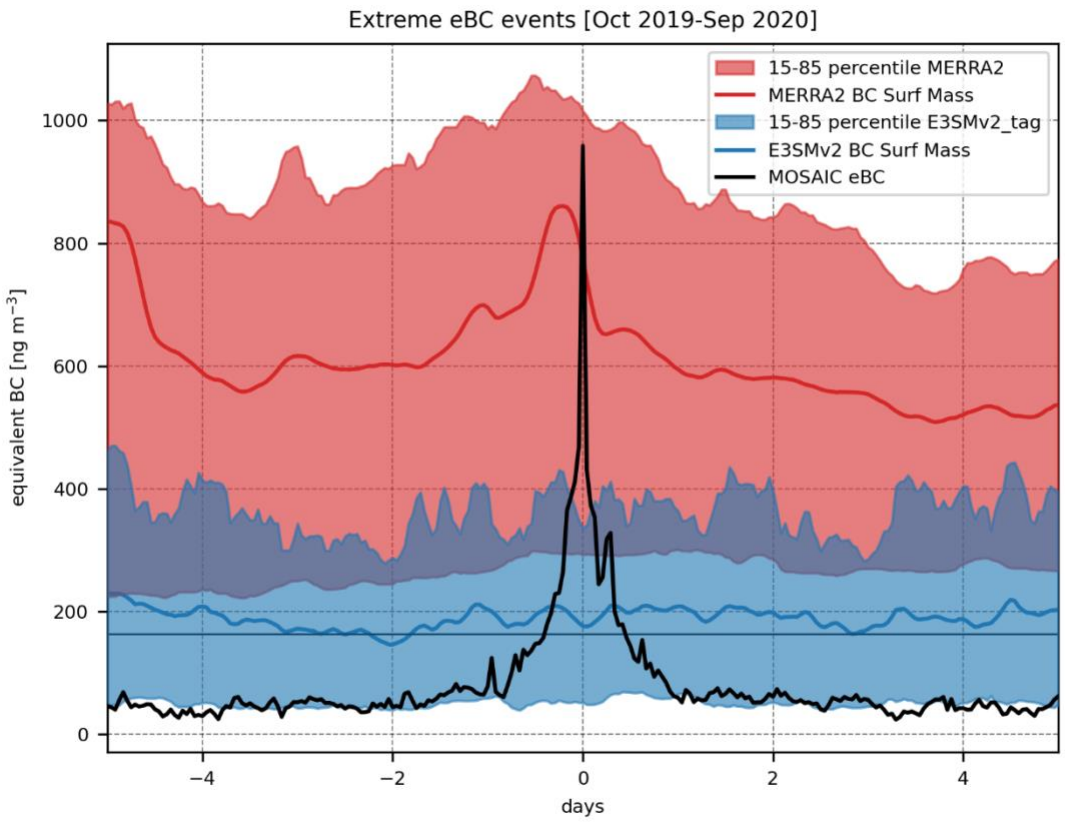

Figure 4.3 MOSAiC, MERRA-2 and E3SM extreme surface aerosol concentration events: eBC from MOSAiC (black), MERRA-2 (red) and E3SMv2_tag (blue) composited based on MOSAiC measurements that exceed the 85th percentile in each month. The curves show the mean across the events and the shading shows the 15th and 85th percentiles of those events.

MERRA-2 is able to capture coinciding increases in eBC that were observed by MOSAiC, though the reanalysis shows an increase 3 hours, or one time step, before observations (Fig. 4.3). MERRA-2 is able to capture these extreme aerosol events from MOSAiC much better during the winter months rather than summer and did exceptionally well at capturing the events that occurred during February 2020 (Supplementary Fig. C3). This may suggest that MERRA-2 is most appropriate for studies examining long-range transport of aerosols into the Arctic, but is not representing the local sources as well. E3SMv2_tag, on the hand, despite having the

same large-scale circulation via the nudging, does not exhibit any correspondence in increasing eBC concentrations relative to that from MOSAiC.

To determine where BC is being transported into the Arctic, we composite spatial maps of anomalous (relative to 1997-2018) BC IAT from MERRA-2 during these events (Fig. 4.4). Increasing poleward (red shading) BC IAT traveling from eastern Europe, central Eurasia, and Siberia leads extreme measurements at the MOSAiC site (black line in Fig. 4.4). Transport over North America also occurs at lead times of 2-3 days, but this flux does penetrate deep into the central Arctic where it could be picked up by the field expedition. The transport pathways contributing to extreme aerosol concentrations over the central Arctic corroborate results from the tagging, which show a very dominant contribution from East Asia (23.5% of total Arctic BC concentration) and Siberia (11%). Not evident from the BC flux composite maps, is the second leading contribution coming from South Asia (15%). These regions have been shown to contribute to aerosol concentrations at higher elevations, owing to how far they are from the Arctic (Wang et al. 2014; Ren et al. 2020). These regions are also the major emitters of BC in the CMIP6 future scenario forcing dataset, adding to their large contributions in this simulation.

From examining the extreme eBC events observed at the MOSAiC site, we are able to determine that aerosol transport in the colder seasons is well captured by MERRA-2, but E3SMv2 with CMIP6 emissions is not able to capture the observed events, despite constraining the circulation fields.

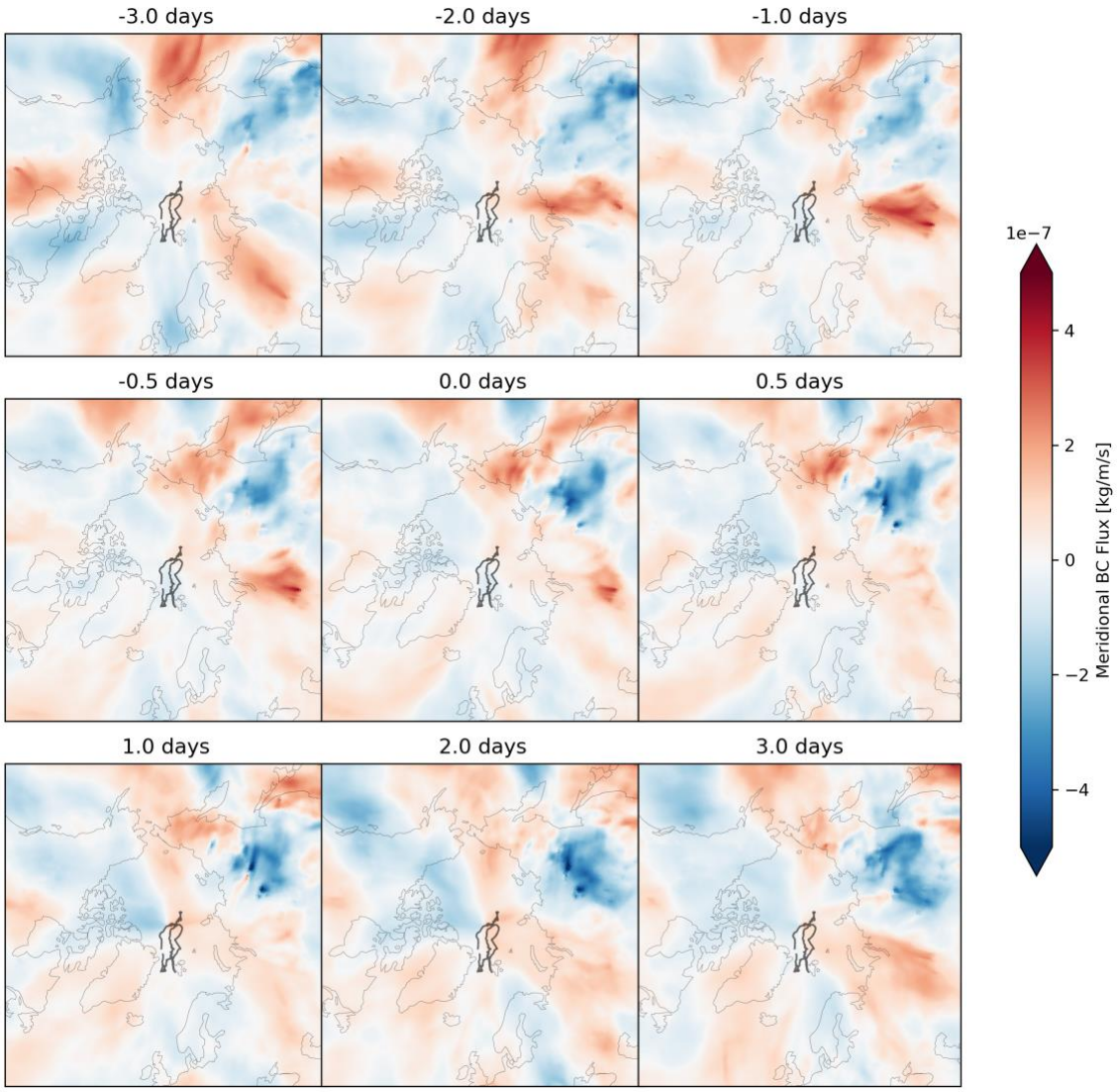

Figure 4.4 Composites of MERRA-2 aerosol transport and circulation during extreme MOSAiC events: Shading shows anomalous meridional BC flux composited based on extreme aerosol events measured by MOSAiC at time lags ranging from -3 to 3 days. The black line shows the MOSAiC drift track for Septmeber 2019 to August 2020.

4.5 Arctic AARs in E3SMv2

The E3SMv2 simulated aerosol transport during times of extreme eBC readings at the MOSAiC field site are lower than that seen in MERRA-2 (Fig. 4.3). Therefore, to evaluate these transport events from a more case-by-case basis, we examine aerosol atmospheric rivers

(AARs) to leverage their ability to identify and characterize specific events (see methods). In this case, we also expand this analysis to include an additional set of nudged simulations using the E3SMv2-Arctic (see methods). This is to account for the potential influence of model horizontal resolution, as aerosol depositional processes are tightly coupled to cloud microphysics, which are themselves sensitive to resolution (Hobbs 1993). BC-AAR frequency and meridional integrated BC aerosol transport (IAT) are aggregated to monthly means to compare with the 85th percentile of MOSAiC eBC concentrations per month (Fig. 4.7).

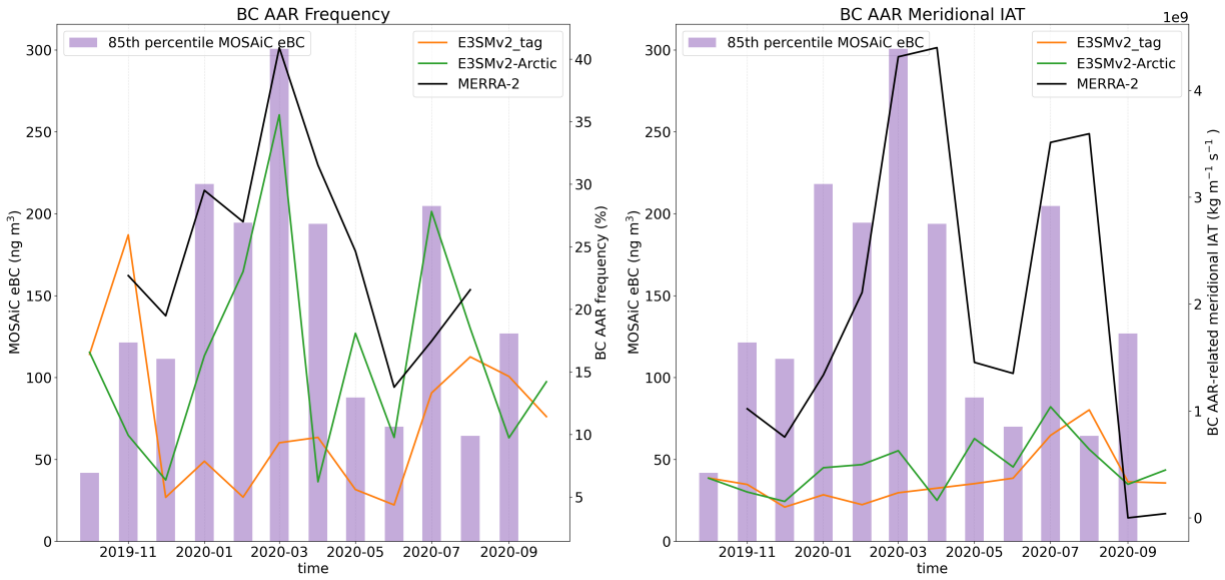

Figure 4.7 Comparison of AAR statistics in observations and models by month
(a) Area-weighted mean monthly mean BC AAR frequency (% of timesteps) from MERRA-2 (black), E3SMv2-Arctic (green), and E3SMv2_tag (orange) within the Arctic (70-90° N). (b) Monthly mean BC AAR associated meridional IAT at 70° N (kg m^{-1} s^{-1}) from MERRA-2 (black), E3SMv2-Arctic (green), and E3SMv2_tag (orange). Purple bars show the monthly 85th percentile of MOSAiC eBC concentrations.

We first evaluate BC-AAR frequency, finding that MERRA-2 has a higher occurrence of detected BC-AARs relative to E3SMv2 (Fig. 4.7a). There is an exception during July, when MERRA-2 registers a lower occurrence than E3SMv2-Arctic. This coincides with large concentrations in the observations. Overall, eBC corresponds very well with MERRA-2 and

E3SMv2-Arctic BC-AAR frequency (Fig. 4.7a). MERRA-2 captures the monthly variations marginally better during winter and spring, whereas E3SMv2-Arctic seems to show this correspondence with MOSAiC better during spring and summer. All three aforementioned products show peaks in eBC or BC-AAR frequency in March exceeding 300 ng m^{-3} and 35%, respectively. The standard 1-degree resolution E3SMv2_tag does not seem to be capturing the seasonal cycle of BC-AAR occurrence within the Arctic (Fig 4.7a). The E3SMv2 models struggle much more to capture the magnitude of poleward IAT into the Arctic relative to MERRA-2 (Fig 4.7b). MERRA-2 shows a close correspondence with the MOSAiC eBC 85th percentile measurements, with increased transport through winter that peaks in March and then again in July when there were large wildfires in northern Eurasia (Ponomarev et al. 2021). The magnitudes of poleward transport in MERRA-2 seem to better reflect the observations, whereas it is the opposite for E3SMv2-Arctic. This suggests that the winds and resolution play a more important role in capturing the occurrence of BC-AARs, while emissions are the dominant factor in determining the magnitude of aerosol transport.

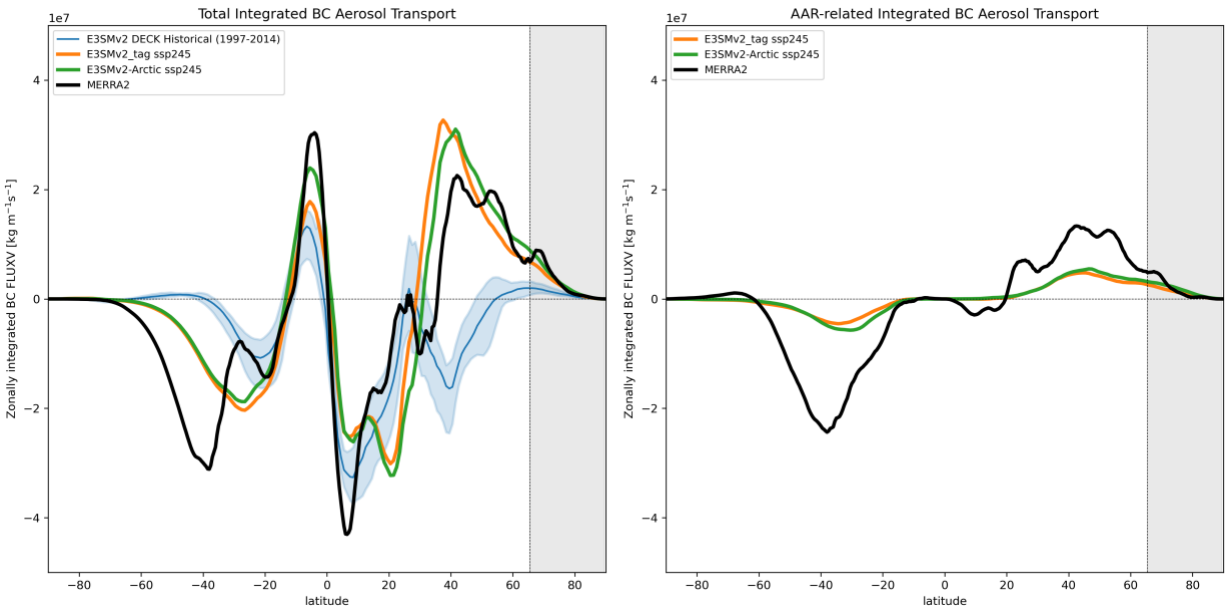

Figure 4.8 Poleward Moisture Transport in Models vs. Reanalysis: (a) Zonally integrated total integrated meridional BC transport from MERRA-2 (black), E3SMv2_tag (green) and E3SMv2-Arctic (orange) averaged over 2019-2020, as well as from the 5 members of the E3SMv2 DECK simulations (ensemble mean: blue curve, spread: blue shading) averaged over the GFED historical period (1997-2014). (b) AAR associated zonally integrated total integrated meridional BC transport from MERRA-2 (black), E3SMv2_tag (green) and E3SMv2-Arctic (orange) averaged over 2019-2020.

Approaching the differences between MERRA-2 and the E3SM simulations from a more global perspective, we lastly examine total integrated meridional BC transport at each latitude. When comparing the mean transport across 2019-2020, we find very little difference between MERRA-2 and both the nudged E3SMv2 simulations in Northern Hemisphere transport during the MOSAiC expedition (Fig. 4.8a). The free-running DECK simulations (blue in Fig. 4.8a) exhibit extremely weak meridional BC fluxes, with the 5-member ensemble spread not close to encompassing the fluxes with observed circulation, highlighting the importance of capturing large-scale circulation in order to capture the mean zonal pattern of BC redistribution.

In contrast, even with the imposed circulation, the E3SMv2 and E3SMv2-Arctic underestimate the magnitude of meridional transport carried in BC-AARs (Fig. 4.8b). Both E3SMv2 simulations with identical emissions and surface and nearly identical winds still underestimate transport into the Arctic by half in the 2019-2020 mean (Fig. 4b.8) and by up to 5/6 in certain months (Fig. 4.7b). The causes of this difference require future examination, but it is likely associated with some combination of emissions and depositional processes. Despite the need for ongoing research to continue to improve the representation of poleward aerosol transport in climate models, more accurate large-scale circulation, achieved here through nudging, shows potential.

4.6 Discussion and Conclusions

In this study, using a combination of wind nudging and BC aerosol source-receptor region tagging in the E3SMv2, we examine the large-scale circulation pattern contributing to extreme transport of BC to the Arctic and its correspondence with the MOSAiC field measurements. Through an MCA analysis, we find that a positive AO pattern is conducive to lower BC concentrations within the Arctic and that this pattern was very prominent during the winter and spring of 2019-2020, likely reducing BC transport to the MOSAiC site. Despite this prevailing wind pattern, in situ measurements still registered many instances of extreme BC concentrations which we use to examine the ability of MERRA-2 and a circulation constrained E3SMv2 simulation to capture these extremes. MERRA-2 shows a reliable ability to capture transport events along AARs that were observed in the central Arctic, while the E3SMv2 with nudged winds is not. Transport into the Arctic in MERRA-2 occurs along two narrow corridors over eastern Europe and Siberia and can be linked to the leading sources of BC in East and South Asia as well as Siberia using an online tagging capability in E3SMv2. Lastly, we find that constraining circulation yields large improvements in mean transport and the simulation of AAR occurrence but does alleviate underestimations of the magnitude of poleward aerosol transport.

The atmospheric circulation patterns shown here that generate the strongest increases/decreases in BC within the central Arctic are not so much associated with the local circulation, but the midlatitude configuration. High/low pressure centers over the midlatitude Europe and eastern Eurasia are the most prominent patterns determining extreme aerosol transport into the Arctic. Throughout the recent decades, when this pattern enters its negative phase (high pressure over the Arctic, low pressure over Europe and Siberia) is capable of

exciting large bursts of BC into the Arctic, which can have profound impacts on albedo, clouds and biochemistry. These results emphasize the key role that large-scale circulation plays in the redistribution of aerosols from their sources to remote regions, that is generally underestimated in climate models.

It should be noted that the modeling simulations presented here use the CMIP6 monthly aerosol emissions. This is not ideal for examining individual events and is likely a major cause of the differnce in the BC-AAR related poleward transport (Fig. 4.7b). Future work should focus on more faithfully representing emissions to what is observed in order to better capture these extreme transport events and their impacts on polar climate. This conclusion comes in contrast to some of the recent experiences with biomass burning variability and discontinuities in the forcing led to exaggerated sea ice decline in the CESM2 (DeRepentigny et al. 2022). The suggestion from this study opposite to smoothing biomass burning variability, instead advocating for increased variability through higher temporal and spatial resolution or prognostic representations of historical and future aerosol emissions.

References

AMAP, 2011: *The Impact of Black Carbon on Arctic Climate*. https://www.amap.no/documents/doc/the-impact-of-black-carbon-on-arctic-climate/746.

Baxter, I., and Q. Ding, 2022: An Optimal Atmospheric Circulation Mode in the Arctic Favoring Strong Summertime Sea Ice Melting and Ice–Albedo Feedback. *Journal of Climate*, **35**, 6627–6645, https://doi.org/10.1175/JCLI-D-21-0679.1.

Boyer, M., and Coauthors, 2023: A full year of aerosol size distribution data from the central Arctic under an extreme positive Arctic Oscillation: insights from the Multidisciplinary drifting Observatory for the Study of Arctic Climate (MOSAiC) expedition. *Atmospheric Chemistry and Physics*, **23**, 389–415, https://doi.org/10.5194/acp-23-389-2023.

Bretherton, C. S., C. Smith, and J. M. Wallace, 1992: An Intercomparison of Methods for Finding Coupled Patterns in Climate Data. *Journal of Climate*, **5**, 541–560, https://doi.org/10.1175/1520-0442(1992)005<0541:AIOMFF>2.0.CO;2.

Brown, H., H. Wang, M. Flanner, X. Liu, B. Singh, R. Zhang, Y. Yang, and M. Wu, 2022: Brown Carbon Fuel and Emission Source Attributions to Global Snow Darkening Effect. *Journal of Advances in Modeling Earth Systems*, **14**, e2021MS002768, https://doi.org/10.1029/2021MS002768.

Chakraborty, S., B. Guan, D. E. Waliser, A. M. da Silva, S. Uluatam, and P. Hess, 2021: Extending the Atmospheric River Concept to Aerosols: Climate and Air Quality Impacts. *Geophysical Research Letters*, **48**, e2020GL091827, https://doi.org/10.1029/2020GL091827.

——, ——, ——, and ——, 2022: Aerosol atmospheric rivers: climatology, event characteristics, and detection algorithm sensitivities. *Atmospheric Chemistry and Physics*, **22**, 8175–8195, https://doi.org/10.5194/acp-22-8175-2022.

Clarke, A. D., and K. J. Noone, 1985: Soot in the Arctic snowpack: a cause for perturbations in radiative transfer. *Atmospheric Environment (1967)*, **19**, 2045–2053, https://doi.org/10.1016/0004-6981(85)90113-1.

Comiso, J. C., C. L. Parkinson, R. Gersten, and L. Stock, 2008: Accelerated decline in the Arctic sea ice cover. *Geophysical Research Letters*, **35**, https://doi.org/10.1029/2007GL031972.

Dada, L., and Coauthors, 2022: A central arctic extreme aerosol event triggered by a warm air-mass intrusion. *Nat Commun*, **13**, 5290, https://doi.org/10.1038/s41467-022-32872-2.

DeRepentigny, P., and Coauthors, 2022: Enhanced simulated early 21st century Arctic sea ice loss due to CMIP6 biomass burning emissions. *Science Advances*, **8**, eabo2405, https://doi.org/10.1126/sciadv.abo2405.

Ding, S., and Coauthors, 2019: Observed Interactions Between Black Carbon and Hydrometeor During Wet Scavenging in Mixed-Phase Clouds. *Geophysical Research Letters*, **46**, 8453–8463, https://doi.org/10.1029/2019GL083171.

Durack, P. J., and K. E. Taylor, 2016: PCMDI AMIP SST and sea-ice boundary conditions version 1.1.0. https://doi.org/10.22033/ESGF/input4MIPs.1120.

Engelmann, R., and Coauthors, 2021: Wildfire smoke, Arctic haze, and aerosol effects on mixed-phase and cirrus clouds over the North Pole region during MOSAiC: an introduction. *Atmospheric Chemistry and Physics*, **21**, 13397–13423, https://doi.org/10.5194/acp-21-13397-2021.

Flanner, M. G., 2013: Arctic climate sensitivity to local black carbon. *Journal of Geophysical Research: Atmospheres*, **118**, 1840–1851, https://doi.org/10.1002/jgrd.50176.

Gong, Z., L. Zhong, L. Hua, and J. Feng, The role of atmospheric rivers and associated circulation patterns in the Arctic warming in boreal winter. *International Journal of Climatology*, **n/a**, https://doi.org/10.1002/joc.8444.

Goosse, H., and Coauthors, 2018: Quantifying climate feedbacks in polar regions. *Nat Commun*, **9**, 1919, https://doi.org/10.1038/s41467-018-04173-0.

Guan, B., and D. E. Waliser, 2015: Detection of atmospheric rivers: Evaluation and application of an algorithm for global studies. *Journal of Geophysical Research: Atmospheres*, **120**, 12514–12535, https://doi.org/10.1002/2015JD024257.

——, and ——, 2019: Tracking Atmospheric Rivers Globally: Spatial Distributions and Temporal Evolution of Life Cycle Characteristics. *Journal of Geophysical Research: Atmospheres*, **124**, 12523–12552, https://doi.org/10.1029/2019JD031205.

Hahn, L. C., K. C. Armour, M. D. Zelinka, C. M. Bitz, and A. Donohoe, 2021: Contributions to Polar Amplification in CMIP5 and CMIP6 Models. *Frontiers in Earth Science*, **9**.

Heutte, B., and Coauthors, 2023: Measurements of aerosol microphysical and chemical properties in the central Arctic atmosphere during MOSAiC. *Sci Data*, **10**, 690, https://doi.org/10.1038/s41597-023-02586-1.

Hobbs, P. V., 1993: Chapter 2 Aerosol-Cloud Interactions. *International Geophysics*, P.V. Hobbs, Ed., Vol. 54 of *Aerosol–Cloud–Climate Interactions*, Academic Press, 33–73.

Kirbus, B., and Coauthors, 2023: Surface impacts and associated mechanisms of a moisture intrusion into the Arctic observed in mid-April 2020 during MOSAiC. *Front. Earth Sci.*, **11**, https://doi.org/10.3389/feart.2023.1147848.

Koch, D., and A. D. Del Genio, 2010: Black carbon semi-direct effects on cloud cover: review and synthesis. *Atmospheric Chemistry and Physics*, **10**, 7685–7696, https://doi.org/10.5194/acp-10-7685-2010.

Kramshøj, M., I. Vedel-Petersen, M. Schollert, Å. Rinnan, J. Nymand, H. Ro-Poulsen, and R. Rinnan, 2016: Large increases in Arctic biogenic volatile emissions are a direct effect of warming. *Nature Geosci*, **9**, 349–352, https://doi.org/10.1038/ngeo2692.

Lapere, R., and Coauthors, 2024: Polar Aerosol Atmospheric Rivers: Detection, Characteristics, and Potential Applications. *Journal of Geophysical Research: Atmospheres*, **129**, e2023JD039606, https://doi.org/10.1029/2023JD039606.

Liu, X., P.-L. Ma, H. Wang, S. Tilmes, B. Singh, R. C. Easter, S. J. Ghan, and P. J. Rasch, 2016: Description and evaluation of a new four-mode version of the Modal Aerosol Module (MAM4) within version 5.3 of the Community Atmosphere Model. *Geoscientific Model Development*, **9**, 505–522, https://doi.org/10.5194/gmd-9-505-2016.

Momenimovahed, A., and Coauthors, 2021: Comparison of black carbon measurement techniques for marine engine emissions using three marine fuel types. *Aerosol Science and Technology*, **56**, 46–62, https://doi.org/10.1080/02786826.2021.1967281.

Mouginot, J., and Coauthors, 2019: Forty-six years of Greenland Ice Sheet mass balance from 1972 to 2018. *Proceedings of the National Academy of Sciences*, **116**, 9239–9244, https://doi.org/10.1073/pnas.1904242116.

Nash, D., D. Waliser, B. Guan, H. Ye, and F. M. Ralph, 2018: The Role of Atmospheric Rivers in Extratropical and Polar Hydroclimate. *Journal of Geophysical Research: Atmospheres*, **123**, 6804–6821, https://doi.org/10.1029/2017JD028130.

Nielsen, I. E., and Coauthors, 2019: Biogenic and anthropogenic sources of aerosols at the High Arctic site Villum Research Station. *Atmospheric Chemistry and Physics*, **19**, 10239–10256, https://doi.org/10.5194/acp-19-10239-2019.

Overland, J. E., 2022: Arctic Climate Extremes. *Atmosphere*, **13**, 1670, https://doi.org/10.3390/atmos13101670.

Pithan, F., and T. Mauritsen, 2014: Arctic amplification dominated by temperature feedbacks in contemporary climate models. *Nature Geosci*, **7**, 181–184, https://doi.org/10.1038/ngeo2071.

Ponomarev, E., N. Yakimov, T. Ponomareva, O. Yakubailik, and S. G. Conard, 2021: Current Trend of Carbon Emissions from Wildfires in Siberia. *Atmosphere*, **12**, 559, https://doi.org/10.3390/atmos12050559.

Quinn, P. K., G. Shaw, E. Andrews, E. G. Dutton, T. Ruoho-Airola, and S. L. Gong, 2007: Arctic haze: current trends and knowledge gaps. *Tellus B: Chemical and Physical Meteorology*, **59**, 99–114, https://doi.org/10.1111/j.1600-0889.2006.00236.x.

Randles, C. A., and Coauthors, 2017: The MERRA-2 Aerosol Reanalysis, 1980 Onward. Part I: System Description and Data Assimilation Evaluation. *Journal of Climate*, **30**, 6823–6850, https://doi.org/10.1175/JCLI-D-16-0609.1.

Ren, L., Y. Yang, H. Wang, R. Zhang, P. Wang, and H. Liao, 2020: Source attribution of Arctic black carbon and sulfate aerosols and associated Arctic surface warming during 1980–2018. *Atmospheric Chemistry and Physics*, **20**, 9067–9085, https://doi.org/10.5194/acp-20-9067-2020.

Sand, M., T. K. Berntsen, Ø. Seland, and J. E. Kristjánsson, 2013: Arctic surface temperature change to emissions of black carbon within Arctic or midlatitudes. *Journal of Geophysical Research: Atmospheres*, **118**, 7788–7798, https://doi.org/10.1002/jgrd.50613.

——, and Coauthors, 2017: Aerosols at the poles: an AeroCom Phase II multi-model evaluation. *Atmospheric Chemistry and Physics*, **17**, 12197–12218, https://doi.org/10.5194/acp-17-12197-2017.

Schmale, J., P. Zieger, and A. M. L. Ekman, 2021: Aerosols in current and future Arctic climate. *Nat. Clim. Chang.*, **11**, 95–105, https://doi.org/10.1038/s41558-020-00969-5.

Serreze, M. C., and J. A. Francis, 2006: The Arctic Amplification Debate. *Climatic Change*, **76**, 241–264, https://doi.org/10.1007/s10584-005-9017-y.

——, and R. G. Barry, 2011: Processes and impacts of Arctic amplification: A research synthesis. *Global and Planetary Change*, **77**, 85–96, https://doi.org/10.1016/j.gloplacha.2011.03.004.

Shupe, M. D., and Coauthors, 2022: Overview of the MOSAiC expedition: Atmosphere. *Elementa: Science of the Anthropocene*, **10**, 00060, https://doi.org/10.1525/elementa.2021.00060.

Stroeve, J., and D. Notz, 2015: Insights on past and future sea-ice evolution from combining observations and models. *Global and Planetary Change*, **135**, 119–132, https://doi.org/10.1016/j.gloplacha.2015.10.011.

Thompson, D. W. J., and J. M. Wallace, 1998: The Arctic oscillation signature in the wintertime geopotential height and temperature fields. *Geophysical Research Letters*, **25**, 1297–1300, https://doi.org/10.1029/98GL00950.

Twomey, S. A., M. Piepgrass, and T. L. Wolfe, 1984: An assessment of the impact of pollution on global cloud albedo. *Tellus B*, **36B**, 356–366, https://doi.org/10.1111/j.1600-0889.1984.tb00254.x.

Voronova, O. S., A. L. Zima, V. L. Kladov, and E. V. Cherepanova, 2020: Anomalous Wildfires in Siberia in Summer 2019. *Izv. Atmos. Ocean. Phys.*, **56**, 1042–1052, https://doi.org/10.1134/S000143382009025X.

Wallace, J. M., C. Smith, and C. S. Bretherton, 1992: Singular Value Decomposition of Wintertime Sea Surface Temperature and 500-mb Height Anomalies. *Journal of Climate*, **5**, 561–576, https://doi.org/10.1175/1520-0442(1992)005<0561:SVDOWS>2.0.CO;2.

Wang, H., and Coauthors, 2014: Using an explicit emission tagging method in global modeling of source-receptor relationships for black carbon in the Arctic: Variations, sources, and transport pathways. *Journal of Geophysical Research: Atmospheres*, **119**, 12,888-12,909, https://doi.org/10.1002/2014JD022297.

——, and Coauthors, 2020: Aerosols in the E3SM Version 1: New Developments and Their Impacts on Radiative Forcing. *Journal of Advances in Modeling Earth Systems*, **12**, e2019MS001851, https://doi.org/10.1029/2019MS001851.

Warren, S. G., and W. J. Wiscombe, 1980: A Model for the Spectral Albedo of Snow. II: Snow Containing Atmospheric Aerosols. *Journal of the Atmospheric Sciences*, **37**, 2734–2745, https://doi.org/10.1175/1520-0469(1980)037<2734:AMFTSA>2.0.CO;2.

Wille, J. D., and Coauthors, 2021: Antarctic Atmospheric River Climatology and Precipitation Impacts. *Journal of Geophysical Research: Atmospheres*, **126**, e2020JD033788, https://doi.org/10.1029/2020JD033788.

Xian, P., and Coauthors, 2022: Arctic spring and summertime aerosol optical depth baseline from long-term observations and model reanalyses – Part 1: Climatology and trend. *Atmospheric Chemistry and Physics*, **22**, 9915–9947, https://doi.org/10.5194/acp-22-9915-2022.

Zelinka, M. D., S. A. Klein, K. E. Taylor, T. Andrews, M. J. Webb, J. M. Gregory, and P. M. Forster, 2013: Contributions of Different Cloud Types to Feedbacks and Rapid Adjustments in CMIP5. *Journal of Climate*, **26**, 5007–5027, https://doi.org/10.1175/JCLI-D-12-00555.1.

——, T. A. Myers, D. T. McCoy, S. Po-Chedley, P. M. Caldwell, P. Ceppi, S. A. Klein, and K. E. Taylor, 2020: Causes of Higher Climate Sensitivity in CMIP6 Models. *Geophysical Research Letters*, **47**, e2019GL085782, https://doi.org/10.1029/2019GL085782.

Zhang, P., G. Chen, M. Ting, L. Ruby Leung, B. Guan, and L. Li, 2023: More frequent atmospheric rivers slow the seasonal recovery of Arctic sea ice. *Nat. Clim. Chang.*, **13**, 266–273, https://doi.org/10.1038/s41558-023-01599-3.

Chapter 5
Conclusions and Future Work

5.1 Summary

Arctic Amplification has very important implications for local communities and ecosystems within the Arctic, but also potentially for weather extremes in the lower latitudes. Currently, there is substantial uncertainty in the ability of climate models to capture the rate of polar amplified warming and sea ice decline. This dissertation demonstrates that large-scale circulation is key to understanding both historical Arctic climate change as well as reconciling biases between global climate model simulations and observations. The nudging and tagging approaches detailed in this dissertation, are used to investigate the influence of large-scale circulation on radiation, moisture and aerosols. Through a more comprehensive understanding of how circulation bridges the atmosphere, ocean and land as well determines the redistribution of energy we can make improvements to our extreme event and sea ice forecasting systems as well as future projections of Arctic climate change. This understanding can also aid potentially vulnerable communities that may need ever evolving adaptation strategies to combat shifts in food and water resources, weather extremes, coastal erosion or wildfire emissions as well as the potential destruction of infrastructure and relocation of communities.

5.2 Key Results

Chapter 2 shows the optimal large-scale circulation pattern generating enhanced sea ice decline, manifested as a “Figure-8”-like barotropic anticyclone with one lobe over the central Arctic and another extending over Greenland. Winds cause this melting through subsidence-

driven adiabatic warming of the lower troposphere, which in combination with moistening, drives increases in downwelling longwave radiation. It is commonly believed that winds primarily impact sea ice change through export through the North Atlantic to lower latitudes, however the nudging simulations here show that sea ice decline caused by winds is primarily thermodynamically driven. By examining periods of the strongest sea ice decline in the CESM1 preindustrial control simulation with fixed anthropogenic forcing and paleoclimate reananlysis products far preceding industrialization, this study links the optimal large-scale circulation pattern contributing to enhanced sea ice decline over the satellite era to internal atmospheric variability. Thus, this research serves as comprehensive description of how internal variability could be contributing to differences in the rate of sea ice decline between models and observations.

In Chapter 3, we use a novel nudging and water tagging approach in the iCESM1 to exhibit the importance of large-scale circulation in determining the amount and means by which moisture is transported into the Arctic. We then use radiative kernel approach to show the radiative impacts from this moisture transport that is a leading contributor to the positive warming feedback in the Arctic. Summertime moisture changes in the region are predominantly driven by remote transport that comes from the high latitude continents. We identify the common boreal summer pathways, such as over northern Europe and central Eurasia, however when considering the trend with observationally constrained circulation, we also note a large contribution from North America that has not been identified in previous water tagging studies. A key finding in this study, is that the increasing trend in moisture transported into the Arctic originates from the tropical Atlantic and Mediterranean Sea, often being evaporated in winter and spring, then precipitated over the continents before being

recycled and moved into the Arctic. The relatively short residence time of water vapor (~5-10 days) supports the need for an intermediate step between the tropics and Arctic, mediating the connections between the tropics and polar regions that is so often the foundation of theoretical frameworks explaining poleward heat and moisture transport. Continued efforts to understand this land capacitor effect are necessary because it accounts for over 2/3 of the second leading contributor to summertime Arctic warming via the water vapor feedback.

Chapter 4 showcases how large-scale circulation, in the form of an Arctic Oscillation-like pattern, with high/low pressure over the central Arctic and high/low pressure centers over Europe and Siberia can control black carbon transport into the Arctic. The winter of 2019-2020, which coincided with MOSAiC field expedition, experienced the positive phase of the Arctic Oscillation, suggesting that there was potentially less black carbon transported into the region during this time. However, there were still several extreme black carbon transport events that were observed. In this study we show that MERRA-2 is able to capture these events reasonably well and link them to aerosol atmospheric river (AAR) events from over western Europe and Siberia. E3SMv2 simulations with constrained circulation show improvements in mean poleward transport and AAR occurrence (in the case of the high-resolution configuration). While the E3SMv2 with nudging still struggles to capture the magnitude of black carbon transport into the Arctic. In all, this study is another example of the importance of accurate simulations of large-scale circulations and its role in capturing meridional transport.

5.3 Suggestions for future work

We have shown the importance of large-scale circulation in contributing to heat, moisture, and aerosol extremes within the Arctic, however we have examined these processes

individually. The results that we have shown here highlight the need for future work to account for the role of circulation in linking the coupled interactions between all components of the Earth system. This is especially the case for the land surface, which is not often considered in studies focused on the Arctic. Going forward, increasing attention to large-scale circulation and the representation of variability in persistence, propagation and magnitude of these patterns in climate models versus observations is needed. The approaches taken in this dissertation, namely nudging and tagging, provide a unique opportunity to further bridge the gaps between models and observations as well as characterize the role of observed atmospheric circulation variability in contributing to changes in other regions and processes. These studies have taken steps toward better understanding of the response of Arctic sea ice, moisture and black carbon to circulation trends over the satellite era, but have also shown potentially promising applications related to the ocean, soil or precipitation in lower latitudes.

Locally within the Arctic there are multiple aspects of physical processes in climate models and observational datasets that are still extremely uncertain. The primary uncertainty is related to the formation, persistence and interactions of low-level supercooled liquid containing clouds (Luo et al. 2023). In Luo et al. (2023) large-scale circulation, as well as interactions with aerosols, were implicated as important for the differences not only between observations and models, but also for the spread amongst models. Therefore, our lack of understanding in how cloud processes mediate the Arctic response to large-scale circulation and transport of moisture and aerosols requires further attention. Five more specific suggestions for future work are detailed below:

1. The first two chapters employ nudging in the CESM1 model, which has since been superseded by the CESM2. This new version of the model has updated cloud physical

schemes that targeted more realistic supercooled liquid in polar clouds. Nudging simulations with the updated physics may yield new and interesting results related to cloud interactions with large-scale circulation, radiation and sea ice.

2. Results from Chapter 1 suggest that the anticyclonic circulation pattern generating sea ice decline in the model is almost random, whereas in observationally constrained products there is some persistence from year-to-year. This suggests that we need to better understand the processes contributing to the persistence of atmospheric circulation patterns, because in this case it may be the cause of differences between longer-term changes in sea ice and climate between models and observations.
3. The framework we have established in Chapter 3, using the nudging and moisture tagging, can be applied to many other different regions around the Earth, such as over the midlatitude continents where there are growing concerns about water resources and wildfires, or somewhere with exceptional recycling, like the Amazon.
4. Chapter 3 also examines atmospheric river trends in the CESM2 Large Ensemble, finding that the free-running model struggles to capture the transport west of Greenland. When the model does show a similar circulation pattern, integrated vapor transport suggests that the moisture is coming from the Pacific, rather than the Atlantic, and moving very zonally. Therefore, future work should further investigate the trends in integrated vapor transport and atmospheric rivers with a focus on the causes of the spread amongst members and this zonal preference of transport.
5. The aerosol study was restricted by limited computational and storage capabilities. The influence of natural variability and emissions sources over a longer period might result in intriguing and different conclusions compared to our study. In the future, examining

trends and year-to-year variability in poleward aerosol transport and aerosol atmospheric rivers is needed.

References

Luo, R., Q. Ding, I. Baxter, X. Chen, Z. Wu, M. Bushuk, and H. Wang, 2023: Uncertain role of clouds in shaping summertime atmosphere-sea ice connections in reanalyses and CMIP6 models. *Clim Dyn*, **61**, 1973–1994, https://doi.org/10.1007/s00382-023-06785-9.

Appendix A

Chapter 2 Appendix

A.1 Supplementary Material

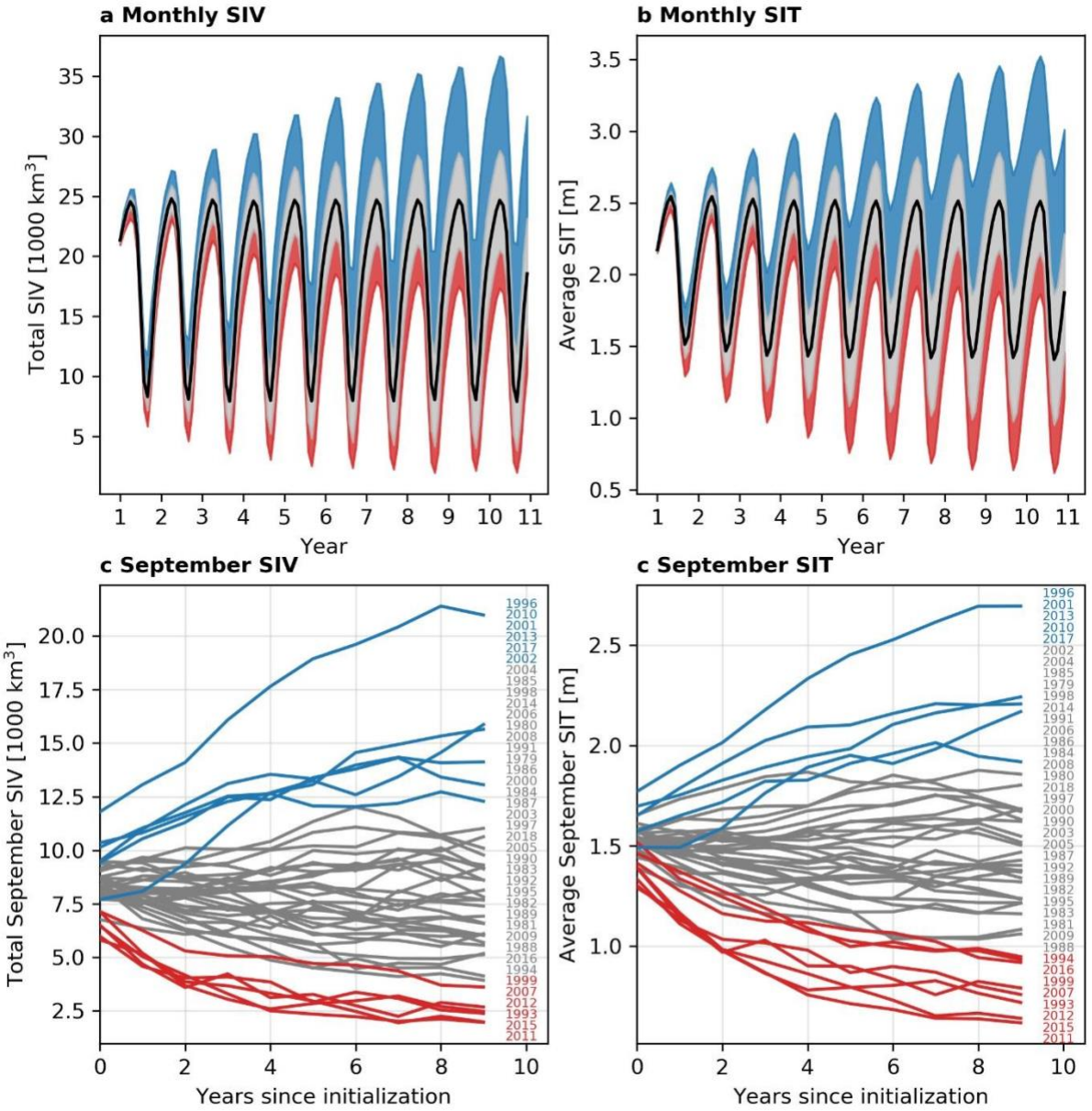

Supplementary Figure A1. Sea ice volume and thickness in the nudged simulations

(a) Monthly total sea ice volume (SIV), (b) monthly average sea ice thickness (SIT), (b) September SIV from each of the 10-yr nudged simulations, and (d) September SIT from each of the 10-yr nudged simulations. Red (a,b) shading and (c,d) curves represent the low sea ice cover group, defined as less than -1 standard deviation and blue indicates the high sea ice cover group, defined as greater than +1 standard deviation.

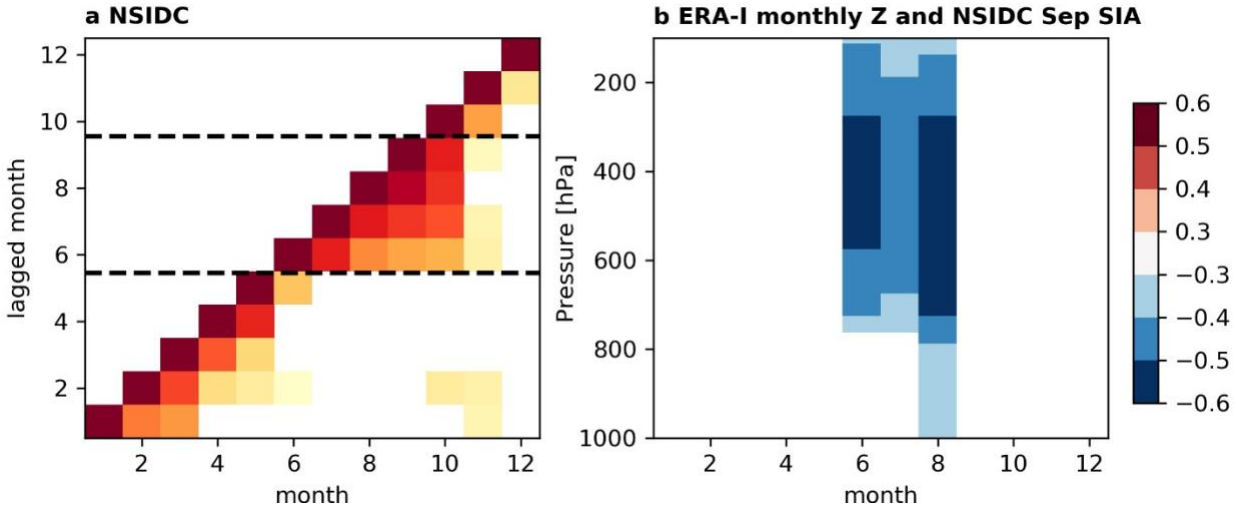

Supplementary Figure A2. (a) Autocorrelation of monthly total Arctic SIA (x-axis) with the preceding months (y-axis) in the NSIDC sea ice concentration product. Black dashed lines denote June through September. (b) Correlation of NSIDC total September SIA with monthly Arctic-averaged (70-90°N) geopotential height.

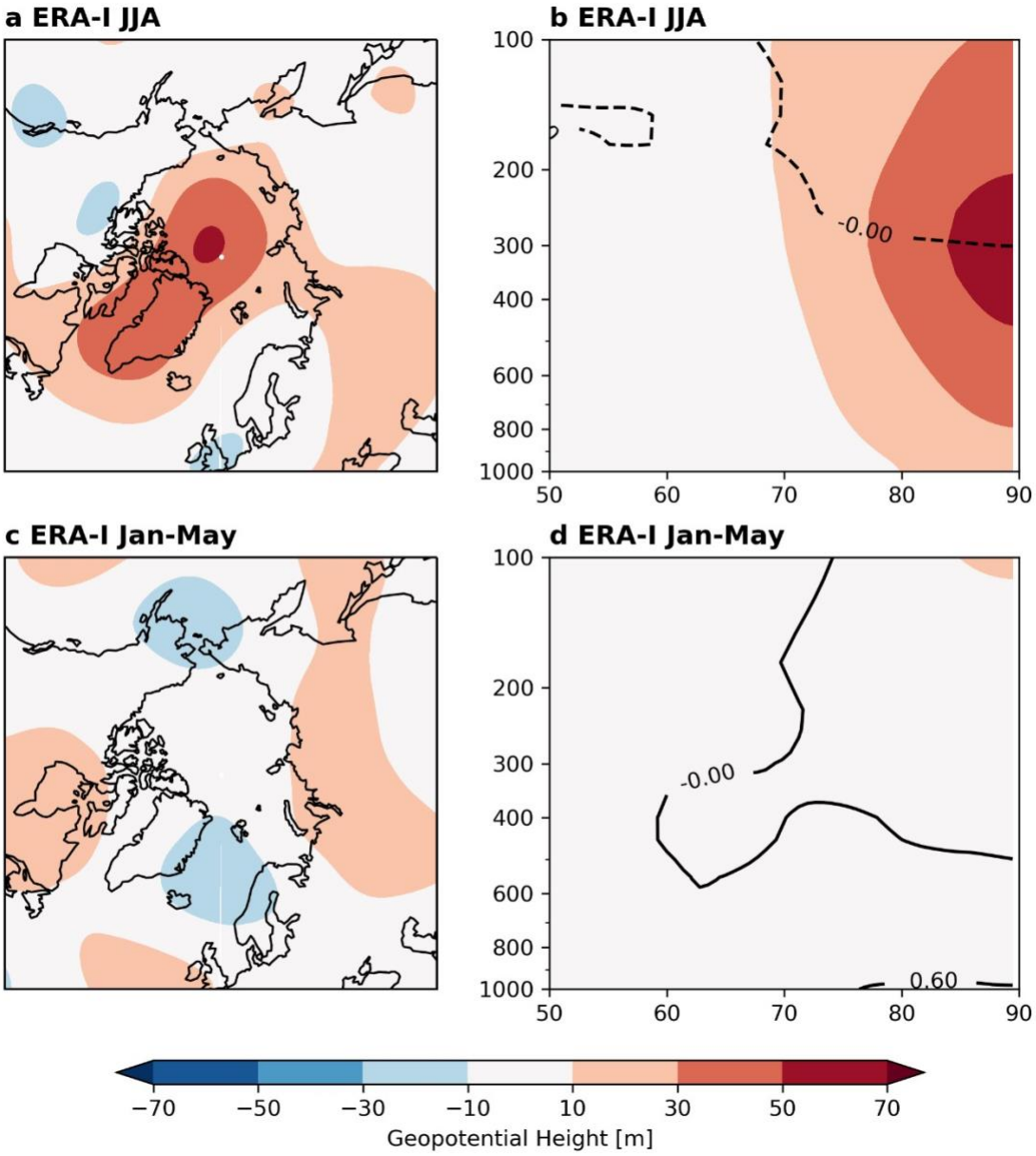

Supplementary Figure A3. Regression of JJA and Jan-May atmospheric variables onto total September SIA

Regression of JJA (a) Z200 and (b) zonal mean geopotential height (shading) and temperature (contour) onto total September SIA. Regression of Jan-May averaged (c) Z200 and (d) geopotential height (shading) and temperature (contour) onto total September SIA.

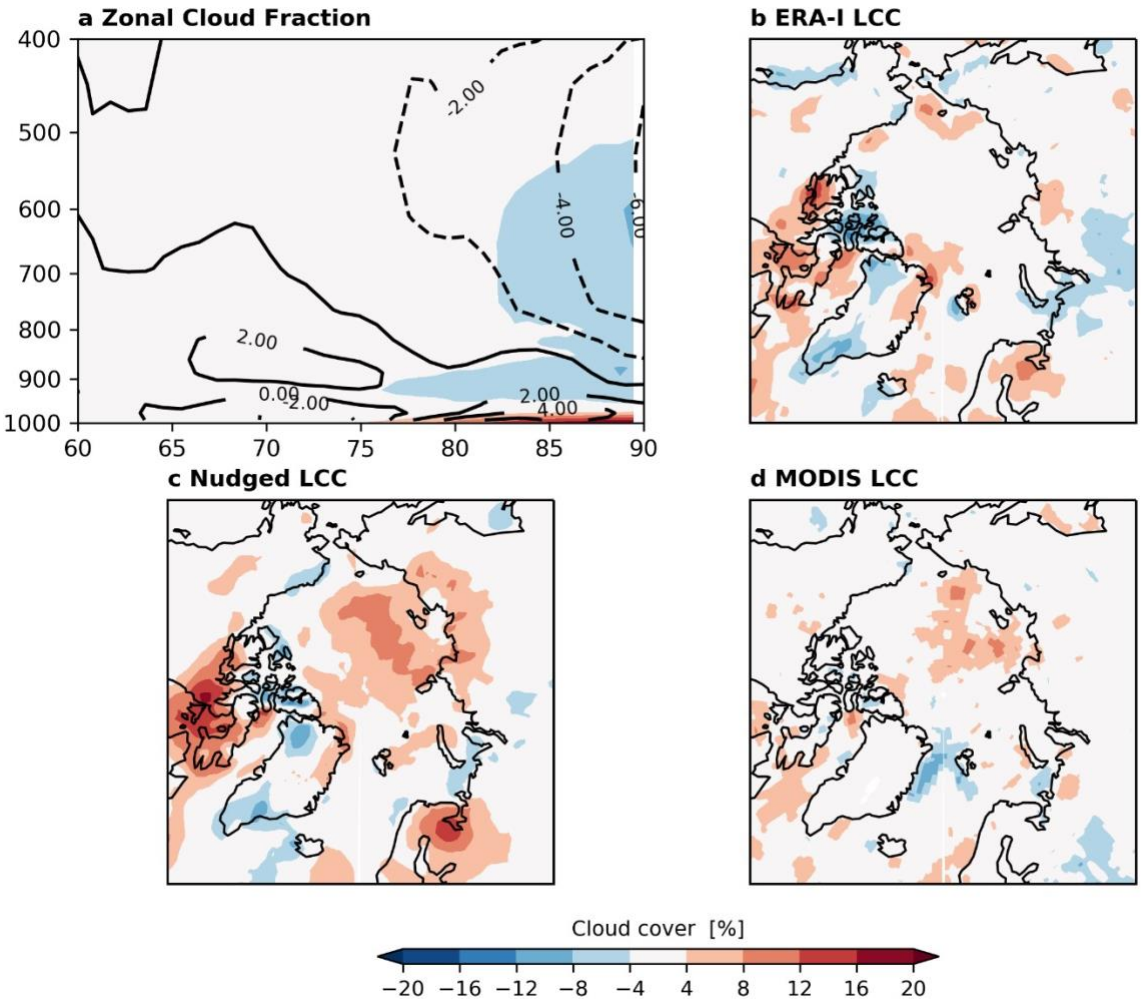

Supplementary Figure A4. Differences in cloud cover in extreme sea ice years from perpetual simulations

Regression of JJA (a) Z200 and (b) zonal mean geopotential height (shading) and temperature (contour) onto total September SIA. Regression of Jan-May averaged (c) Z200 and (d) geopotential height (shading) and temperature (contour) onto total September SIA.

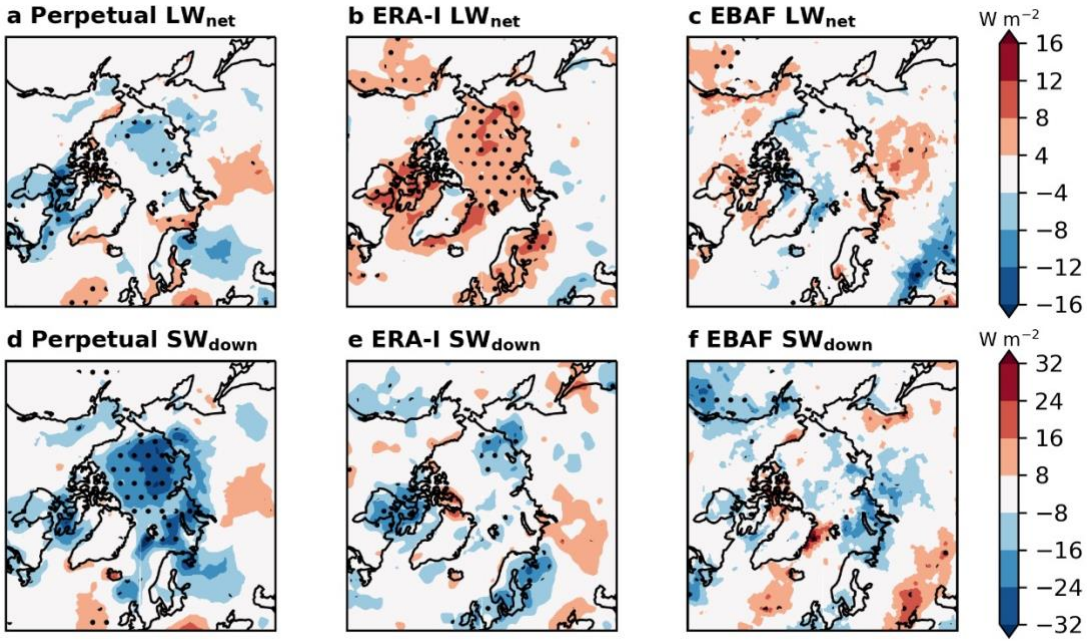

Supplementary Figure A5. Remaining surface radiative fluxes not shown in Figure 2 (a) JJA TOA net longwave (blue) and net shortwave (orange) radiative fluxes from CERES EBAF. (b) 10-yr mean JJA surface net longwave (blue) and net shortwave (orange) radiative fluxes from the nudged simulations relative to 2000-2018 mean. Thick outlines indicate years from the strong melting group in the 10-yr nudging simulations. Dashed outlines indicate years from the strong growth group in the 10-yr nudging simulations. Positive values indicate net outgoing radiation.

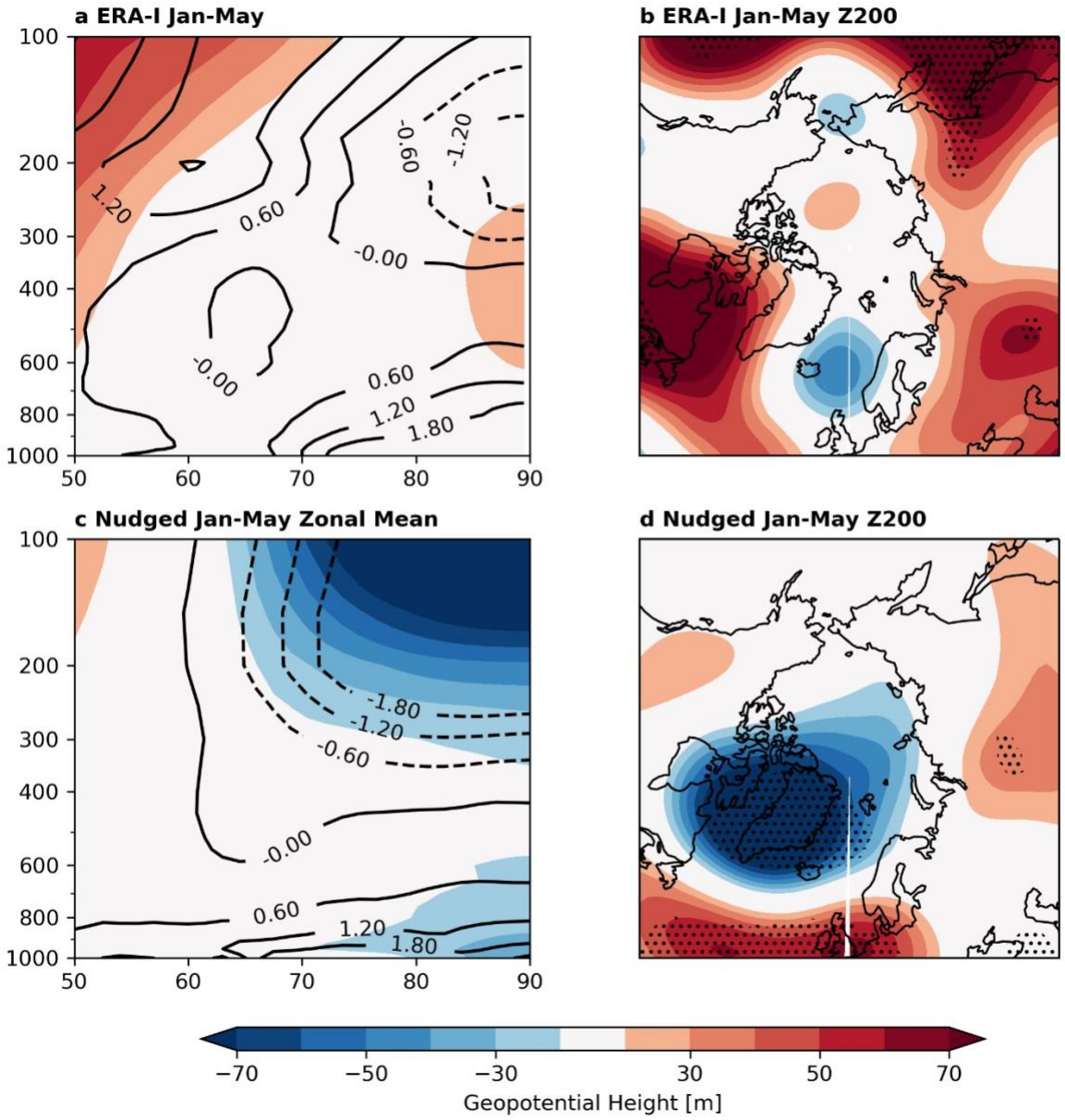

Supplementary Figure A6. PI control in preceding seasons

Same as Fig. 1d-g, but with ERA-I and perpetual nudged Jan-May Z200 and zonal mean geopotential height (shading; unit: m) and temperature (contour; unit: K), composited on the same strong melting minus strong growth September sea ice years from the NSIDC record and perpetual nudging simulations, respectively.

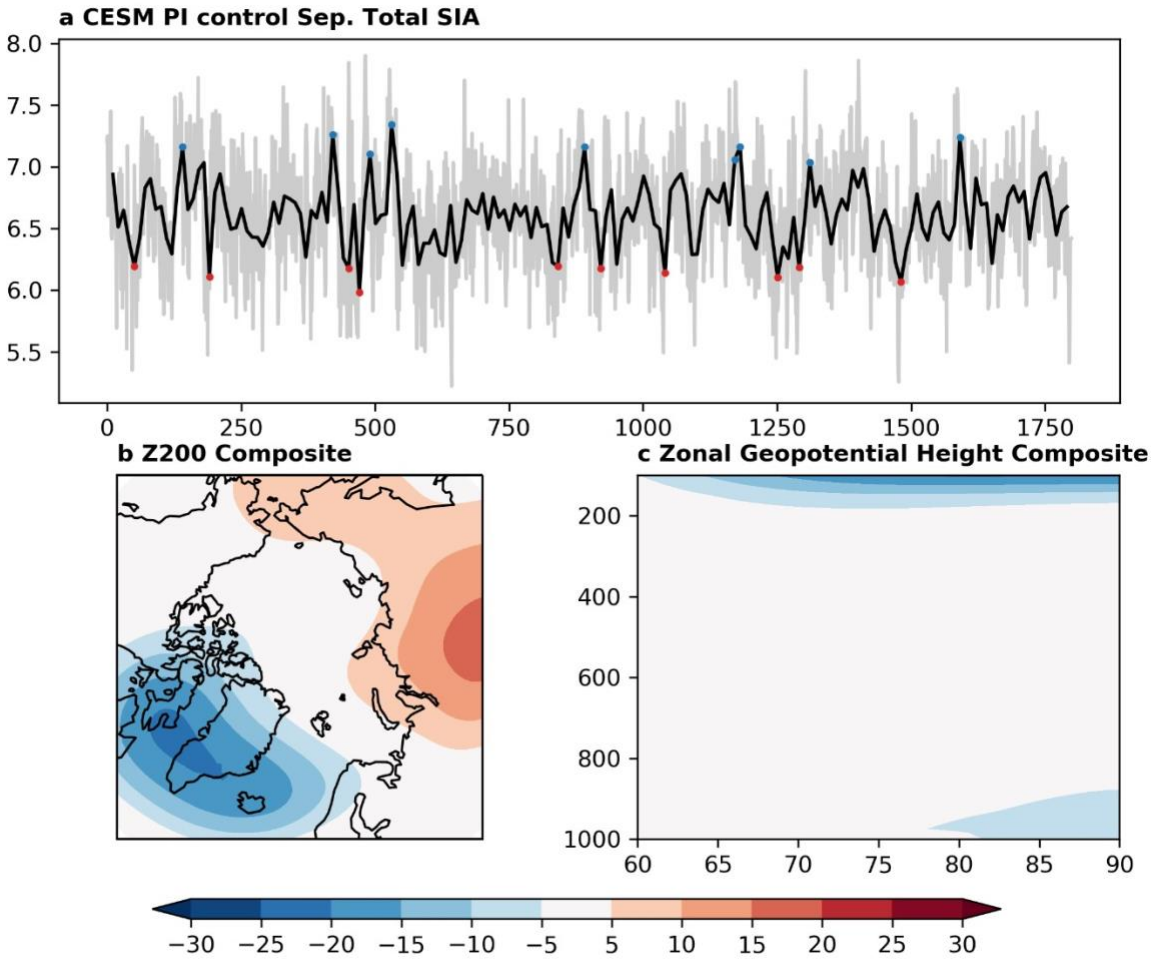

Supplementary Figure A7. PI control in preceding seasons
Same as Fig. 4, but with Jan-May Z200 and zonal mean geopotential height, composited on the same September sea ice years used in Fig. 4.

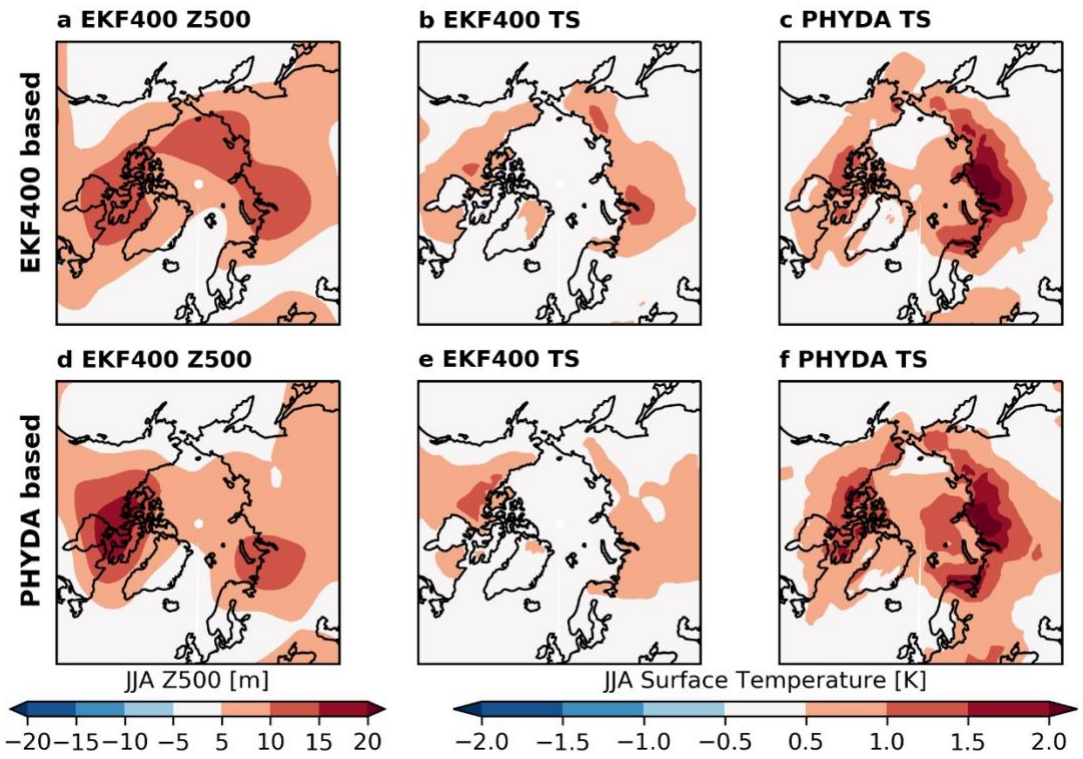

Supplementary Figure A8. Paleoreanalysis surface temperature-based composites
Composites based on Arctic-averaged (70-90°N) JJA surface temperature from (a-c) EKF400 and (d-f) PHYDA of (left column) EKF400 Z500, (middle column) EKF JJA surface temperature, and (right column) PHYDA JJA surface temperature.

Appendix B

Chapter 3 Appendix

B.1 Supplemental Material

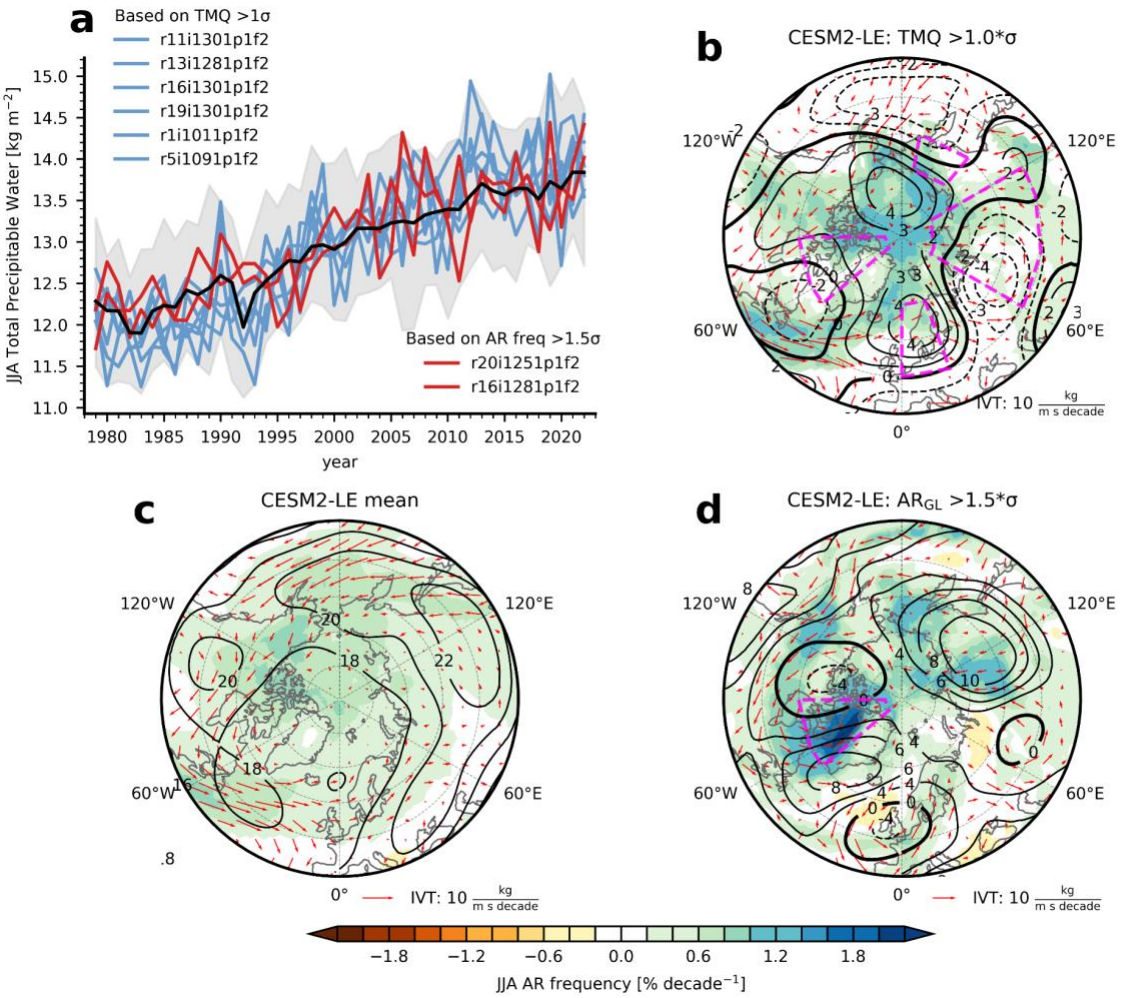

Supplementary Figure B1. Simulated extreme AR trends west of Greenland. a, Area-weighted mean JJA total precipitable water (70-90° N, kg m^{-2}) within the Arctic from the spread amongst 40 members from the CESM2-LE with smoothed biomass burning emissions (gray shading), the 40 member ensemble mean (black curve), 5 members with trends in area-weighted mean Arctic JJA total precipitable water exceeding 1 standard deviation (blue curves), and 2 members with AR frequency trends west of Greenland (60-85° N, 90-50° W, magenta box in panel **d**) that exceed 1.5 standard deviations (**a**). **b,** Trends in JJA AR frequency (shading, % $decade^{-1}$), IVT (red vectors, kg m^{-1} s^{-1} $decade^{-1}$), and JJA 200 hPa geopotential heights (black contours, m $decade^{-1}$). The 40-member ensemble mean trends are removed from AR frequency, IVT, and 200 hPa geopotential height trends (**b**). Shading shown only for AR frequency trends that are statistically significant at the 95%

confidence level. **c-d,** CESM2-LE 40-member mean (**c**) and members from the CESM2-LE with AR frequency trends in the western Greenland region that exceed 1.5 standard deviations (dashed blue curve, dashed magenta box: 60-85° N, 90-50° W) (**d**). The 40-member ensemble mean trends are removed from AR frequency, IVT, and 200 hPa geopotential height trends in panel (**d**). Shading in panels (**b-d**) only shows statistically significant AR frequency trends at the 95% confidence level.

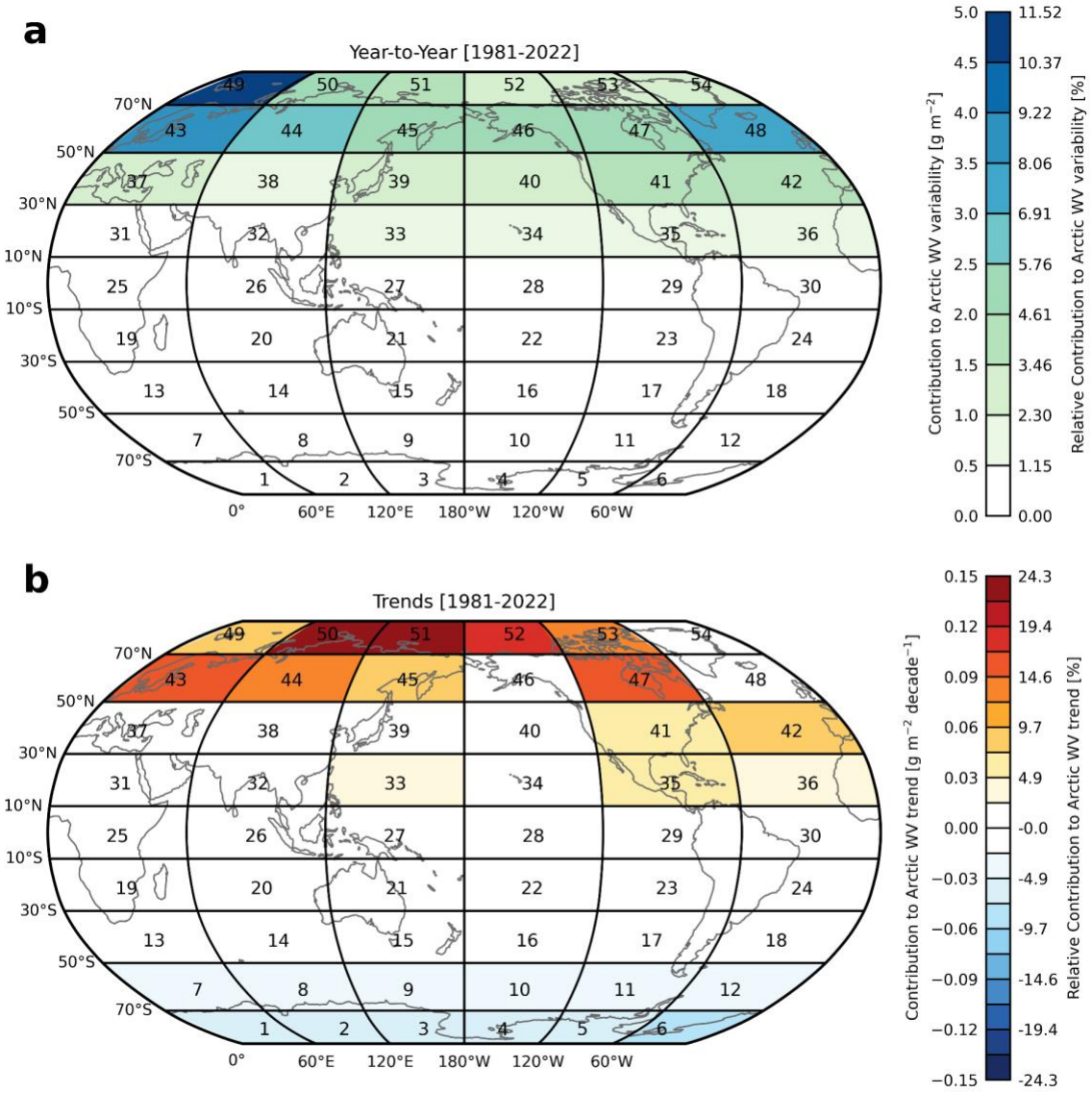

Supplementary Figure B2. Annual mean contributions to Arctic moisture. a,b, Root mean square error (kg m^{-2}) when each region is removed from annual mean Arctic (70-90° N) total column precipitable water (**a**) and linear decadal trends (1979-2022, g m^{-2} $decade^{-1}$) in annual mean Arctic (70-90° N) total column precipitable water (**b**) sourced from each of the 54 tagged source regions. Numbers indicate the source region number or tag. Shading corresponds to the magnitude of the RMSE (**a**) or trend (**b**) on the left side of the colorbar and the relative contribution (% of total) on the right of the colorbar. Contributions are standardized by the area of the source region (See Methods).

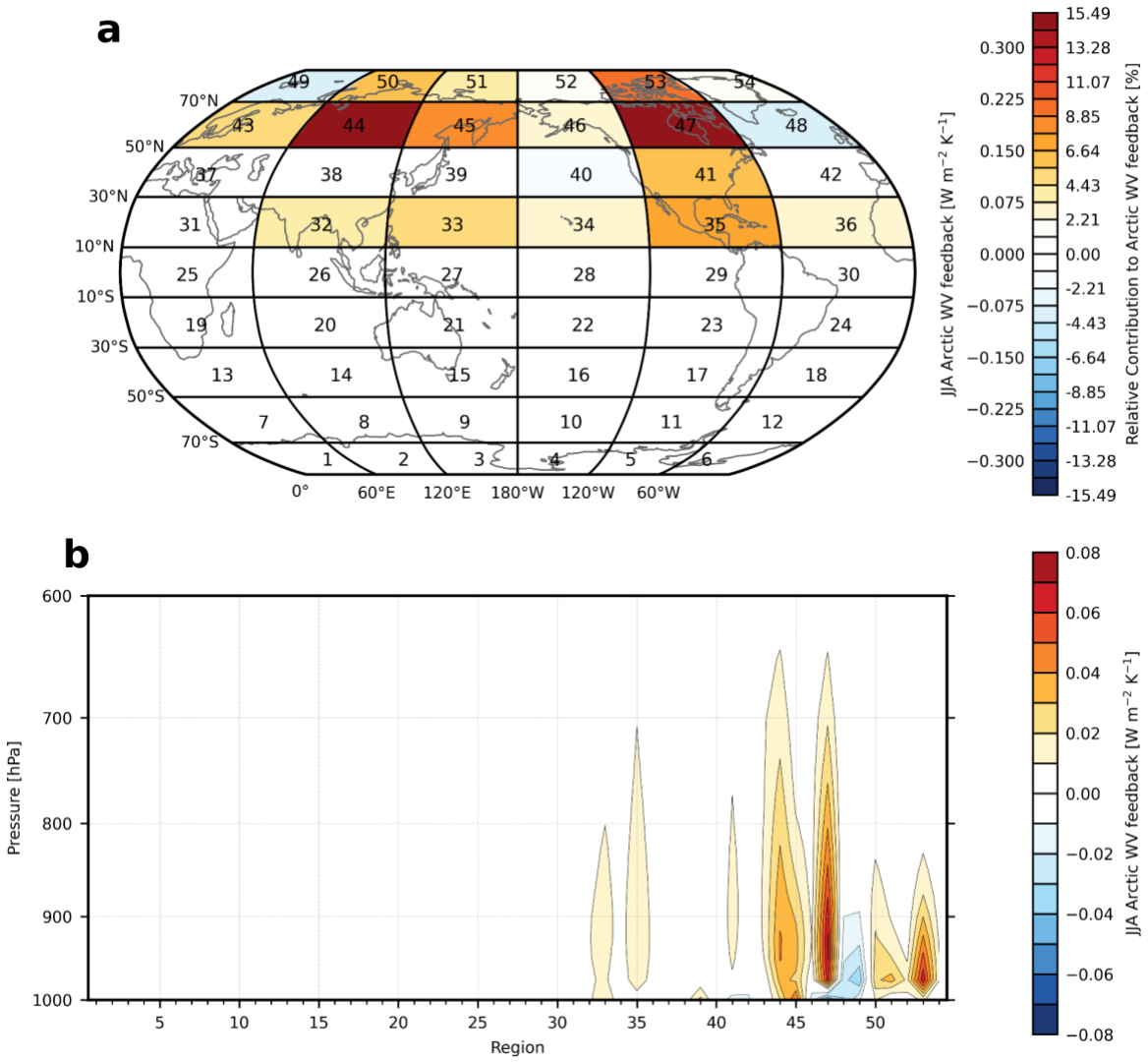

Supplementary Figure B3. Regional contribution to the Arctic summertime water vapor radiative effect using CAM5 radiative kernels. a, Total column integrated WV feedback (W m^{-2} $decade^{-1}$) computed by removing WV sourced from each region using the CAM5 radiative kernel approach (**a**) (Methods). **b,** Vertical structure of Arctic (70-90° N) WV feedback (W m^{-2} $decade^{-1}$), computed by removing WV from each tagged source region (x-axis) (**b**). Region numbers on x-axis in (**b**) correspond to numbered labels in panel (**a**).

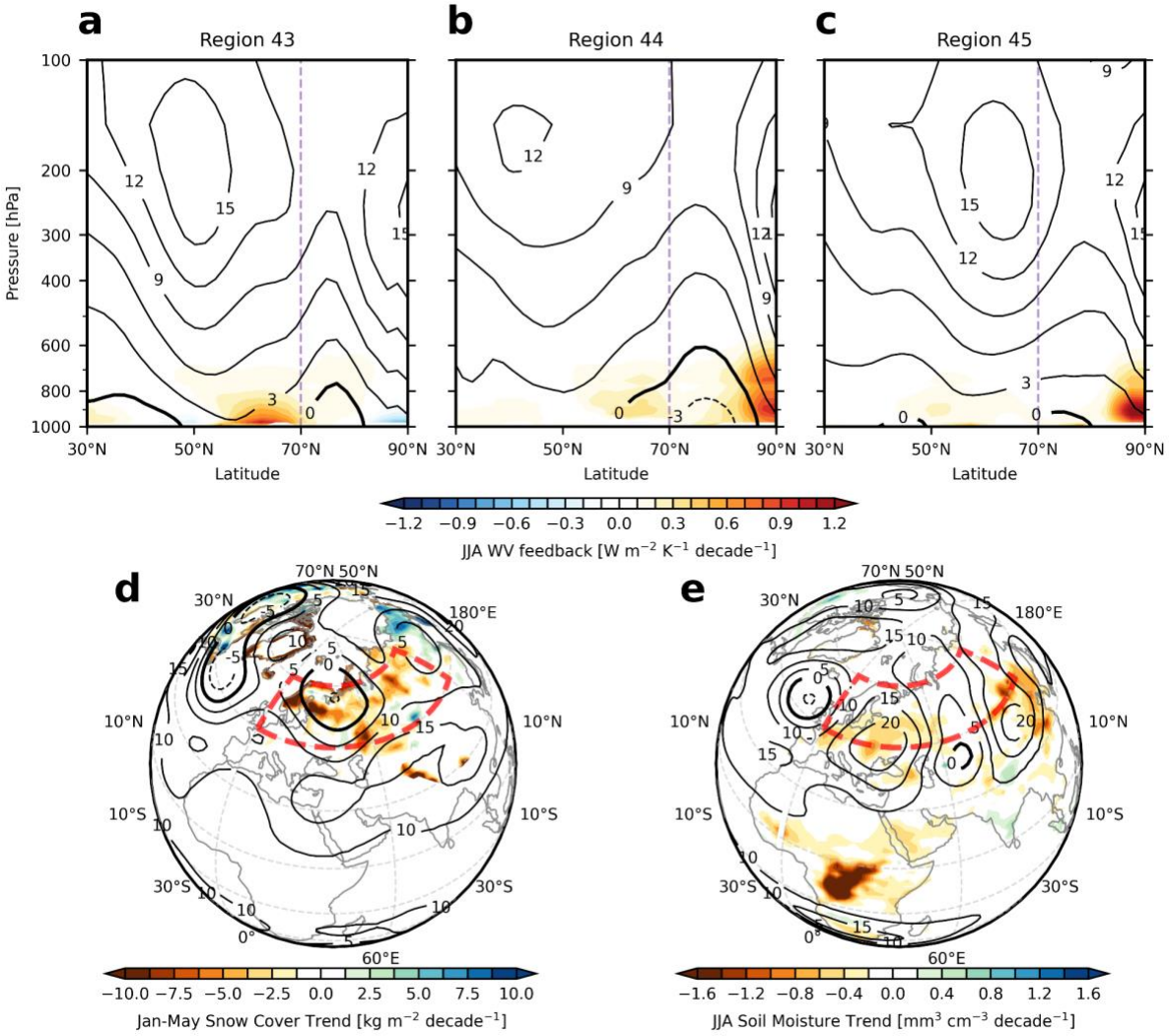

Supplementary Figure B4. Eurasian sourced moisture transport impacts and land capacitor. a-c, Zonal mean JJA water vapor feedback (W m^{-2} K^{-1} $decade^{-1}$) resulting from trends (1981-2022) in moisture sourced from region 43 (**a**), 44 (**b**), and 45 (**c**) as labeled in Fig. 3 along the 50-70° N band along Eurasia. Black contours show trends (1981-2022) trends in zonal mean JJA geopotential heights within 0-60° E (**a**), 60-120° E (**b**), and 120-180° E (**c**). **d,** The linear trends (1981-2022) in January-May-mean snow cover (shading, mm^3 cm^{-3} $decade^{-1}$) and January-May-mean 200 hPa geopotential height (black contours) (**d**). **e,** The linear trends (1981-2022) in JJA column-mean soil moisture over vegetated land surfaces (mm^3 cm^{-3} $decade^{-1}$) and JJA 200 hPa geopotential height (black contours) (**e**). Brown and green/blue shading is only shown for trends that are statistically significant at the 95% confidence level. Red dashed lines indicate the western and central Eurasia regions (43 and 44) (**d-e**).

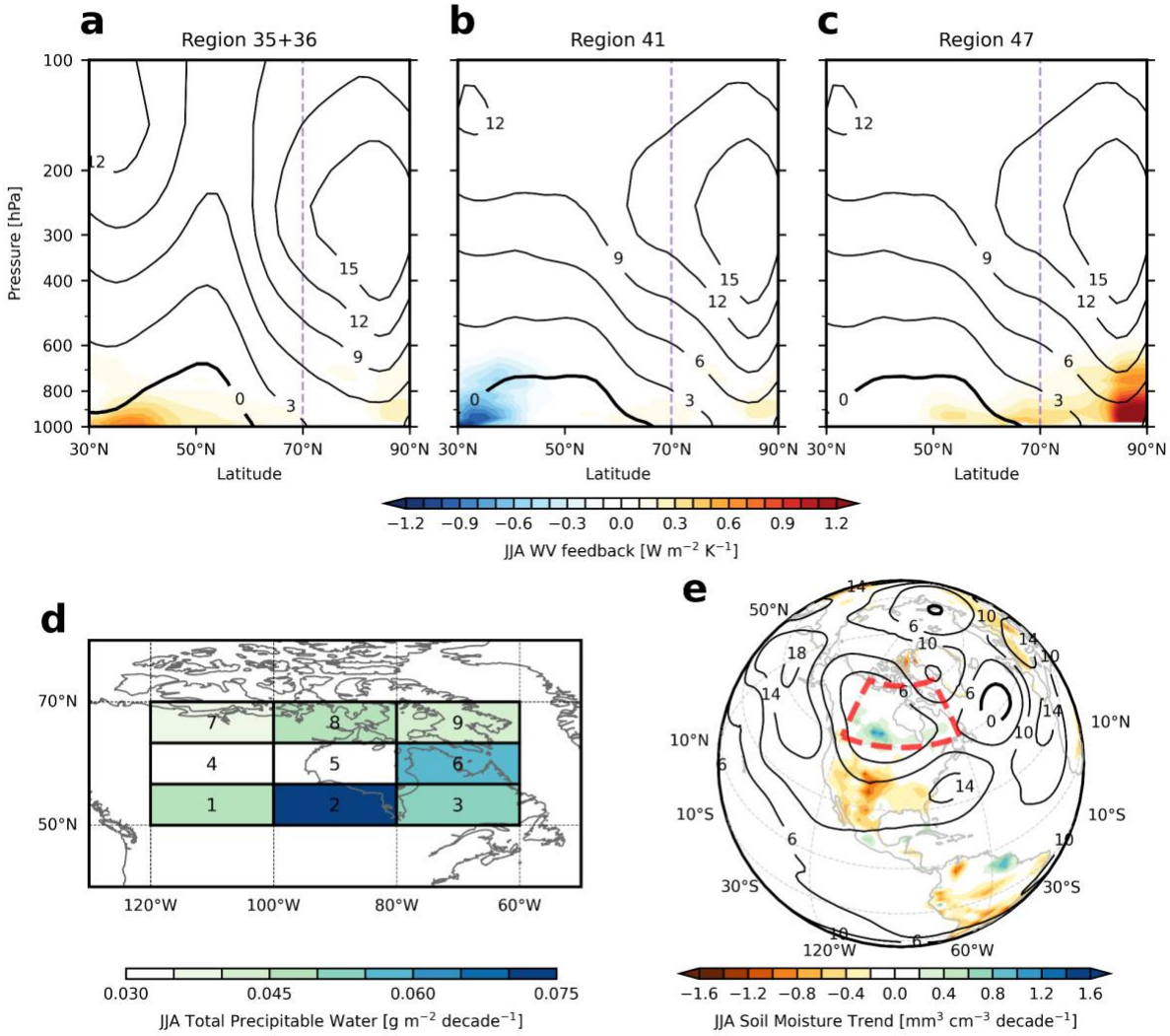

Supplementary Figure B5. Impacts and transport for key North American land capacitor. a-c, Vertical structure of zonally integrated moistening trends (shading, kg m kg^{-1} decade^{-1}) sourced from the tropical Atlantic (regions 35 and 36) (**a**), central and eastern United States (region 41) (**b**), and central and eastern Canada (region 47) (**c**). Contours show zonal mean geopotential heights within the North American corridor (60-120° W) (**a-c**). **d,** The linear trends (1981-2022) in Arctic total column precipitable water (kg m^{-2} decade^{-1}) originating from the 9 subregions within central and eastern Canada (region 47) (**d**). **e,** The linear trends (1981-2022) in column-mean (upper 10 m) soil moisture over vegetated land surfaces (mm^3 cm^{-3} decade^{-1}) and JJA 200 hPa geopotential height (black contours) (**e**). The red dashed box indicates central and eastern Canada (region 47). All brown and green/blue shading shown in panel (**e**) is statistically significant at the 95% confidence level.

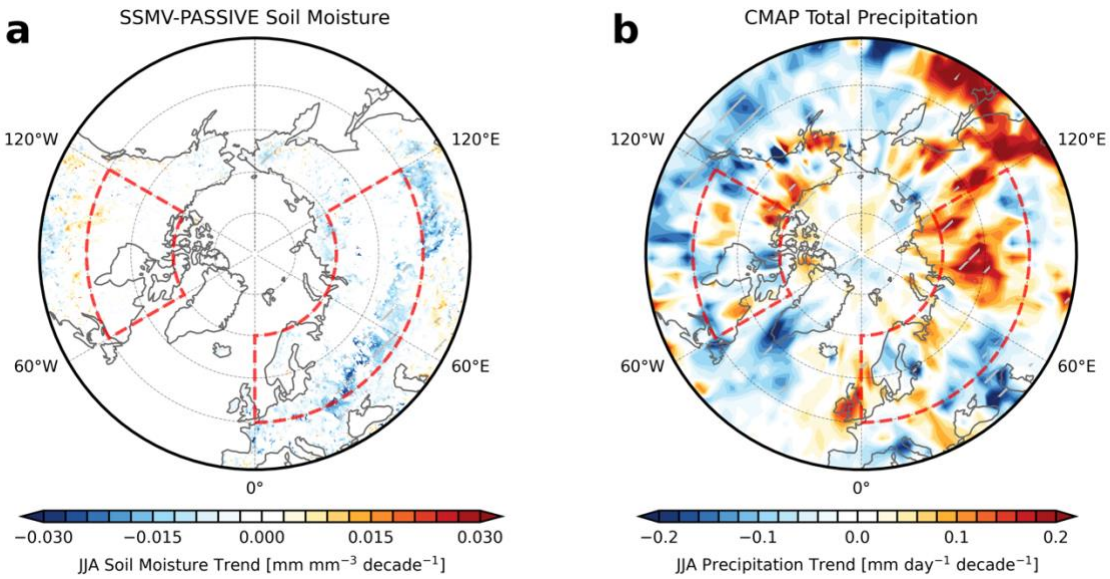

Supplementary Figure B6. Observed soil moisture trends.
(a) Linear trends (1981-2022) in JJA SSMV-Passive total column soil moisture from the SSMV-PASSIVE product (shading, mm^3 mm^{-3} $decade^{-1}$). Shading only shown for trends that are statistically significant at the 95% confidence level. Dash red boxes indicate regions of interest: 43, 44, and 47. (b) Linear trends (1981-2022) in JJA CMAP total precipitation (shading, mm day^{-1} $decade^{-1}$). Grey stippling indicates statistically significant trends at the 95% confidence level.

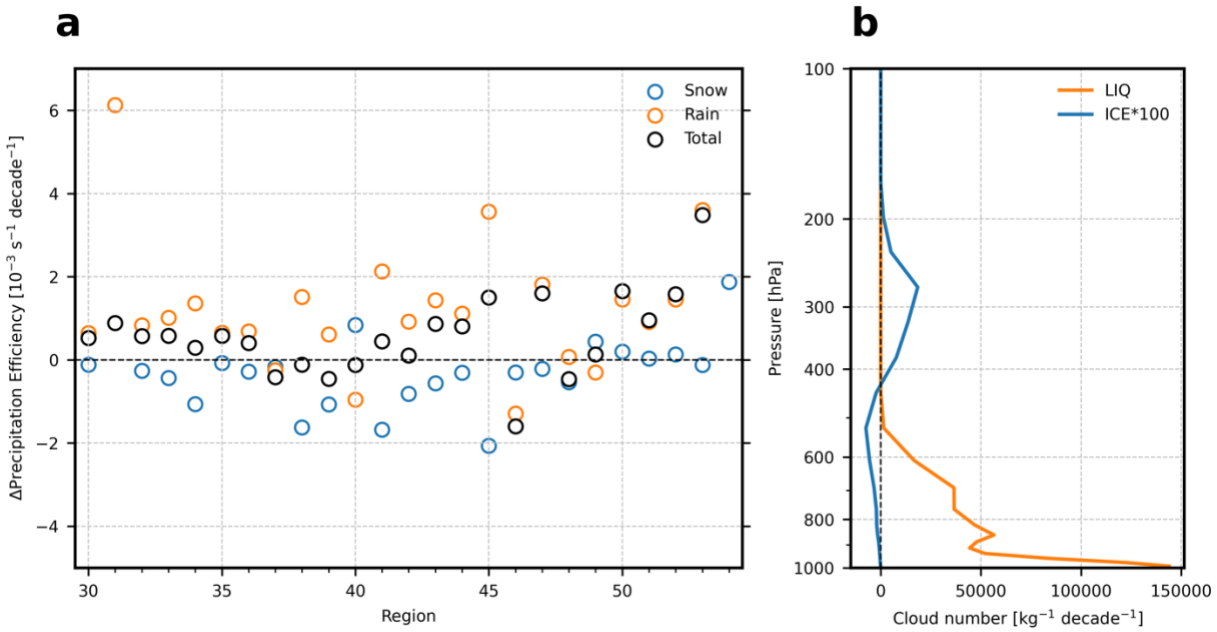

Extended Data Figure 7. Decreasing Precipitation Efficiency with Warming. a, Linear trend (1981-2022) in area-weighted Arctic average (70-90° N) snowfall (blue), rainfall (orange), and total (black) precipitation efficiency (precipitation divided by total water path, s^{-1} $decade^{-1}$) by Northern Hemisphere tagged region. The inverse can be considered the trend in residence time **(a)**. **b,** Linear trend (1981-2022) in area-weighted Arctic average (70-90° N) liquid (blue) and ice (orange) cloud number concentration (kg^{-1} $decade^{-1}$) **(b)**.

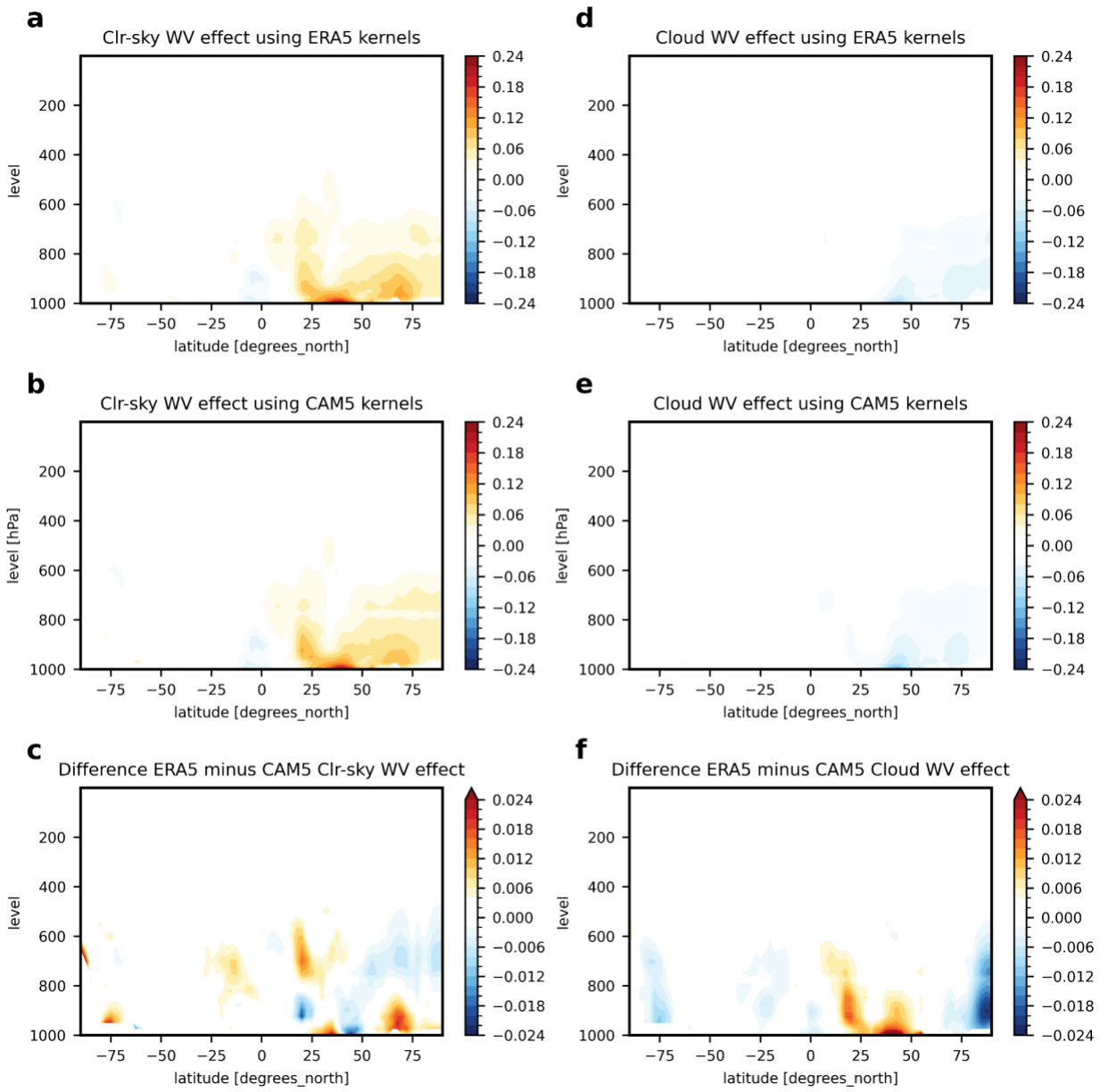

Supplementary Figure B8. Zonal mean water vapor radiative effect in ERA5 and CAM5 radiative kernels.

(a) The zonal mean clear-sky water vapor radiative effect (W m^{-2} $decade^{-1}$) in the iCESM1 simulations using the (a) ERA5 or (b) CAM5 radiative kernels and (c) the difference between the two approaches. (d-f) The zonal mean cloud water vapor radiative effect (W m^{-2} $decade^{-1}$) in the iCESM1 simulations using the (d) ERA5 or (e) CAM5 radiative kernels and (f) the difference between the two approaches.

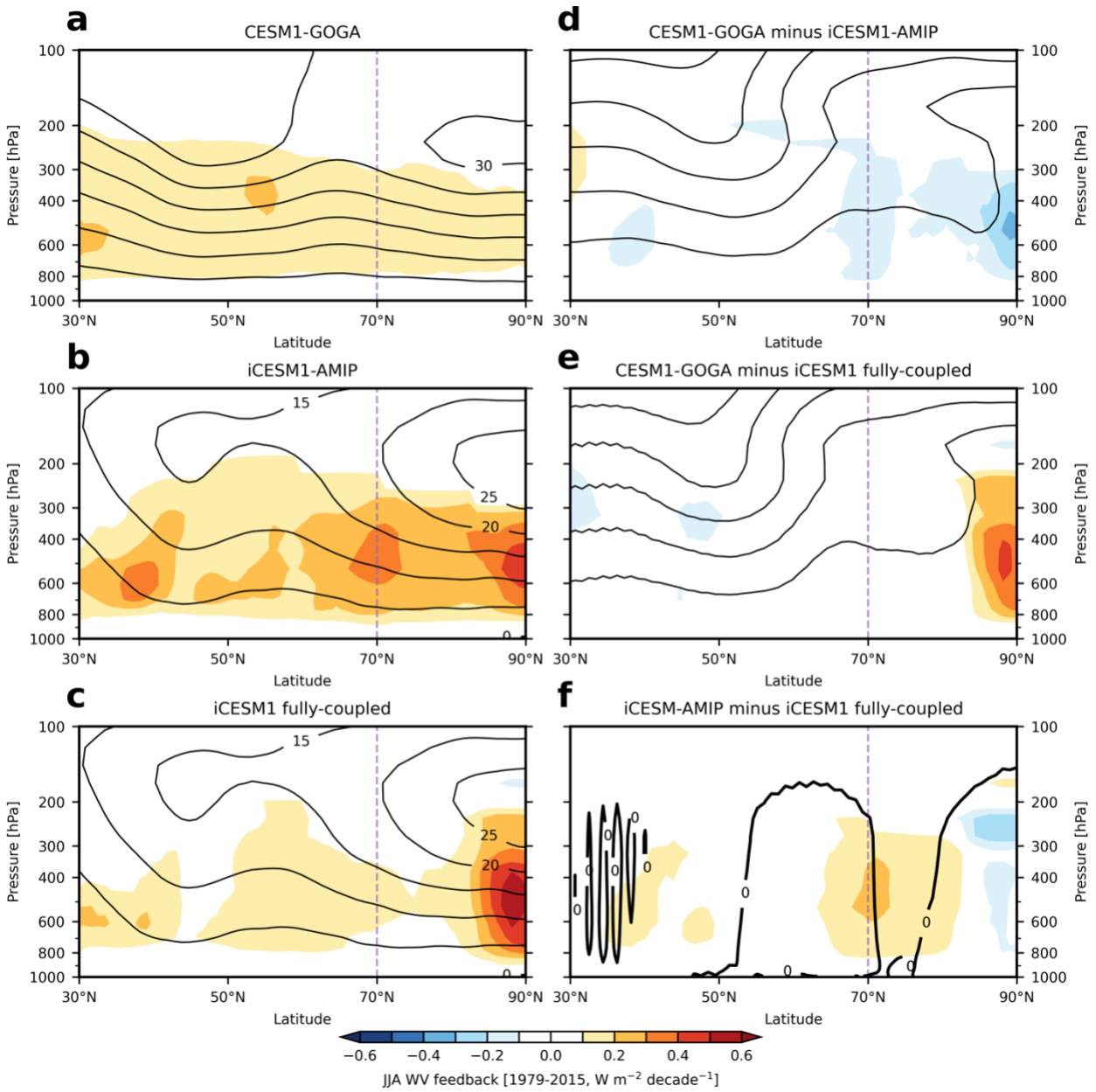

Supplementary Figure 9. Role of the ocean and winds in zonal mean JJA WV radiative effect. a-c, Zonal mean all-sky surface WV radiative feedback resulting from the 1979-2015 linear trends in the 10-member ensemble mean from CESM1-GOGA (**a**), iCESM1 AMIP or prescribed SST simulations (**b**), and iCESM1 fully-coupled simulations. **d-e,** The difference in the zonal mean all-sky WV radiative feedback response from the 1979-2015 linear trends from CESM1-GOGA minus iCESM1-AMIP (**d**), CESM1-GOGA minus iCESM1 fully-coupled (**e**), and iCESM1-AMIP minus iCESM1 fully-coupled (**f**).

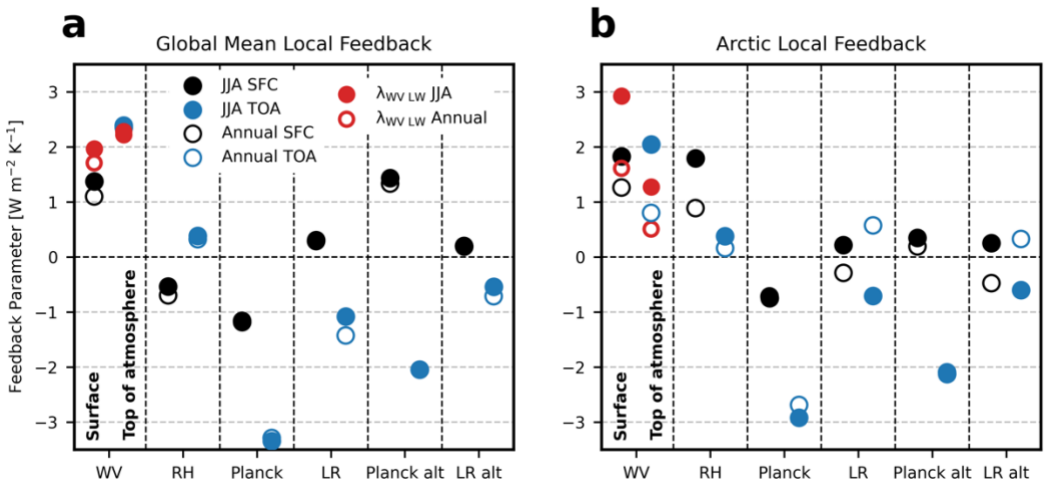

Supplementary Figure 10. Global and radiative feedbacks derived from nudged iCESM simulation. a, Surface (black) and TOA (blue) global mean local feedbacks (water vapor, relative humidity, Planck, lapse rate, alternative Planck, and alternative lapse rate) **(a)**. **b,** Surface (black) and TOA (blue) Arctic (70-90° N) mean local feedbacks (water vapor, relative humidity, Planck, lapse rate, alternative Planck, alternative lapse rate) **(b)**. Blue and orange circles correspond to monthly means. Filled and empty circles correspond to JJA and annual means, respectively.

Appendix C

Chapter 4 Appendix

C.1 Supplementary Material

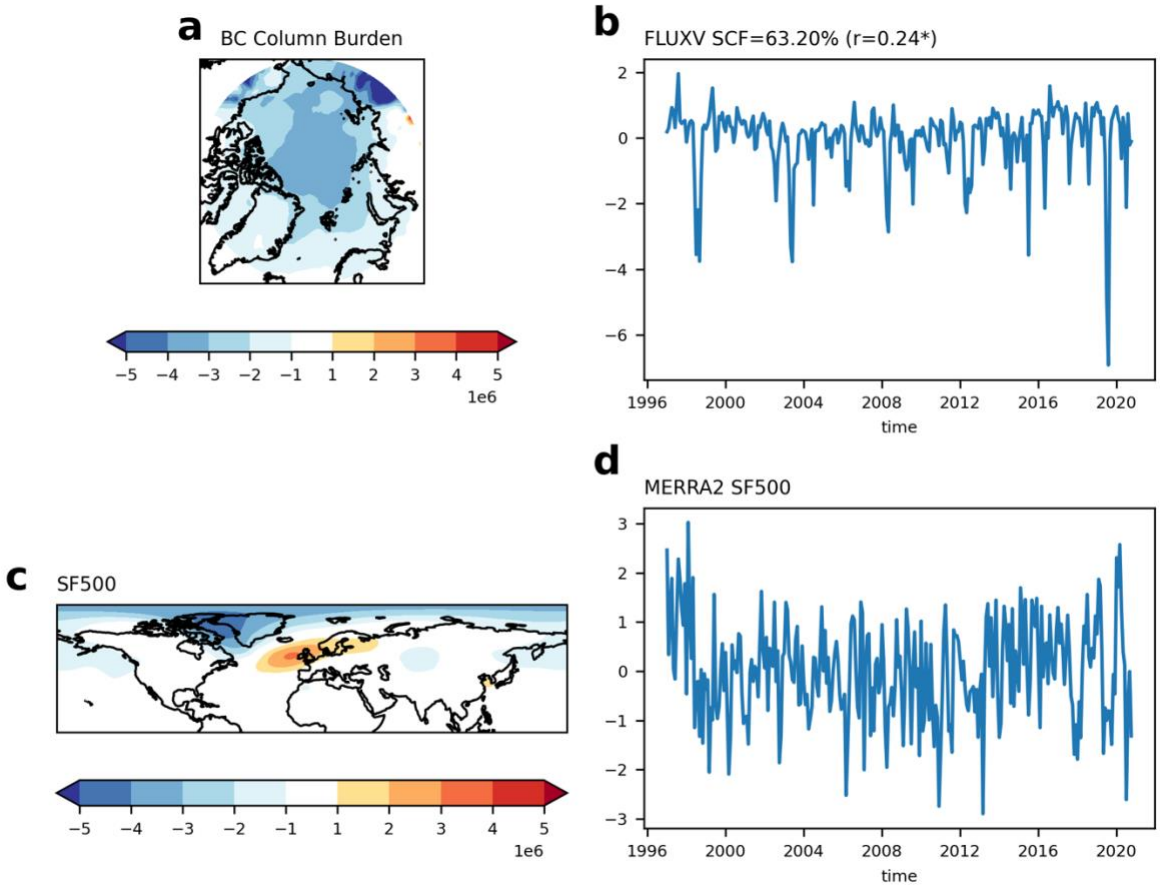

Supplementary Figure C1. Coupled Arctic BC and circulation mode: Spatial pattern of the leading MCA mode of monthly deseasoned and detrended (a) total column BC burden and (c) 500 hPa stream function over the Northern Hemisphere. Panels (b) and (d) are their respective time series. This leading mode accounts for 63.2% of the covariance fraction and the time series are significantly correlated (r=0.24).

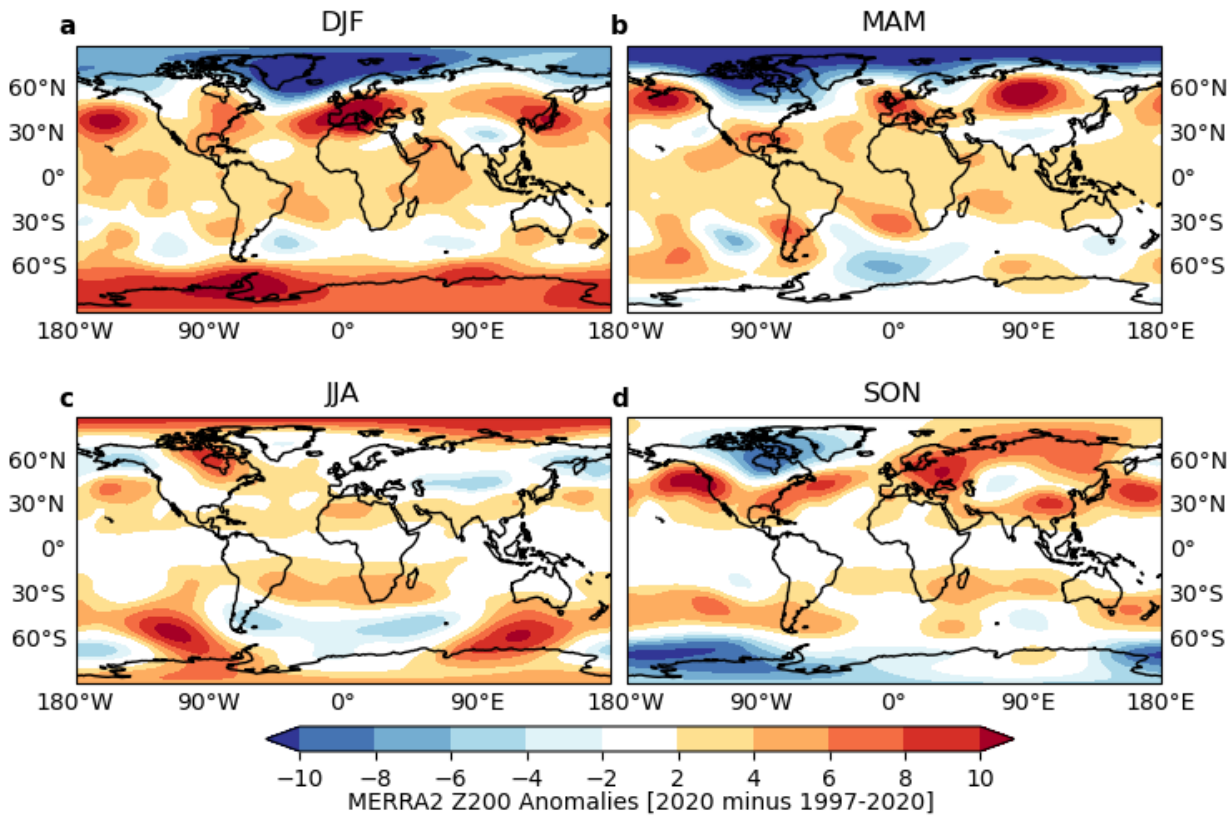

Supplementary Figure C2. 2019-2020 Atmospheric Circulation patterns determining poleward aerosol transport: 2019-2020 anomalies of 200 hPa geopotential heights relative to 1997-2018 for (a) DJF, (b) MAM, (c) JJA and (d) SON.

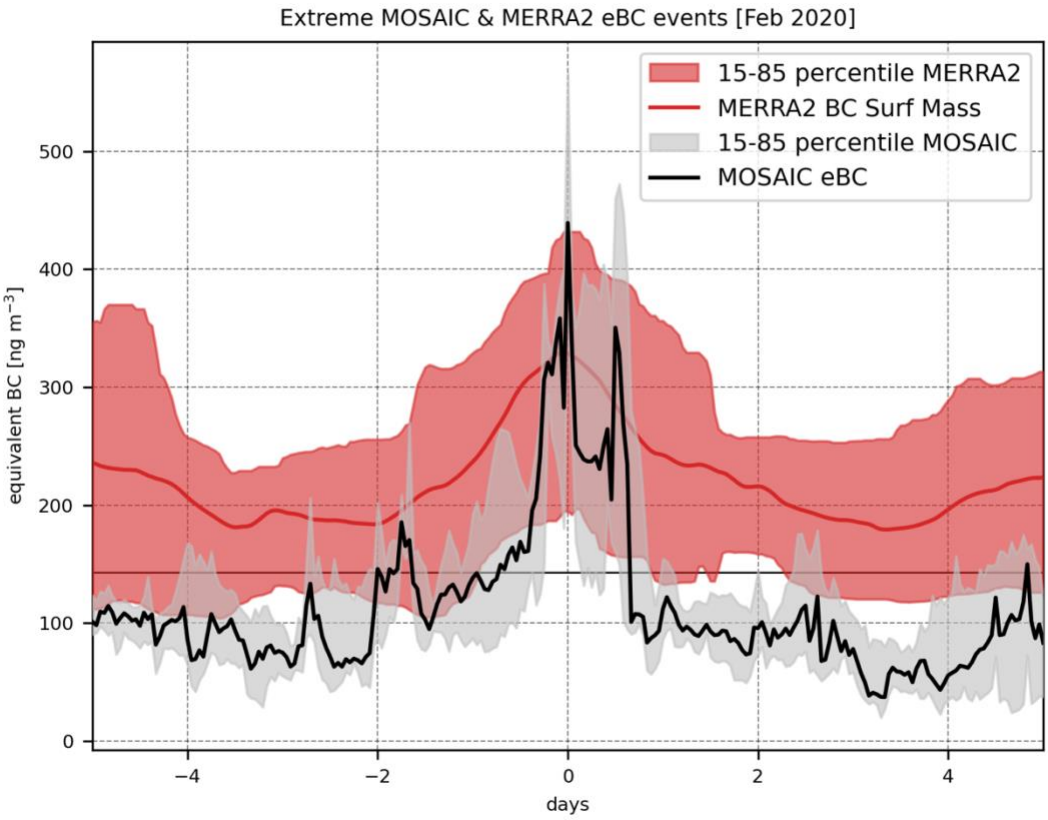

Supplementary Figure C3. Extreme aerosol events from MOSAiC during February: Same as Fig. 4.3 but only February extreme events.

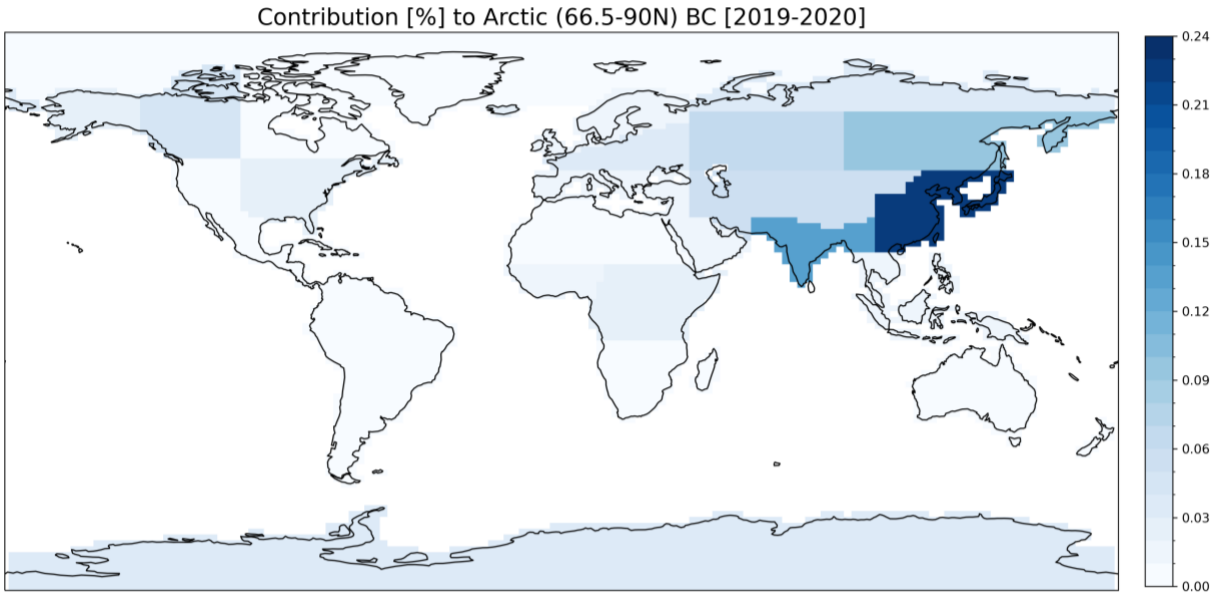

Supplementary Figure C3. Source region contributions to Arctic BC: Percent contribution of each of the 30 tagged source regions to 2019-2020 mean BC burden within the Arctic (70-90° N).